8
26

A Fabrication Stress Model for Axisymmetric Filament Wound Composite Structures

by

Vinh Dinh Nguyen

Dissertation submitted to the Faculty of the

Virginia Polytechnic Institute and State University

in partial fulfillment of the requirements for the degree of

Doctor of Philosophy

in

Mechanical Engineering

APPROVED:

Dr. Charles E. Knight, Chairman

Dr. Robert H. Fries

Dr. Alfred C. Loos

Dr. Hamilton H. Mabie

Dr. Reginald G. Mitchiner

February, 1988

Blacksburg, Virginia

A Fabrication Stress Model for Axisymmetric Filament Wound Composite Structures

by

Vinh Dinh Nguyen

Dr. Charles E. Knight, Chairman

Mechanical Engineering

(ABSTRACT)

A comprehensive fabrication stress model was developed to compute fiber stresses in axisymmetric filament wound composite structures at any stage of the fabrication process, a prerequisite for the evaluation of the performance of the composite structures from fabrication process variables. The stress model uses an isoparametric axisymmetric finite element formulation and a double-layered composite element to model the mechanical behavior of the composite material in any cure state. An incremental finite element formulation was used to model the winding and mandrel removal stages. A thermo-mechanical formulation was used to model the curing stage. Also, all major physical phenomena occurring in the fabrication stages which significantly affect the fiber stresses are taken into account: instantaneous tension loss in winding, tension loss due to multiple circuit winding, tension loss due to fiber motion through the uncured resin, material cure transition, and fiber stiffness degradation in a compressive strain state.

Two case studies were selected to evaluate and to illustrate the use of the fabrication stress model: the space shuttle booster joint overwrap and a filament wound composite bottle. The analysis results of the overwrap case study show excellent agreement with experimental hoop strain data. The fabrication stresses from the analysis indicate that the overwrap should experience no strength degradation due

to adverse fabrication stresses and strains. Very favorable residual stress results were also predicted by the model for the overwrap.

The analysis results of the bottle case study, while having no experimental data to compare with, show very reasonable behaviors, which can be readily explained by a qualitative consideration of the actual winding problem. The stress and strain results from the case study show that the bottle would experience strength degradation when a sand/PVA mandrel is used, but it would retain maximum strength when a steel mandrel is used.

Acknowledgements

I would like to express my gratitude toward Dr. Charles E. Knight for his guidance and supervision during the completion of this work. His readily available help, infinite patience, and generous tolerance for my procrastination are deeply appreciated. I am especially indebted to Dr. Knight for the invaluable experience gained from working under him and for the model he provides of how to be an engineer and a gentleman.

Thanks are due to Dr. Mabie, Dr. Mitchiner, Dr. Fries, and Dr. Loos for serving on my committee. Special thanks are in order for Dr. Loos for his readiness to help and to advise whenever I have problems with my research. I also appreciate Jerome Tzeng's promptness in supplying the data I needed for my research.

I would also like to thank my parents, Mr. and Mrs. Thung D. Nguyen, my brothers Tien and Thang, and my sisters-in-law Kim Anh and Dieu Hien for their love and encouragements, without which this work would not be possible. I am grateful for my sister Vuong Anh's support and understanding in the last months of this work. She is appreciated more than she realized. And thanks to her friend Lam for letting me borrow his personal computer. It was a lot of help. Also, I am indebted to my

adopted sister Le Thi Tuong Van for spending hours on end listening to my confidences and for offering very sound advices.

I would like to thank my friends Nguyen Anh Hao, Men-Fung Chin, Ed and Michelle Moas, Nour and Alice Tira, Bob and Lisa Williams, Pham Huu Chi, Arun Veeraraghavan, Sung-Hwan Chung, and many others who have made my stay in Blacksburg more pleasant than it would have been. You are the truest friends anyone could ask for. Also, thanks are due to my loyal lifting partner Terry Martin. You are a lot of help and a lot of fun. Workouts will never be the same with another partner.

Finally, I would like to thank my very dear friend Tran Ngu Nhu La for her unending love and wonderful company. Despite your young age, you taught me more about love and life than anybody else I have known; and you have changed my life for the better. More than for anyone else, this one is for you.

Table of Contents

List of Illustrations

List of Tables

Chapter 1

Introduction

In the past two decades, filament winding has become an increasingly popular method of fabricating composite structures. Filament wound structures are easy to fabricate and, because of the continuous reinforcing fibers, have higher strength and stiffness to weight ratios than their metal counterparts. For these reasons, filament winding has found wide applications in the medical technologies, as well as in the aerospace and military industries. Recent advances in the filament winding technology such as the development of new winding machinery and interfacing with CAD/CAM systems have further contributed to the popularity of filament winding by allowing the fabrication of larger and more complex parts. The most recent developments using these technologies include filament wound pressurized gas containers, door springs for the Boeing 767, and the launch tube for the MX missile.

Despite all these advances, as yet very little is known about the relationship between fabrication process variables and the performance of the end product. As a result, the manufacturing process is still mainly a process of trial and error. Process

variables are often selected empirically and used to fabricate subscale parts which are then tested for performance. If the subscale parts prove unsatisfactory, the process variables are varied until satisfactory performance is achieved. This manufacturing method is very costly and time consuming. Furthermore, the performance of the subscale parts in many cases is not indicative of the performance of the full scale parts. Often, the process variables which produce satisfactory subscale parts may produce full scale parts which are nonuniformly cured and have a high void content, resulting in a degradation of strength. Because of these economic and technical problems, it is desirable to have an analysis tool to enable the prediction of the composite structure's performance from the fabrication process variables analytically, thus reducing the need for subscale parts and the scaleup problem.

The prediction of the composite structure's performance may be assessed by looking at the fiber strains at cure and at the residual fiber stresses. If the fibers have tensile strains during cure, they will be straight and aligned in the cured composite, giving it the maximum strength. Whereas, a state of compressive strain in the fibers during cure means local buckling of the fibers, resulting in a loss of strength in the final product. Also, the radial component of the residual stresses, i.e., the interlaminar normal stress, determines the possibility of layer delamination and/or separation of the composite layers from the mandrel. The latter phenomenon is of great importance if the mandrel is an integral part of the final structure.

Thus, if the fiber stresses and strains during fabrication are known, one can predict the strength of the final product, if not quantitatively then at least qualitatively. Therefore the purpose of the fabrication stress model should be to compute the fiber stresses and strains at any time in the fabrication process from the process variables such as the winding tension, the winding pattern, and the cure cycle. By calculating the cumulative fiber stresses, the fabrication stress model also yields the residual

stresses in the composite structure after fabrication. These stresses may need to be included in the computation of the total stresses in the structure for external loadings.

The fabrication stress model is developed for axisymmetric structures since most filament wound structures have axisymmetric configurations. The model uses an axisymmetric finite element formulation modified to account for material property anisotropy. All materials involved in the fabrication process, namely the mandrel material, the insulation material, and the composite material, uncured and cured, can be assumed to behave as elastic systems. The viscoelastic nature of the uncured composite material may be approximated by the inclusion of fiber motion in the form of tension loss in the fibers (as a result of the fiber motion).

In order to simulate the fabrication process accurately, the fabrication stress model needs to be divided into three separate stages corresponding to the actual fabrication stages: winding, curing, and mandrel removal. The winding stage can be modeled as a modified incremental construction problem. However, modifications should be made to accommodate the fact that the final stress level in the layer being wound, instead of the initial stress level, is known. The curing stage can be modeled as a thermal expansion problem with a material transition associated with the curing of the composite material. Finally, the mandrel removal stage can be modeled simply as a removal of prestressed material. In these stages, important phenomena such as the difference in the mechanical behavior of the uncured and cured materials, the various tension losses in the winding process, the fiber motion in the uncured or partially cured material, and the stress redistribution due to changes in material properties from step to step should also be taken into account.

The simulation of these stages, along with the modeling of the physical phenomena occurring in each stage, will be discussed in detail in Chapter 5. First, however, a brief review of the works done which led to or are related to the stress

model is presented in the literature review of Chapter 2, followed a theoretical consideration of the actual fabrication process and an overview of the fabrication stress model in Chapter 3. A review of the axisymmetric finite element formulation and an outline of the material properties transformations are presented in Chapter 4. Chapter 6 will outline the implementation of the fabrication stress model in a finite element code WACSAFE. In that chapter, only the significant features of the implementation will be described. Finally, two case studies will be presented in Chapter 7 as sample analyses, as well as a means for evaluating the model.

Chapter 2

Literature Review

The popularity of filament wound structures has inspired the development of many stress analysis programs for filament wound structures, especially axisymmetric structures. Examples of these programs are the works of Chen and Clewlow [1], Gerstle [2], Patel and Kennedy [3], and Knight [4]. However, most programs analyze only the fabricated structure and consider only the stresses due to external loadings on the structure, with disregard for the residual fabrication stresses, which in some cases can be a significant portion of the total stresses in the structure. Also neglected is the influence of the fabrication stresses at cure on the strength of the final product.

A reason for this may be the complications encountered in trying to analyze the fabrication process. Many researchers have for a long time considered the fabrication process, and particularly the winding process, to be an "inexact science". As a result, very little work has been done in the analysis of the fabrication stresses. In fact, the author is aware of only two related works which deal with the computation

of fabrication stresses from fabrication process variables. The first work, by Leavesley and Knight [5], is a stress model specialized for spherical pressure vessels and computes the fiber stresses and strains only in the winding stage. The model uses an axisymmetric finite element formulation with the assumption that on the average, there is no twisting about the structure's axis of symmetry. The second work, by Johnson and Knight [6], is an extension of the previous model and carries the analysis through the curing stage also. This latter model is also generalized for any axisymmetric geometry. These models served as the basis for the fabrication stress model in this dissertation and they are discussed below, along with other literature dealing with or related to the three stages of the fabrication process.

Tarnopol'skii and Beil' [7] proposed perhaps the first winding stress model. In their model, composite layers are treated as prestressed orthotropic rings which are added to the mandrel one at a time to simulate winding of the layers. The stress, strain, and displacement increments are taken from the elasticity solution of the concentric rings problem. The authors showed that the mandrel pressure obtained from the model displays the same characteristic variation with the composite wall thickness as observed in experimental data. They also contend that while this model provides a closed form solution, its simplicity makes it applicable only to problems with simple ring geometries.

For more complex geometries, the winding process is analogous to the incremental construction problem of earth dams and embankments studied by researchers such as Clough and Woodward [8] and Brown and King [9]. These authors proposed a simulation of the incremental construction problem using an incremental finite element formulation. As a new layer of material is added, the structural stiffness matrices of the elements in this layer are added to the existing structure's stiffness matrix and the dead weight of the new layer is converted into nodal loads on the modified

structure. The incremental stresses and strains resulted from the addition of the new layer are added to the cumulative stresses and strains in the structure. The authors showed that the incremental construction problem is highly nonlinear and depends strongly on the construction history. Therefore, the simulation must be done in as many steps as in the actual construction process to assure accuracy of the results.

The winding problem is slightly different from the dam construction problem. In the dam construction problem, the stress state in the new layer is determined solely by the dead weight of the layer. The displacement of the structure underneath contributes only a free body motion in the new layer, and thus cannot affect the stress state in the layer. In the winding problem, however, the stress state in the new layer, in addition to being determined by the winding tension, is also affected by the displacement of the structure underneath because of the axisymmetric nature of the problem. To further complicate the problem, the given winding tension is not the initial stress state but the final stress state in the new layer, after the layer has been wound and the altered structure allowed to adjust to a new state of equilibrium. Thus, to model the winding process, one has to formulate the problem such that the final stress state in the new layer is equal to the given winding tension. To get around this difficulty, Leavesley and Knight [5] reduced the fiber direction stiffness of the new layer to the transverse value so that virtually all of the loads are supported by the underlying structure, rendering stress increments in the new layer negligible. As a consequence, the final stress state in the new layer is very close to and can be approximated by the winding tension.

In addition to different material properties, Johnson and Knight [6] characterized the mechanical aspect of curing by different material behaviors in uncured and cured states. The modeling of these different mechanical behaviors is based on the existence of two layers of equal and opposite winding angles at any point in a filament

wound structure. The authors used a composite element containing both of these layers and computed the element structural stiffness matrix from the structural stiffness matrices of the layers. When the material is uncured, the layers are assumed to be free to slide with respect to each other. This assumption led to the averaging of the layer compliance matrices to get the element compliance matrix, which is then inverted to obtain the stiffness matrix. On the other hand, when the material is cured, the layers are assumed to be rigidly bonded together. As a result, the authors averaged the layer material stiffness matrices to get the element stiffness matrix.

The gradual transition of the material from the uncured state to the cured state in the curing process was not accounted for in Johnson and Knight's model. Instead, the authors assumed that the material switches from uncured to cured instantaneously at the end of the heatup step.

The mandrel removal problem is identical to the excavation problem widely studied in the field of civil engineering. Both problems involve the removal of prestressed material from a structure. Early researchers such as Duncan and Clough [10] and Duncan and Dunlop [11] modeled the excavation problem by removing the stiffness of the excavated material and applying a negative traction on the excavation surface equal to that exerted by the excavated material on the remaining portion, in the form of nodal loads. These researchers calculated the nodal loads on the excavation surface by extrapolating the element stresses to the boundaries and then distributing them to the nodes by some weighted averaging method.

Christian and Wong [12] showed that the results obtained from these early models depend on the number of excavation steps even for linearly elastic systems, and thus are in serious error. They also demonstrated that the errors in the solutions build up with the number of excavation steps. Intuitively, one would expect the sol-

ution of the excavation problem to be path independent for a linearly elastic structure. As a matter of fact, Ishihara [13] proved analytically that the end results of an excavation problem are independent of the construction history for a linearly elastic material. Christian and Wong attributed the errors in these methods to the inability of the finite element method to model adequately the stress gradients near the toe of the excavation. Their refinement using least square polynomial extrapolation could only reduce but not eliminate the discrepancies.

More recently, Ghaboussi and Pecknold [14] speculated that the errors in the earlier methods arose from the calculations of the nodal loads on the excavation surface. The authors stated that these methods of calculation yielded a set of inconsistent nodal loads. As an alternative, they proposed using a consistent formulation for the computation of the nodal loads due to excavation from the element stresses in the remaining structure:

$$\{R\} = \sum \int_V [B]^T \{\sigma\} dV \tag{2.1}$$

where $\{R\}$ is the nodal load vector due to excavation,

$[B]$ is the nodal displacements-strains matrix, and

$\{\sigma\}$ is the element stress tensor.

The summation in equation (2.1) is over all the remaining elements. The authors showed numerically that this method yields results that are independent of the number of excavation steps.

Chandrasekaran and King [15] proposed another method of modeling the excavation process. They computed the nodal loads on all future excavation interfaces from the element stresses at the start of the simulation. Then, these nodal loads

were updated using the interface displacements after each excavation step. For example, suppose the finite element model in Fig. 1 undergoes a three-step excavation. The elements to be removed in each step are above the $A-A-A$ interface, between the $A-A-A$ and $B-B-B$ interfaces, and between the $B-B-B$ and $C-C-C$ interfaces, respectively.

At the start of the simulation, the excavation nodal loads on all three interfaces are computed from the stresses in the elements directly above each interface. After the interface nodal loads have been computed, the excavation simulation proceeds as follows.

In the first step, the elements above $A-A-A$ are deactivated and the nodal loads on the $A-A-A$ interface are activated as external loads on the remaining structure. Then, the incremental nodal displacements of the nodes on interfaces $B-B-B$ and $C-C-C$ due to the excavation loads on $A-A-A$ are multiplied with the proper rows in the structural stiffness matrix to obtain the incremental excavation loads which are then used to update the excavation loads on these surfaces.

The next step involved turning off all elements above the $B-B-B$ interface and using the updated nodal loads on $B-B-B$ as the excavation loads. The incremental nodal displacements due to these loads are again used to update the excavation loads on $C-C-C$ and the same procedure is repeated. In each step, only the stresses and strains in the final structure need to be updated. The authors demonstrated numerically that the results obtained by this method are independent of the number of excavation steps.

The methods proposed by Ghaboussi and Pecknold [14] and Chandrasekaran and King [15] should yield identical results. The consistent nodal load computed according to the former method should be equal to those computed from the displacements in the latter method because a consistent relationship between nodal displacements

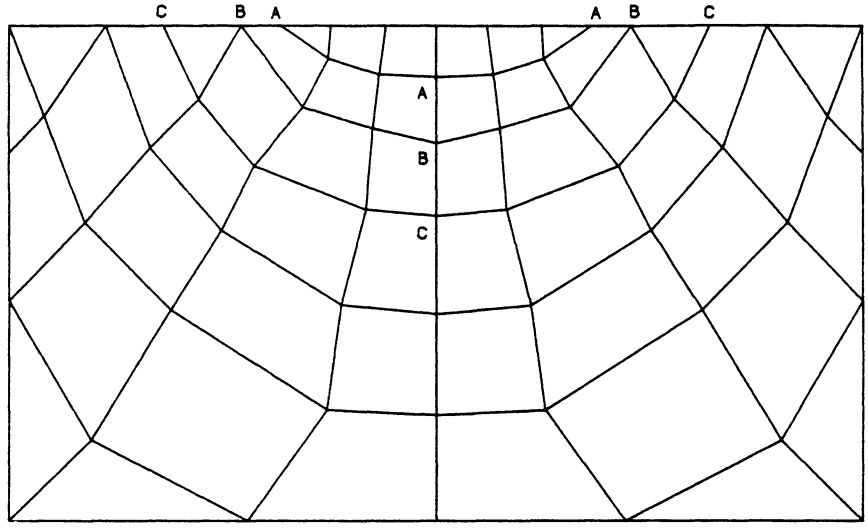

Figure 1. Finite Element Mesh of Typical Excavation Problem

and element stresses was used in both methods. The latter method, while bypassing the updating of the stresses in the elements to be excavated altogether, requires the tracking of the nodal forces on all future excavation surfaces. For this reason, the former method appears simpler and easier to implement.

The fabrication stress model in this dissertation is based on some of the literature discussed above, namely the works of Leavesley and Knight [5], Johnson and Knight [6], and Ghaboussi and Pecknold [14]. Modifications are made to these models to account for three major effects: fiber motion, tension loss due to multiple circuit winding, and the material transition from uncured state to cured state. The theories behind the model formulation and the numerical implementation of the model are discussed in the subsequent chapters.

Chapter 3

Overview of Fabrication Stress Model

Before the fabrication process can be accurately modeled, the mechanics of the winding, curing, and mandrel removal processes must be understood. In particular, it is necessary to examine all the physical phenomena occurring in the fabrication stages which significantly affect the stress state in the fibers. For this reason, the first section of this chapter will present a brief theoretical consideration of the fabrication process, discussing the typical process and the important physical phenomena occurring in each stage of fabrication. From this, the general structure of the fabrication stress model can be organized, the overview of which will be given in the second and last section of the chapter.

3.1 Actual Fabrication Process

A typical wet winding process is depicted in Fig. 2. Fibers are collected from spools to form a fiber band, which is passed through a resin reservoir where the band picks up the resin before being laid onto a rotating mandrel. This mandrel is usually made of metal but sometimes is a composite structure itself. The crossfeed motion of the arm can be controlled to give the desired winding angle.

There are two major categories of winding patterns, depending on the magnitude of the winding angle. When the winding angle is large such that the winding is essentially from pole to pole, it is called polar winding. When the winding angle is small so that the fiber bands wrap around more than half a turn from pole to pole, it is called helical winding. In either winding pattern, a layer is always accompanied by another layer with equal and opposite winding angle.

Another type of winding is called prepreg winding where the fiber bands are preimpregnated with resin. The prepreg winding process is similar to the wet winding process, except there is no resin pickup.

After winding, the structure, i. e., the mandrel plus the composite layers, is put through a cure cycle, which usually involves controlled heating for a prolonged period of time. During heating, the composite material undergoes a gradual transition from uncured state to cured state. This transition, or curing of the composite, involves heat induced chemical reactions which transform the resin from a viscous fluid into a solid. At the end of heating, the composite layers will have been cured if the proper cure cycle was selected. Then, the structure is allowed to cool and the mandrel is removed if necessary.

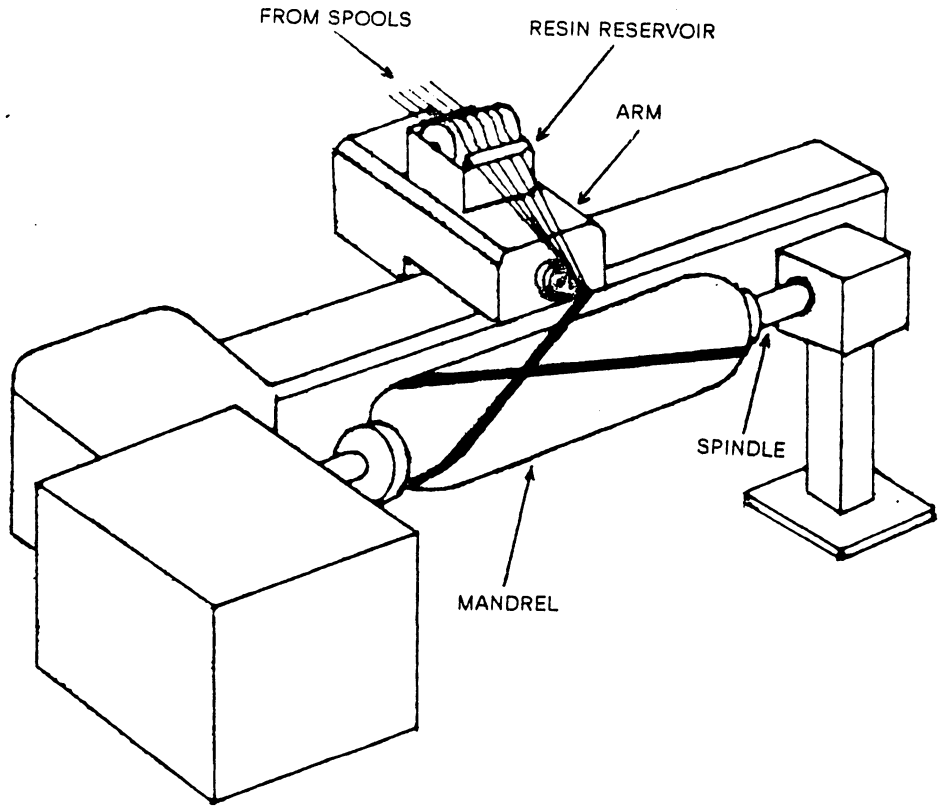

Figure 2. A Typical Wet Winding Process

In the winding stage, there are two major factors affecting the stress state in the fibers: the sequential winding of the layers and various types of tension losses. The first factor, the winding of the layers, can be looked at from an elasticity point of view as follows: when a new layer is added, its winding tension acts as external forces on the underlying structure, causing a shrinkage. This shrinkage, which is purely due to the elastic behavior of the structure, drives the inner layers inward, resulting in a reduction in tension.

Aside from this tension reduction, there are three other sources of tension losses: instantaneous tension loss, tension loss due to multiple circuit winding, and tension loss due to fiber motion (or resin migration). The first two types of tension losses are caused by the mechanics of the winding process itself. The last type occurs because of the viscous nature of the resin in the uncured material.

The instantaneous tension loss occurs when the fiber band is laid onto the mandrel. It is caused by, among other things, the flattening of the fiber band and instantaneous resin flow due to sudden application of pressure on the band. As a result, the winding tension (the tension in the fiber band after it is laid onto the mandrel) is less than the spool tension (the tension in the fibers as they leave the spools). The spool tension is measured as a process control, but the actual applied winding tension must be obtained through experiment as a function of spool tension.

The multiple circuit winding of the layers results in the second type of tension loss. In a typical winding process, each layer of complete surface coverage consists of several circuits which are wound in sequence with a sideways offset. The tension loss due to this type of winding is explained here in a qualitative manner.

A typical circumferential multiple circuit winding process is illustrated in Fig. 3. When the first circuit is wound, the full winding tension is retained in the circuit due to the continuity of the fibers within the circuit, and a small mandrel displacement

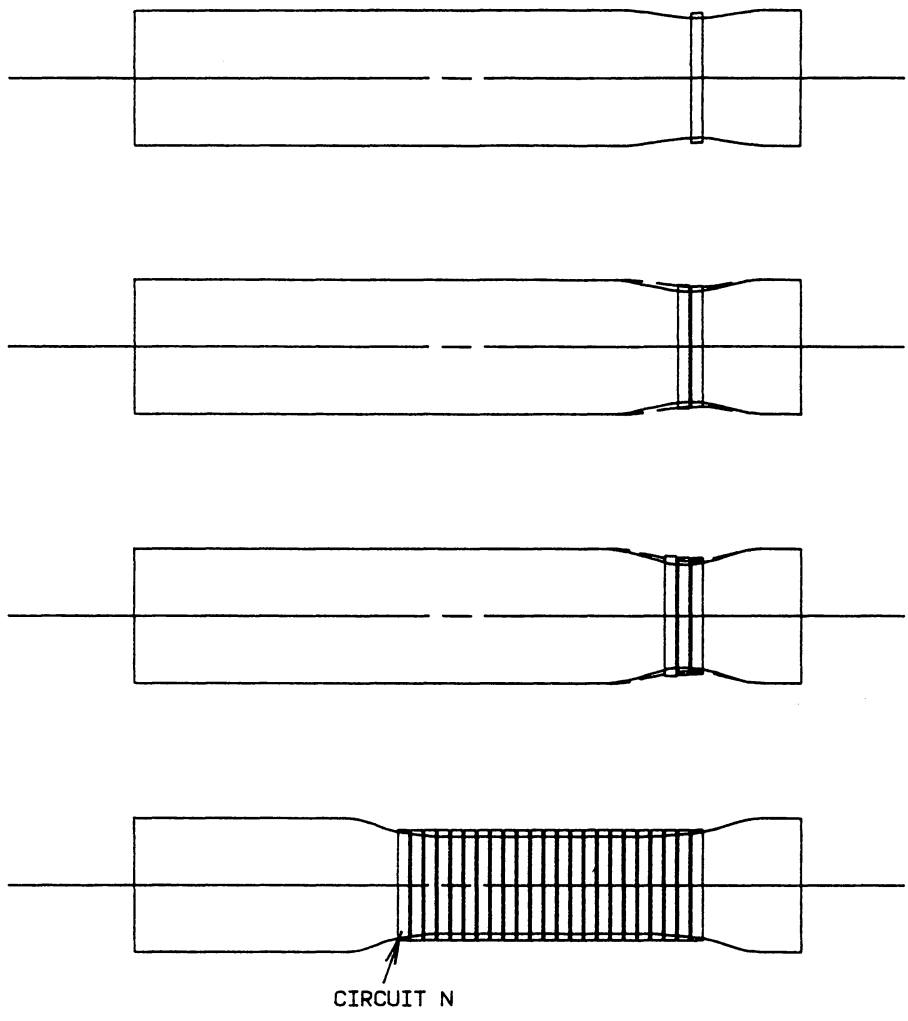

Figure 3. Multiple Circuit Winding Process

occurs. When the second circuit is wound next to the first circuit, it generates a displacement field which drives the first circuit inward along with the mandrel. This inward motion causes a tension loss in the first circuit. Similarly, when the third circuit is wound, both the first circuit and the second circuit are displaced inward, resulting in tension losses in both. The additional tension loss in the first circuit due to the winding of the third circuit is less than the tension loss in the second circuit because of the greater distance away from the third circuit. As the winding of subsequent circuits goes on, the first circuit will lose more and more tension but the incremental tension losses will be smaller each time. When circuit N, far enough away from the first circuit, is wound, its effect on the first circuit is negligible. Thus, after the winding of all circuits, barring end effects, most of the circuits will have lost the same amount of tension assuming the distance of each circuit's influence is much smaller than the spacing required for a full layer of coverage.

The last type of tension loss is due to the radial motion of the fibers through the viscous resin. The fiber tensions generate a pressure gradient in the layers which drives the resin outward. Accompanying this outward resin flow is an inward motion of the fibers to occupy the space left by the displaced resin. This inward motion of the fibers causes a loss in the fiber tensions.

Another phenomenon occurring in the uncured material is the stiffness degradation when the fibers are driven into a state of compression. The very small diameter fibers cannot support compressive loads. Therefore, when a layer loses all tension, the resin becomes the principal load carrying component, and, as a result, the stiffness of the uncured composite in the parallel fiber direction becomes nearly equal to the transverse fiber direction.

Notice that this stiffness degradation and the fiber motion described above are uncured phenomena. Therefore, their presence is not restricted to the winding stage

alone but they occur whenever the material is uncured or only partially cured. In particular, they are significant factors in the first stage of the cure cycle when the resin viscosity decreases rapidly and is beginning to cure.

In the curing stage, the fiber stresses are also influenced by the temperature changes in the structure during heatup and cooldown. The mandrel, if it has a higher coefficient of thermal expansion than the composite, expands and drives the composite layers outward radially and into higher tension. Also, the local variations in the temperature distribution and the difference in the composite layers' coefficients of thermal expansion (because of the different winding angles) give rise to local variations in the stress field.

Occurring simultaneously with this thermal expansion is a drastic decrease in the viscosity of the resin associated with elevated temperatures. The decrease in the resin viscosity allows greater fiber motion, consequently reducing the fiber tension. The viscosity will begin to rise again only when the material starts to gel. After that, the thermal expansion becomes dominant.

Also occurring in the heatup step is a gradual transition of the material from uncured state to cured state. This transition introduces a change in the engineering properties and the mechanical behavior (due to material transition from uncured to cured). In the cooldown step, the composite layers are completely cured and the only source of change in fiber stress is the thermal shrinkage of the composite layers and the mandrel.

The mandrel removal stage occurs if the mandrel is not an integral part of the final structure. Before removal, if the mandrel is compressed by the composite layers and thereby maintaining a surface contact, the stress field in the mandrel generates a pressure on the mandrel-composite interface. The removal of the mandrel takes away this interface pressure. As a result, the stresses in the composite layers

will have to adjust to a new state of equilibrium. If the shrinkage in the mandrel is greater than that in the composite layers, then the mandrel will separate from the composite layers. In the mandrel removal stage, the material is completely cured, and the behavior can usually be assumed to be linearly elastic.

3.2 Overview of Fabrication Stress Model

The fabrication stress model, like the fabrication process itself, is divided into three stages: winding, curing, and mandrel removal. Each stage of the model is a combination of a base model and several submodels for the various physical phenomena occurring in each stage, as discussed in the previous section.

Figure 4 shows a block diagram of the fabrication stress model. Some of the submodels are common to more than one fabrication stage. Each model is shown in Fig. 4 with the number of the section where it will be discussed (except the thermokinetic cure model, which is the subject of a concurrent research effort carried out by Loos et al. [16]).

The base model of the winding stage is the winding simulation (incremental construction simulation). Three major phenomena affecting the fiber stress during the winding stage are the instantaneous tension loss, the tension loss due to multiple circuit winding, and the fiber motion. These phenomena are accounted for in the winding stage simulation by their respective models. Also, uncured material formulation (discussed in next chapter) is used for the winding stage, when the material is assumed to be completely uncured.

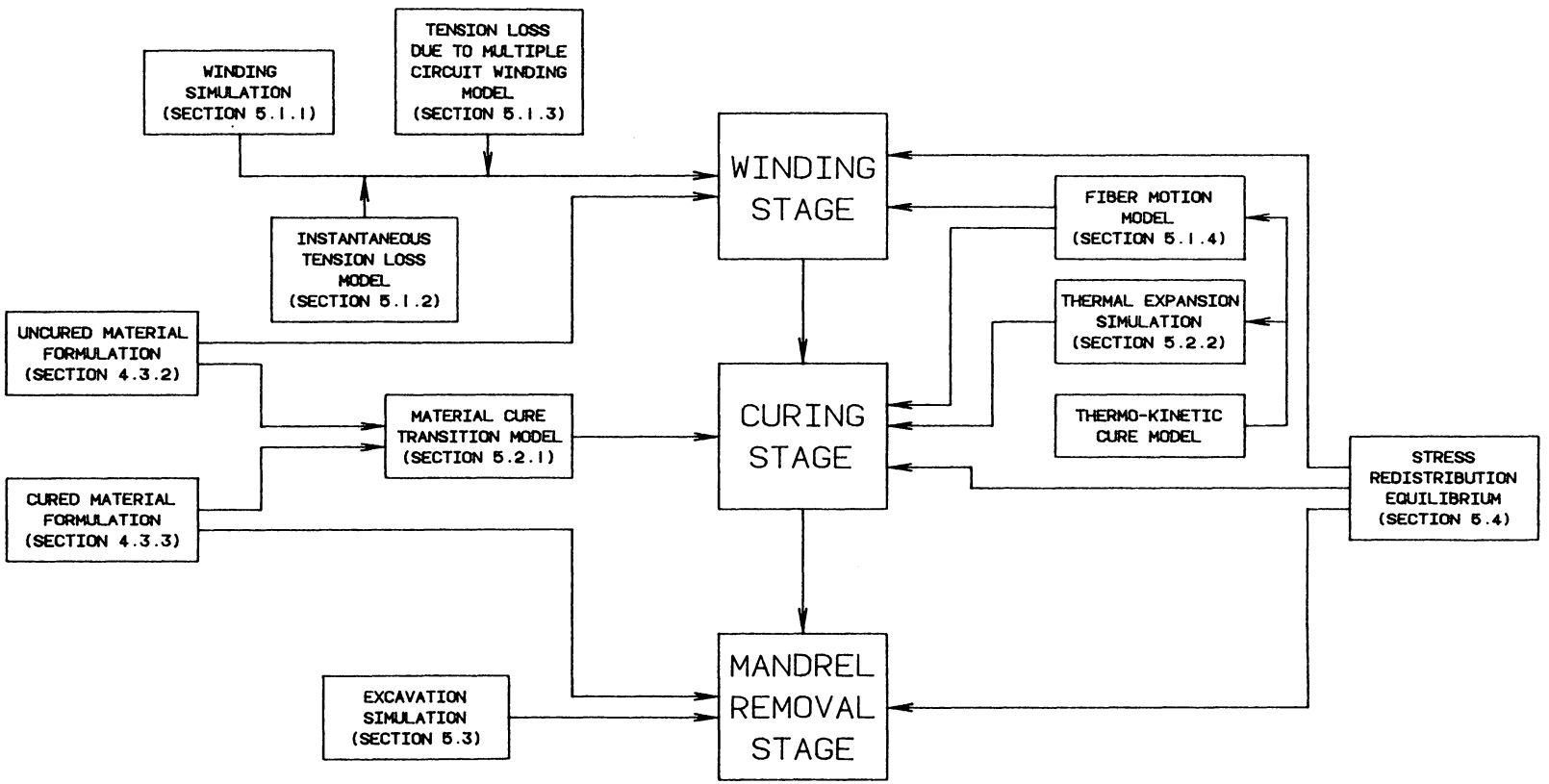

Figure 4. Block Diagram of the Fabrication Stress Model

The base model of the curing stage is the thermal expansion simulation. The major phenomena in the curing stage are the fiber motion and the material cure transition. The thermo-kinetic quantities for the thermal expansion simulation and the fiber motion model in this stage are supplied by the thermo-kinetic cure model.

The thermo-kinetic cure model, developed by Loos et al. [16], is a thermal analysis of the cure process. The model uses a thermal finite element formulation to compute the temperature profile, the cure state, and the viscosities in the composite layers as element values. These data are inputs to the fiber motion model and the thermal expansion model.

The material cure transition is accounted for by a material transition model, which interpolates the uncured and cured material formulations.

The base model of the mandrel removal stage is the excavation simulation. In this stage, the material is assumed to be completely cured and the cured material formulation is used.

The uncured or partially cured material formulation is used only for the composite material. For the mandrel material, the cured formulation is always used. The reason for this is that the cured formulation is valid for both isotropic and composite mandrels.

A stress redistribution equilibrium is included in all three stages to redistribute any unbalanced internal stresses in the structure. The stress redistribution equilibrium is especially needed in the winding stage when fiber stress may become compressive in the numerical model. Since the fibers cannot support compressive loads, the compressive stresses are unsupported and must be redistributed.

All the models shown in Fig. 4, except the thermo-kinetic cure model, will be discussed in details in the next two chapters.

Chapter 4

Finite Element Formulation

The fabrication stress model uses an isoparametric axisymmetric composite element. The formulation of this element is similar to the regular isoparametric axisymmetric element except for the calculation of the element material stiffness matrix. This material stiffness matrix is calculated in different ways, depending on the cure state of the material.

This chapter will present the formulation of the isoparametric axisymmetric composite element in two parts. First, a brief review of the general finite element method and the regular isoparametric axisymmetric formulation from a displacement based potential energy point of view is given in the next two sections. The discussions will be restricted to the class of elasticity problems with linearly elastic material behavior since the winding and curing processes will be treated as such. A more complete treatment of the finite element method can be found in finite element texts such as Zienkiewicz [17], Cook [18], Bathe [19], or Reddy [20]. The last section of the chapter is devoted to the calculations of the element material stiffness

matrix for uncured and cured materials. These calculations are based on the work of Johnson and Knight [6].

4.1 The Finite Element Method

The solutions of many elasticity problems cannot be obtained exactly due to the complexity of the governing differential equation and/or the domain of the continuum. Instead, approximate solution methods have to be employed. One such method is the displacement based finite element method, which is based on the principle of minimum potential energy: a system is in stable equilibrium if the potential energy of the system is at a minimum.

The finite element method discretizes a continuum into several elements of finite size, connected together at a number of node points on their boundaries. In the displacement based formulation, the displacement fields in the elements are approximated by functions of some assumed shape, usually a polynomial in terms of the coordinate variables. The order of the polynomial depends on how closely the actual displacement fields have to be approximated. When a first order polynomial is used, the element is called a linear element; when a second order polynomial is used, the element is called a quadratic element, and so on. A linear, two dimensional, quadrilateral element such as the one used by the fabrication stress model uses bilinear polynomials to approximate the displacement fields:

$$\begin{aligned} u(x,y) &= a_1 + a_2x + a_3y + a_4xy \\ v(x,y) &= b_1 + b_2x + b_3y + b_4xy \end{aligned} \tag{4.1.1}$$

where u, v are the displacement fields,

x, y are the coordinates variables, and

a_i, b_i are the coefficients of the polynomials.

The coefficients a_i and b_i can be written in terms of the nodal displacements by evaluating equations (4.1.1) at the nodes and then solving for the coefficients. In order to accomplish this, the number of nodes in each element has to be equal to the number of coefficients in the polynomial. Thus, an element with the approximate displacement fields given by equations (4.1.1) must contain four nodes.

After the coefficients have been solved for in terms of the nodal displacements, equations (4.1.1) can be rearranged so that the displacement fields u and v become functions of the nodal displacements:

$$u(x,y) = \sum_{i=1}^{4} N_i(x,y)u_i$$
$$v(x,y) = \sum_{i=1}^{4} M_i(x,y)v_i \qquad (4.1.2)$$

where u_i, v_i are the nodal displacements and N_i, M_i are called shape functions. Basically, the shape functions interpolate the nodal displacements to any point (x,y) inside the element.

By writing the approximate displacement fields in the form of equation (4.1.2), the elasticity problem can be formulated in terms of the nodal displacements only. In other words, the nodal displacements become the only unknowns in the final formulation. Therefore, the displacement based finite element method can be looked at as trying to compute a set of permissible nodal displacements which minimizes the potential energy of the system.

The potential energy of each element can be written as the sum of the strain energy and the work done on the element by external forces:

$$\Pi = \int_V U_o dV - \int_V \{f\}^T \{F\} dV - \int_S \{f\}^T \{\Phi\} dS - \{D\}^T \{P\} \qquad (4.1.3)$$

where U_o is the strain energy per unit volume,

$\{f\}$ are the displacement fields in the element,

$\{F\}$ are the body forces acting on the element,

$\{\Phi\}$ are the tractions on the element boundary,

$\{P\}$ are the concentrated loads acting on the element, and

$\{D\}$ are the displacements at the points of applications of $\{P\}$.

The first term is the strain energy term, and the remaining three terms are the work done by the body forces, the surface tractions, and the concentrated loads, respectively. The V subscript denotes integration over the volume of the element and the S subscript denotes the surface integration over the element boundary.

Since the displacements at any point can be written in terms of the nodal displacements, the potential energy functional in equation (4.1.3) can be converted into a function solely of the nodal displacements. Once this conversion is done, the potential energy functional can be partially differentiated with respect to the nodal displacements in order to obtain a minimum. The partial differentiations yield a set of independent equations for each element, relating the nodal forces to the nodal displacements:

$$[K]^e \{d\}^e = \{R\}^e \qquad (4.1.4)$$

where $[K]$ is the structural stiffness matrix,

$\{d\}$ is the nodal displacement vector, and

$\{R\}$ is the nodal force vector.

The e superscript denotes that the equation was formulated on element level. The expressions for $[K]$ and $\{R\}$ are obtained from the differentiations as:

$$[K] = \int_V [B]^T [D][B] dV \tag{4.1.5}$$

and

$$\{R\} = \int_V [B]^T [D]\{\varepsilon_o\} dV - \int_V [B]^T \{\sigma_o\} dV + \int_V [N]^T \{F\} dV + \int_S [N]^T \{\Phi\} dS \tag{4.1.6}$$

where $\{\varepsilon_o\}$ is the initial strain tensor,

$\{\sigma_o\}$ is the initial stress tensor,

$[D]$ is the element material stiffness matrix,

$[B]$ is the nodal displacements-strains matrix, and

$[N]$ is the matrix of shape functions.

The significance of $[B]$ and the expressions for $[B]$ and $[N]$ will be discussed in the next section.

The nodal force vector $\{R\}$ contains not only the nodal forces due to external loadings but also those exerted by adjacent elements in the form of boundary tractions. These latter forces are not known; therefore, the nodal displacements cannot be solved for directly from the individual element equation. Instead, the element equations for all elements have to be assembled into a global system of equations:

$$[K]\{d\} = \{R\} \tag{4.1.7}$$

The lack of the superscript e in equation (4.1.7) denotes the global nature of the equations.

The assembly process eliminates the unknown inter-element traction forces from the global system of equations since adjacent elements exert equal and opposite forces on each other, resulting in a net force of zero at the nodes. The assembly process also takes care of the boundary conditions by deleting the inactive nodal degrees of freedom from the global equations. As a result, equation (4.1.7) is an $n \times n$ system of equations, where n is the number of active degrees of freedom in the finite element model.

The global nodal displacement vector can now be solved for and the displacements at any point can be found through the shape functions, as discussed above. Once the displacements are found the strains and the stresses can be easily computed from the point-wise displacements-strains relations and the constitutive equations.

The next section presents the formulation of the isoparametric axisymmetric element. In particular, the expressions for the element structural stiffness matrix and the nodal force vector will be given for the isoparametric axisymmetric element.

4.2 Axisymmetric Isoparametric Formulation

Figure 5 shows a typical axisymmetric element in the cylindrical (global) coordinate system *rzt*. The *r* axis is the radial direction. The *z* axis is the longitudinal di-

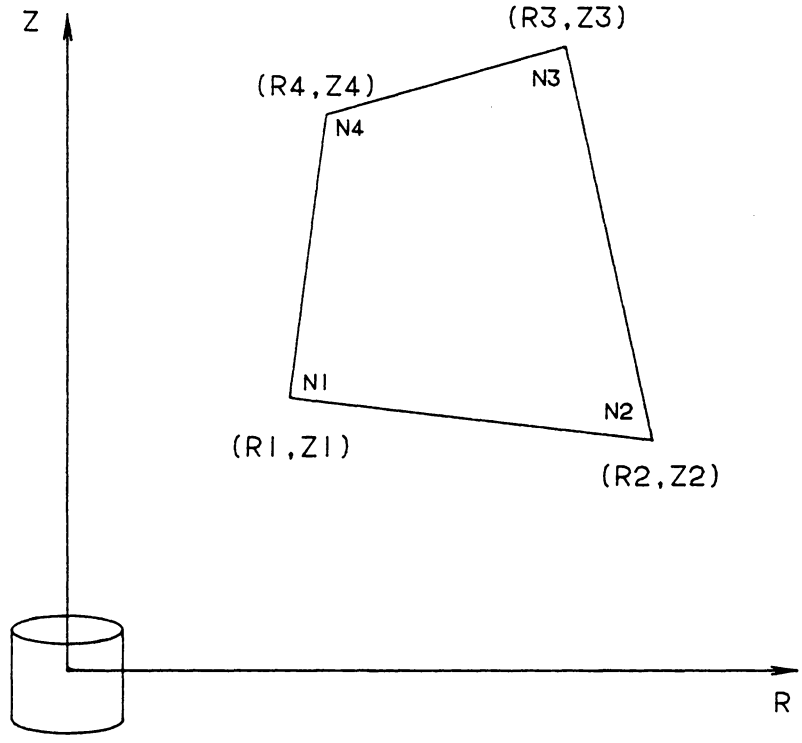

Figure 5. An Axisymmetric Element in the Global Coordinate System

rection and also the axis of symmetry. The t axis, not shown, is the tangential direction. The axisymmetric element is actually a ring element with the cross-section shown in the figure. Since all quantities are invariant in the tangential direction in the axisymmetric formulation, only one cross-section is needed to represent the whole ring.

The arbitrariness of the element shape in the global coordinate system makes the exact evaluation of the integrals in equations (4.1.5) and (4.1.6) very difficult, if not downright impractical. It is therefore necessary to map the element domain onto a master element with a regular domain, where the integrations can be carried out numerically. The mapping is performed via the mapping functions which correlate each point in the global domain to one and only one point in the master domain. The mapping functions for quadrilateral domains are usually polynomials, as in the case of the approximate displacement fields. Furthermore, when the mapping functions are of the same order as the approximate displacement fields, the formulation is called isoparametric.

The master element for linear quadrilateral elements is shown in Fig. 6 as a square domain in the intrinsic coordinate system $\xi\eta$. The center of the element is located at the origin of the coordinate system and the coordinates of the corners are (1,1) , (1, − 1), (−1, − 1), and (−1,1). Numerical integrations over this square domain can be easily carried out using a Gauss quadrature. Therefore, equations (4.1.5) and (4.1.6) need to be formulated in the intrinsic coordinate system.

In the intrinsic coordinates, the shape functions in equation (4.1.2) become the Lagrange interpolation functions:

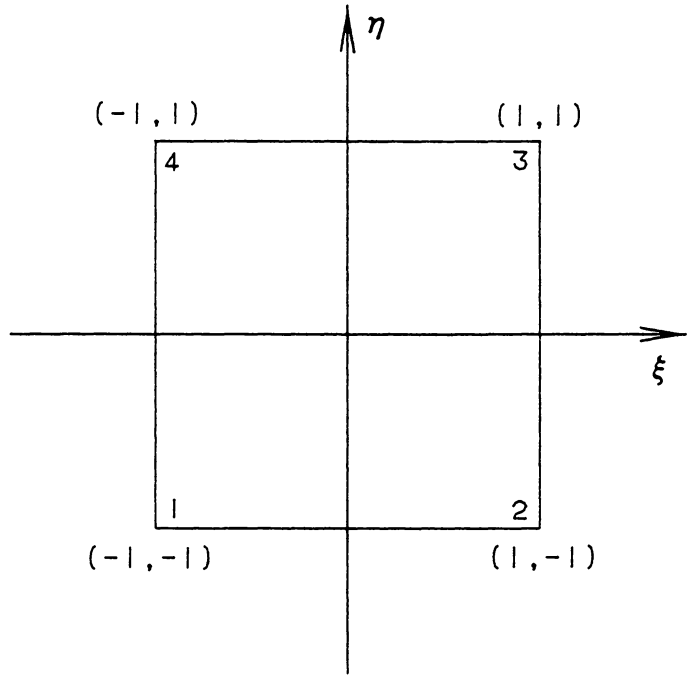

Figure 6. Master Element in the Intrinsic Coordinate System

$$
\begin{aligned}
N_1 &= \frac{1}{4}(1-\xi)(1-\eta) \\
N_2 &= \frac{1}{4}(1+\xi)(1-\eta) \\
N_3 &= \frac{1}{4}(1+\xi)(1+\eta) \\
N_4 &= \frac{1}{4}(1-\xi)(1+\eta)
\end{aligned}
\tag{4.2.1}
$$

The same set of functions can be used for both ξ and η directions since there is essentially no difference between the two directions. Thus, the displacements at any point (ξ, η) can be calculated from the nodal displacements and the shape functions as:

$$
\begin{aligned}
u(\xi, \eta) &= \sum_{i=1}^{4} N_i(\xi, \eta) u_i \\
v(\xi, \eta) &= \sum_{i=1}^{4} N_i(\xi, \eta) v_i
\end{aligned}
\tag{4.2.2}
$$

where $u(\xi, \eta)$, $v(\xi, \eta)$ are the displacements at point (ξ, η),

u_i, v_i are the nodal displacements, and

$N_i(\xi, \eta)$ are the shape functions evaluated at (ξ, η) .

Also, for the isoparametric formulation, the mapping functions become identical to the shape functions in the intrinsic coordinates. Therefore, the global coordinates of any point (ξ, η) are calculated in the same fashion as the displacements:

$$
\begin{aligned}
r(\xi, \eta) &= \sum_{i=1}^{4} N_1(\xi, \eta) r_i \\
z(\xi, \eta) &= \sum_{i=1}^{4} N_i(\xi, \eta) x_i
\end{aligned}
\tag{4.2.3}
$$

where $r(\xi, \eta)$ and $z(\xi, \eta)$ are the global coordinates of point (ξ, η),

r_i and z_i are the nodal coordinates, and

$N_i(\xi, \eta)$ are the same shape functions as in equation (4.2.2).

Written in matrix notation, equations (4.2.2) become:

$$\begin{Bmatrix} u \\ v \end{Bmatrix} = \begin{bmatrix} N_1 & 0 & N_2 & 0 & N_3 & 0 & N_4 & 0 \\ 0 & N_1 & 0 & N_2 & 0 & N_3 & 0 & N_4 \end{bmatrix} \begin{Bmatrix} u_1 \\ v_1 \\ u_2 \\ v_2 \\ u_3 \\ v_3 \\ u_4 \\ v_4 \end{Bmatrix} \tag{4.2.4}$$

or

$$\{f\} = [N]\{d\} \tag{4.2.5}$$

where $\{f\}$ is the displacement vector,

$[N]$ is the matrix of shape functions, and

$\{d\}$ is the nodal displacement vector.

Notice that only two displacement components are considered in equation (4.2.4). The reason for neglecting the third component is that the axisymmetric formulation assumes both the geometry and the loading to be axisymmetric. Thus, for no twisting about the axis of symmetry, the *rt* and *zt* components of the shear stresses and shear strains are always zero. As a result, only two displacement components, namely the *u* and *v* displacements, are needed to define the strain state, and subsequently the stress state, at any point:

$$\begin{Bmatrix} \varepsilon_r \\ \varepsilon_z \\ \varepsilon_t \\ \gamma_{rz} \end{Bmatrix} = \begin{bmatrix} \partial/\partial r & 0 \\ 0 & \partial/\partial z \\ 1/r & 0 \\ \partial/\partial z & \partial/\partial r \end{bmatrix} \begin{Bmatrix} u \\ v \end{Bmatrix} \tag{4.2.6}$$

or

$$\{\varepsilon\} = [P]\{f\} \tag{4.2.7}$$

where $\{\varepsilon\}$ is the strain tensor,

$[P]$ is the matrix of partial differentiations, and

$\{f\}$ is the displacement vector.

By combining equations (4.2.5) and (4.2.7), one can relate the strains to the nodal displacements directly:

$$\{\varepsilon\} = [P][N]\{d\} = [B]\{d\} \tag{4.2.8}$$

where $[B]$ is called the nodal displacements-strains matrix. The nodal displacements-strains matrix is a function of the coordinates and it enables the calculation of the strains at any point in the element once the nodal displacements are known.

The partial differentiations in equation (4.2.6) are with respect to the global coordinates. Since the problem is now formulated in the intrinsic coordinates, these partial differentiations have to be converted to differentiations with respect to the intrinsic coordinate variables ξ and η. The conversion of the differentiation variables is done through the chain rule:

$$\begin{Bmatrix} \partial/\partial r \\ \partial/\partial z \end{Bmatrix} = \begin{bmatrix} \partial r/\partial \xi & \partial r/\partial \eta \\ \partial z/\partial \xi & \partial z/\partial \eta \end{bmatrix} \begin{Bmatrix} \partial/\partial \xi \\ \partial/\partial \eta \end{Bmatrix} = [J] \begin{Bmatrix} \partial/\partial \xi \\ \partial/\partial \eta \end{Bmatrix} \tag{4.2.9}$$

where $[J]$ is the Jacobian matrix of the mapping. After the coordinate transformations, the nodal displacements-strains matrix has the form:

$$[B] = \begin{bmatrix} J^*_{11}\partial/\partial \xi + J^*_{12}\partial/\partial \eta & 0 \\ 0 & J^*_{21}\partial/\partial \xi + J^*_{22}\partial/\partial \eta \\ 1/r & 0 \\ J^*_{21}\partial/\partial \xi + J^*_{22}\partial/\partial \eta & J^*_{11}\partial/\partial \xi + J^*_{12}\partial/\partial \eta \end{bmatrix} \tag{4.2.10}$$

where J^*_{ij} are the entries of the inverted Jacobian matrix.

Finally, the expressions of $[K]$ and $\{R\}$ in the intrinsic coordinate system are:

$$[K] = \int_{-1}^{1} \int_{-1}^{1} [B]^T [D][B] r J d\xi d\eta \tag{4.2.11}$$

$$\begin{aligned} \{R\} = &\int_{-1}^{1} \int_{-1}^{1} [B]^T [D]\{\varepsilon_o\} r J d\xi d\eta - \int_{-1}^{1} \int_{-1}^{1} [B]^T \{\sigma_o\} r J d\xi d\eta \\ &+ \int_{-1}^{1} \int_{-1}^{1} [N]^T \{F\} r J d\xi d\eta + \int_S [N]^T \{\Phi\} dS \end{aligned} \tag{4.2.12}$$

where r is the radial coordinate, and

J is the determinant of the Jacobian matrix.

The volume integrals in equations (4.2.11) and (4.2.12) can be easily evaluated using Gauss quadrature. For a linear element, a two-point Gauss quadrature is sufficient for the accurate evaluation of these integrals. A special case occurs when a triangular element is formed by collapsing two adjacent nodes of a quadrilateral element.

In this case, a one-point Gauss quadrature is used to avoid the artificial stiffening of the collapsed edge.

4.3 Material Formulation

As discussed in the previous chapter, the nature of the filament winding process dictates the existence, at any point, of two layers of equal and opposite winding angles. The relative motion of these layers is assumed to determine the material behavior under different cure states: the layers are free to slide along each other when uncured and rigidly bonded together when cured. In order to model these behaviors, the composite element is made to contain both layers. As a result, the calculation of the element material stiffness matrix $[D]$ for the composite element involves, first the calculation of the material stiffness matrix or the compliance matrix for each layer in the fiber coordinates from the engineering properties, and then the calculation of the element material stiffness matrix in the global coordinate system from the layer stiffness or compliance matrices. The first calculation is simple and can be found in any textbook on composite materials. Therefore, only the second calculation is discussed in this section, after a review of the general coordinate transformations for the stress and strain tensors, and for the compliance and stiffness matrices.

4.3.1 General Transformations

Figure 7, taken from Leavesley and Knight [5], shows a typical fiber band wound on a mandrel. Three coordinate systems are shown in the figure: the global coordinate system *rzt*, the local coordinate system *stn*, and the fiber coordinate system 123. The orientation of the fiber band is completely defined by two angles. The first angle is the wrap angle *BETA*, which is defined as the angle between the fiber direction and the longitude. This angle is also the angle between the 1 direction of the fiber coordinate system and the *s* direction of the local coordinate system. The second angle is the polar angle *SETA*, which is defined as the angle between the vector normal to the surface of the fiber band and the horizontal plane. This angle is also the angle between the *n* direction of the local coordinate system and the *r* direction of the global coordinate system. Thus, the transformations of stresses, strains, stiffnesses, and compliances from the fiber coordinate system to the global coordinate system involve two coordinate rotations, the first one through the wrap angle *BETA* and the second through the polar angle *SETA*. Both transformations are rotations about a fixed axis, and therefore are identical in nature.

First consider a general coordinate transformation for a rotation about an axis. Figure 8 shows a rotation from an unprimed coordinate system (123) to a primed coordinate system (123'). The rotation is about the 3 axis and through an angle θ. The coordinate transformation of the stress tensor through a rotation is given by Frederick and Chang [21] in tensorial form as:

$$\sigma'_{ij} = a_{ik}a_{jl}\sigma_{kl} \tag{4.3.1.1}$$

where a_{ij} are the angle cosines. Written in matrix form, equation (4.3.1.1) becomes:

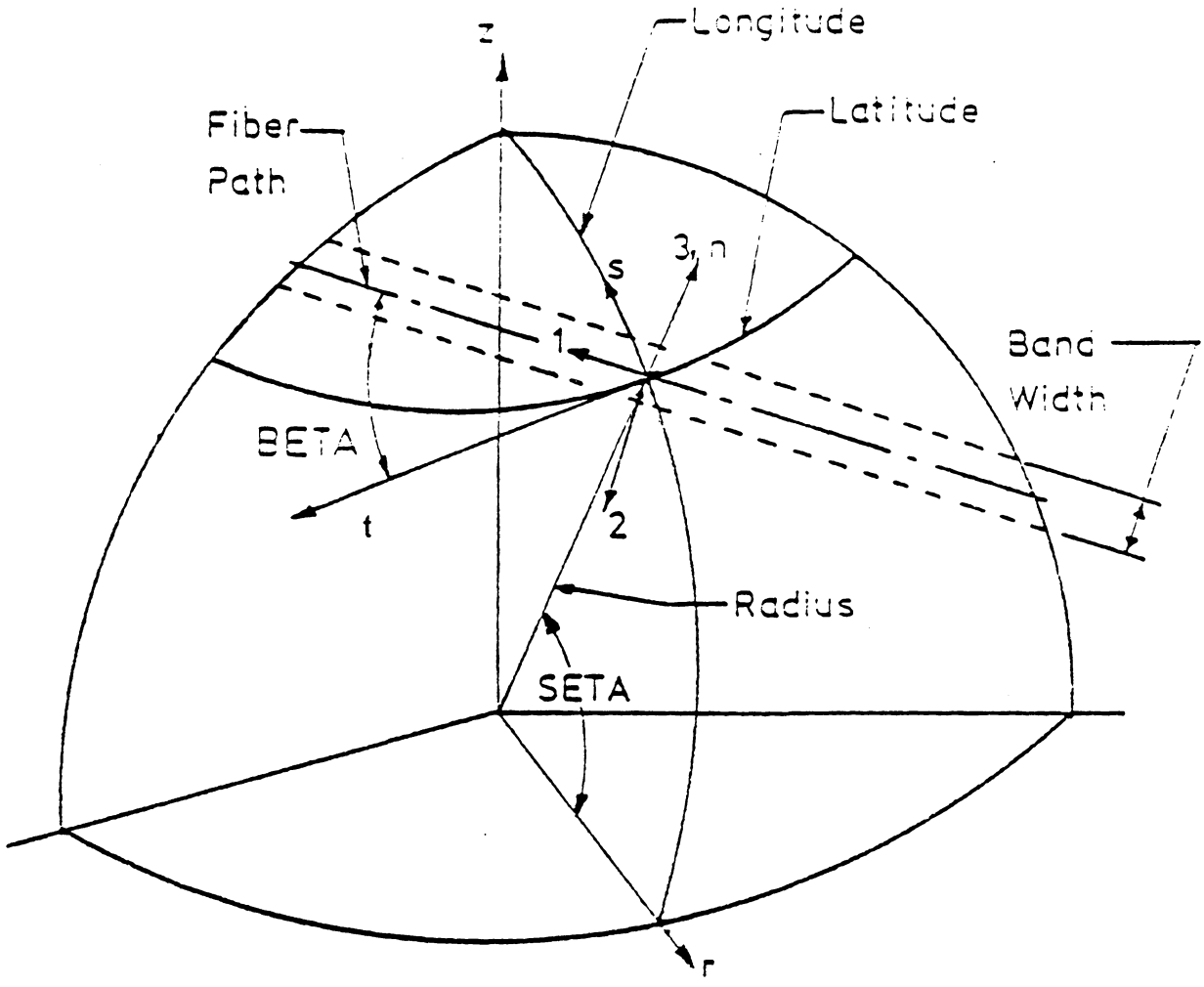

Figure 7. Schematic of Transformation Angles BETA and SETA

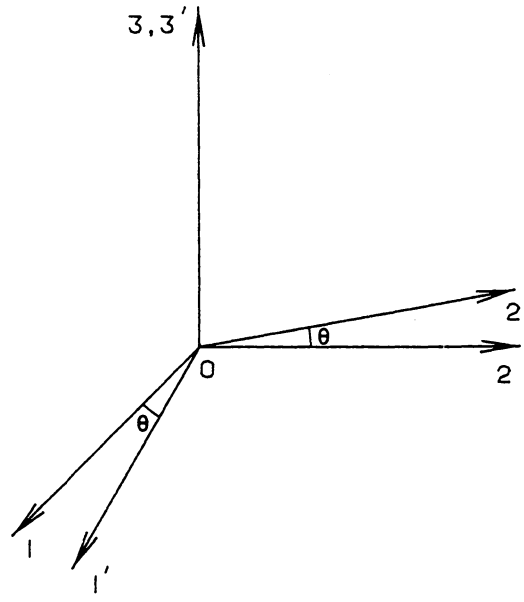

Figure 8. General Coordinate Rotation About One Axis

$$\begin{Bmatrix} \sigma_{11} \\ \sigma_{22} \\ \sigma_{33} \\ \sigma_{23} \\ \sigma_{13} \\ \sigma_{12} \end{Bmatrix} = \begin{bmatrix} M^2 & N^2 & 0 & 0 & 0 & 2MN \\ N^2 & M^2 & 0 & 0 & 0 & -2MN \\ 0 & 0 & 1 & 0 & 0 & 0 \\ 0 & 0 & 0 & M & -N & 0 \\ 0 & 0 & 0 & N & M & 0 \\ -MN & MN & 0 & 0 & 0 & M^2 - N^2 \end{bmatrix} \begin{Bmatrix} \sigma_{11} \\ \sigma_{22} \\ \sigma_{33} \\ \sigma_{23} \\ \sigma_{13} \\ \sigma_{12} \end{Bmatrix} \qquad (4.3.1.2)$$

or

$$\{\sigma\}' = [T]\{\sigma\} \qquad (4.3.1.3)$$

where $M = \cos\theta$,

$N = \sin\theta$, and

$[T]$ is the stress transformation matrix.

The same transformation matrix can be used for the strains provided the tensorial strains are used. Tensorial strains are different from engineering strains in that the shear terms in the tensorial strains are half of those in the engineering strains.

The transformation of the compliance matrix can be derived from the stress and strain transformations; however, it has already been worked out by Tsai [22]. The compliance transformation for the rotation in Fig. 8 is given in Fig. 9. Again, M and N denote the cosine and the sine of the rotation angle, respectively. The same transformation can be used for the material stiffness matrix provided the shear coupling terms are divided in half and the shear terms are divided by four before being put through the transformation. After the transformation, the shear terms must be multiplied by four and the shear coupling terms by two. These are required for use with engineering strains.

$$C_{11} = M^4C'_{11} + M^2N^2(2C'_{12} + C'_{66}) + N^4C'_{22}$$

$$C_{12} = M^2(N^2C'_{11} + C'_{22} - C'_{66}) + (M^4 + N^4)C'_{12}$$

$$C_{13} = M^2C'_{13} + N^2C'_{23}$$

$$C_{16} = MN[M^2(2C'_{11} - 2C'_{12} - C'_{66}) + N^2(2C'_{12} - 2C'_{22} + C'_{66})]$$

$$C_{22} = N^4C'_{11} + M^2N^2(2C'_{12} + C'_{66}) + M^4C'_{22}$$

$$C_{23} = N^2C'_{13} + M^2C'_{23}$$

$$C_{26} = MN[N^2(2C'_{11} - 2C'_{12} - C'_{66}) + M^2(2C'_{12} - 2C'_{22} + C'_{66})]$$

$$C_{33} = C'_{33}$$

$$C_{36} = 2MN(C'_{13} - C'_{23})$$

$$C_{44} = M^2C'_{44} + N^2C'_{55}$$

$$C_{45} = MN(C'_{55} - C'_{44})$$

$$C_{55} = N^2C'_{44} + M^2C'_{55}$$

$$C_{66} = 4M^2N^2(C'_{11} + C'_{22} - 2C'_{12}) + (M^2 - N^2)^2C'_{66}$$

Figure 9. Transformation of Terms of the Compliance Matrix

Now relate the general coordinate rotation of Fig. 8 to the coordinate transformations of the winding problem in Fig. 7. In the first rotation about the wrap angle *BETA*, the axis of rotation is the 3 axis of the fiber coordinate system and the angle of rotation is *BETA*. The fiber coordinate system 123 corresponds exactly with the unprimed coordinate system of the general rotation and the local coordinate sytem *stn* corresponds with the primed coordinate system. The second rotation through the polar angle *SETA* is about the *t* axis of the local coordinate system. If the local coordinate system is permuted from the order of *stn* to the order of *nst* then the second rotation becomes identical to the general rotation, with the *nst* coordinate system corresponding with the unprimed coordinate system and the global coordinate system *rzt* corresponding with the primed coordinate system. Thus, the same coordinate transformation can be used for both rotations.

The transformations discussed above are called the forward transformations. The inverse transformations (from the primed coordinate system to the unprimed coordinate system) can be thought of as forward transformations with a negative rotation angle. Thus, the inverse transformations can be easily obtained by substituting the negative rotation angles into the forward transformations.

4.3.2 Uncured Material Stiffness Matrix

Axisymmetric assumptions require that the average shear stresses τ_{rt} and τ_{zt} and the average shear strains γ_{rt} and γ_{zt} are zero for each element. Through transformation from *rzt* to *nst*, shear stresses τ_{nt} and τ_{st} and shear strains γ_{nt} and γ_{st} must also be zero for each element. These assumptions must be satisfied regardless of the cure state of the material.

When the material is uncured, there is no bonding between the layers and the layers are free to slide relative to each other. Therefore, there are no bond-induced internal stresses in the layers. Consequently, the stresses in each layer must be equal to the element stresses and thus equal to each other in the local coordinates:

$$\{\sigma\}^{+}_{stn} = \{\sigma\}^{-}_{stn} = \{\sigma\}^{e}_{stn} \tag{4.3.2.1}$$

where the superscripts + and - denote the plus and the minus layers, the superscript *e* denotes the element value, and the subscript *stn* denotes the coordinate system. This contrasts the assumption of the same state of strain in each layer for cured and bonded layers.

Without interlaminar bond stresses, the shear stresses τ_{st} and τ_{nt} are zero in the layers as they are zero for the element. The absence of these shear stresses in the layers is intuitively obvious since these stresses are induced by interlaminar shearing, which does not occur in the uncured material. Thus, the stress tensor in any layer of the uncured composite has the following form in the local coordinate system:

$$\{\sigma\}^{e}_{stn} = [\sigma_s \;\; \sigma_t \;\; \sigma_n \;\; 0 \;\; \tau_{ns} \;\; 0]^T \tag{4.3.2.2}$$

In this case, the mechanical shear strain components in the layers will have equal magnitude but opposite signs due to the orthotropic shear coupling of the composite material. Although the two layers have the same compliance matrix in the fiber coordinates, the layer compliance matrices are different in the local coordinates after transformations through opposite wrap angles. Since the mechanical strains are related to the stresses through the material compliance matrix, the layer mechanical strains in the local coordinate system are also different from each other:

$$\{\varepsilon\}^{+}_{m,stn} = [C]^{+}_{stn}\ \{\sigma\}^{e}_{stn}$$
$$\{\varepsilon\}^{-}_{m,stn} = [C]^{-}_{stn}\ \{\sigma\}^{e}_{stn} \qquad (4.3.2.3)$$

where the *m* subscript denotes the mechanical component of strains and the *stn* subscript denotes the local coordinate system.

The element strains are taken as the average of the layer strains and a constitutive equation can be written on the element level, relating the element strains to the element stresses:

$$\{\varepsilon\}^{e}_{m,stn} = \frac{\{\varepsilon\}^{+}_{m,stn} + \{\varepsilon\}^{-}_{m,stn}}{2} = \frac{[C]^{+}_{stn}\{\sigma\}^{e}_{stn} + [C]^{-}_{stn}\{\sigma\}^{e}_{stn}}{2}$$
$$= \frac{[C]^{+}_{stn} + [C]^{-}_{stn}}{2}\{\sigma\}^{e}_{stn} = [C]^{e}_{stn}\{\sigma\}^{e}_{stn} \qquad (4.3.2.4)$$

where $[C]^{e}_{stn}$ is the element compliance matrix in the local coordinate system. Thus, when the material is uncured, the element compliance matrix is simply the average of the layer compliance matrices. Since the layers have equal and opposite wrap angles, the shear coupling terms in the compliance matrices of the two layers are also equal and of opposite sign (by transformation). As a result, the shear coupling terms will go to zero in the averaging process.

After the element compliance matrix is computed in the local coordinate system, it is transformed to the global coordinate system and reduced to a 4 x 4 form by excluding the rows and columns corresponding to the *rt* and *zt* terms. The material stiffness matrix $[D]$ is then obtained by inverting the reduced compliance matrix.

The element stresses and strains in the global coordinate system computed from the displacement solution have to be converted back to the layer values in the fiber coordinates since these values are important in the strength determination. In the global and local coordinate systems, the layer stresses are the same as the element

stresses when the material is uncured. The layer strains, however, are different from the element strains, and therefore unknown. Therefore, transform the element stresses (which are also the layer stresses) back to the fiber coordinates and compute the fiber strains from the transformed stresses. Notice that while the stresses in the layers are equal in both the global and the local coordinate systems, they are different in the fiber coordinate system due to the transformation through the opposite wrap angles:

$$\{\sigma\}^{\pm}_{123} = [\sigma_1 \;\; \sigma_2 \;\; \sigma_3 \;\; \pm\tau_{23} \;\; \tau_{13} \;\; \pm\tau_{12}]^T \tag{4.3.2.5}$$

The difference comes only from the signs of the shear terms τ_{23} and τ_{12}. Thus, only the stress state of the plus layer needs to be stored. The stress state in the minus layer can be obtained by reversing the signs of the shear stresses τ_{23} and τ_{12}.

The mechanical strains in the fiber coordinates can then be computed from the constitutive equations:

$$\{\varepsilon\}^{\pm}_{m,123} = [C]_{123}\,\{\sigma\}^{\pm}_{123} \tag{4.3.2.6}$$

Since the compliance matrix has generally orthotropic form in the fiber coordinates, the layer strain tensors have the form:

$$\{\varepsilon\}^{\pm}_{m,123} = [\varepsilon_1 \;\; \varepsilon_2 \;\; \varepsilon_3 \;\; \pm\gamma_{23} \;\; \gamma_{13} \;\; \pm\gamma_{12}]^T \tag{4.3.2.7}$$

In the case of thermal loadings, the total strains are the sum of the mechanical strains and the free thermal strains. The free thermal strains in the fiber coordinates, being calculated from the coefficients of thermal expansion and the temperature change, are of the form:

$$\{\varepsilon\}^{\pm}_{th,123} = [\varepsilon_1 \;\; \varepsilon_2 \;\; \varepsilon_3 \;\; 0 \;\; 0 \;\; 0]^T \tag{4.3.2.8}$$

Thus, the form of the total strain tensor is identical to equation (4.3.2.7). Again, only the strain state in the plus layer needs to be stored.

4.3.3 Cured Material Stiffness Matrix

When the material is cured, the layers are rigidly bonded together, resulting in the same strain state in each layer in the local coordinate system:

$$\{\varepsilon\}^{+}_{stn} = \{\varepsilon\}^{-}_{stn} = \{\varepsilon\}^{e}_{stn} \tag{4.3.3.1}$$

The strains in equation (4.3.3.1) are the total strains in the layers. Since the material stiffness matrix relates the stresses to the mechanical strains, one can simplify the problem by considering the case of the mechanical loadings only. In such a case, the total strains are equal to the mechanical strains.

Equation (4.3.3.1) implies that the shear strains γ_{nt} and γ_{st} are zero for the layers as they are for the elements (from axisymmetric assumptions). Thus, the layer strain tensors in the local coordinates have the form:

$$\{\varepsilon\}^{\pm}_{stn} = [\varepsilon_s \;\; \varepsilon_t \;\; \varepsilon_n \;\; 0 \;\; \gamma_{ns} \;\; 0]^T \tag{4.3.3.2}$$

Physically, the absence of the shear strains γ_{nt} and γ_{st} can be justified by considering the opposite wrap angles of the two layers. The material orthotropy in one layer would generate shear strains in one direction and the material orthotropy in the other layer would generate equal shear strains in the other direction due to the equal and opposite wrap angles. Since the layers are rigidly bonded together, they restrict each other from shearing.

The stresses in the layers, however, are not equal due to internal stresses induced by bonding of the layers:

$$\{\sigma\}^{+}_{stn} = [D]^{+}_{stn}\{\varepsilon\}^{e}_{stn}$$
$$\{\sigma\}^{-}_{stn} = [D]^{-}_{stn}\{\varepsilon\}^{e}_{stn} \qquad (4.3.3.3)$$

The element stress therefore has to be taken as the average of the layer stresses. As a result, the constitutive equation is written on the element level as:

$$\{\sigma\}^{e}_{stn} = \frac{\{\sigma\}^{+}_{stn} + \{\sigma\}^{-}_{stn}}{2} = \frac{[D]^{+}_{stn}\{\varepsilon\}^{e}_{stn} + [D]^{-}_{stn}\{\varepsilon\}^{e}_{stn}}{2}$$
$$= \frac{[D]^{+}_{stn} + [D]^{-}_{stn}}{2}\{\varepsilon\}^{e}_{stn} = [D]^{e}_{stn}\{\varepsilon\}^{e}_{stn} \qquad (4.3.3.4)$$

where $[D]^{e}_{stn}$ is the element stiffness matrix. Thus, when the material is cured, the element material stiffness matrix is simply the average of the layer material stiffness matrices in the local coordinate system. The element stiffness matrix in the local coordinate system must then be transformed to the global coordinate system and reduced to a 4×4 form by excluding the rows and columns corresponding to the *rt* and *zt* terms. As in the case of the uncured material, the averaging process results in zero shear coupling terms in the element stiffness matrix.

The transformations of the computed stresses and strains from the global coordinate system back to the fiber coordinate system is done in the exact opposite fashion from the case of uncured material. When the material is cured, the layer strains are equal to the element strains, and therefore known completely. Meanwhile, the layer stresses are unknown. Therefore, transform the element strains (which are also the layer strains) back to the fiber coordinate system and use them to calculate the layer stresses.

Like the stress tensors in the case of uncured material, the layer strain tensors in the fiber coordinate system have the form:

$$\{\varepsilon\}^{\pm}_{123} = [\varepsilon_1 \;\; \varepsilon_2 \;\; \varepsilon_3 \;\; \pm\gamma_{23} \;\; \gamma_{13} \;\; \pm\gamma_{12}]^T \tag{4.3.3.5}$$

The layer stresses in the fiber coordinates are then computed from the constitutive equations:

$$\{\sigma\}^{\pm}_{123} = [D]_{123}\,\{\varepsilon\}^{\pm}_{123} \tag{4.3.3.6}$$

The specially orthotropic form of the stiffness matrix in the fiber coordinates and the form of the layer strain tensor $\{\varepsilon\}^{\pm}_{123}$ give rise to the following form of the layer stress tensors:

$$\{\sigma\}^{\pm}_{123} = [\sigma_1 \;\; \sigma_2 \;\; \sigma_3 \;\; \pm\tau_{23} \;\; \tau_{13} \;\; \pm\tau_{12}]^T \tag{4.3.3.7}$$

Thus, as in the case of uncured material, the stress and strain tensors need to be stored only for the plus layer.

In the case of thermal loadings, the strains obtained are the total strains which include the free thermal strains and the mechanical strains. Before the stresses can be calculated from equation (4.3.3.6), the mechanical strains must be obtained by subtracting the free thermal strains from the total strains. As shown previously, the addition or subtraction of the free thermal strains does not change the form of the strains tensor, and consequently the form of the stress tensor in the fiber coordinates.

Notice that while all discussions in this section assumed that each composite element contains only one plus layer and one negative layer, the material formulation is also valid for the case where each element contains several plus and minus layers with the only requirements being the number of the plus layers equal to the number

of minus layers and all layers in the element having the same absolute value of the winding angle.

Chapter 5

Fabrication Simulation

This chapter will describe in detail the simulation of the fabrication process, as outlined in Chapter 3. The next three sections will describe the simulation of the three fabrication stages, along with detailed discussions of the modeling of the physical phenomena in each stage. The last section of the chapter will discuss the stress redistribution equilibrium.

5.1 Winding Simulation

The winding simulation includes the modeling of the winding process, particularly the addition of layers and the conversion of the winding tensions in those layers into nodal loads on the current structure, and the simulation of the physical phenomena occurring in the winding stage. In the winding stage, the composite

material is assumed to be uncured, and the uncured material formulation in the previous chapter is used.

5.1.1 Modeling of the Winding Process

The winding process is modeled with an incremental finite element formulation. A finite element model of the structure is created with all the composite layers as they would exist in the complete structure. At the start of the winding process, all composite elements are turned off, leaving just the mandrel elements as active elements in the model. Elements are turned off by having their structural stiffness matrices excluded from the global stiffness matrix. As composite layers are being wound, the elements corresponding to those layers are turned on by including their structural stiffness matrices in the global stiffness matrix. Thus, at any stage of the winding process, only the mandrel elements and the composite elements belonging to the already wound layers are active.

The winding tensions in the layers are modeled by the following initial stress tensor in the fiber coordinate system:

$$\{\sigma\}^{\pm}_{123} = [\sigma_1 \ 0 \ 0 \ 0 \ 0 \ 0]^T \tag{5.1.1.1}$$

where σ_1 is equal to the winding tension. When transformed to the local coordinate system *nst*, the stress tensor acquires two other components through the transformation and becomes different for the plus layer and the minus layer:

$$\{\sigma\}^{\pm}_{stn} = [\sigma_s \ \sigma_t \ 0 \ 0 \ 0 \ \pm\tau_{st}]^T \tag{5.1.1.2}$$

The element initial stress tensor, or the initial stress tensor as seen by the structure, is the average of the stress tensors in equation (5.1.1.2):

$$\{\sigma\}^{e}_{stn} = \frac{\{\sigma\}^{+}_{stn} + \{\sigma\}^{-}_{stn}}{2} \tag{5.1.1.3}$$

Since the stress tensors in equation (5.1.1.2) are obtained by transformations of the stress tensor in equation (5.1.1.1) through opposite wrap angles, the shear terms τ_{st} in the plus and minus layers have equal magnitudes and opposite signs. All other terms are equal for the two layers. Thus, the averaged stress tensor has the following form:

$$\{\sigma\}^{e}_{stn} = [\sigma_s \;\; \sigma_t \;\; 0 \;\; 0 \;\; 0 \;\; 0]^T \tag{5.1.1.4}$$

Therefore, the calculation of the average initial stress tensor for the element is equivalent to transforming the winding tension to the global coordinate system and then discarding the shear term.

The initial stress tensor in the global coordinate system is regarded as a body force type loading and can be converted into nodal loads according to equation (4.2.12). A simplified version of that equation is given here for easy reference:

$$\{R\} = \int_{-1}^{1}\int_{-1}^{1} [B]^T \{\sigma\}^{e}_{rzt}\, rJ\,d\xi\,d\eta \tag{5.1.1.5}$$

where $\{R\}$ is the nodal load vector,

$[B]$ is the nodal displacements-strains matrix,

r is the radial coordinate,

J is the determinant of the Jacobian matrix, and

$\{\sigma\}^{e}_{rx}$ is the element initial stress tensor of equation (5.1.1.3) transformed to the global coordinates.

5.1.2 Instantaneous Tension Loss

The winding tension is a material dependent function of the spool tension. The functional relationship between these two quantities have to be established experimentally for each material. Winding experiments will have to be performed on mandrels of different sizes to establish the functional relationship between the winding tension and the spool tension. Once this functional relationship has been established, the winding tension can be plotted as a function of the spool tension for each material. Then, the winding tension can be picked from the graph once the spool tension is known.

5.1.3 Tension Loss Due to Multiple Circuit Winding

The fabrication stress model assumes that a whole layer is applied concurrently. Therefore, it is necessary to develop a multiple circuit winding model to approximate the tension loss due to this winding method without having to model the winding of each individual circuit.

The tension loss due to multiple circuit winding depends on the relative stiffnesses of the underlying structure and the composite layer being wound. These relative stiffnesses are in turn dependent on the engineering properties of the

mandrel and the composite, the thickness of the mandrel and the composite, and the size of the structure.

The simulation of the tension loss due to multiple circuit winding is based on the elasticity solution of the interference fit problem. Timoshenko and Goodier [23] showed that the stress levels in the rings of an interference fit problem are functions of the stiffnesses of the rings, as well as the size of the interference. One can directly control the stress levels in the rings by changing the interference or by changing the stiffnesses of the rings. Using the latter technique, stiffness of the layer being wound can be reduced such that the desired tension level is achieved in the layer.

A range of possible stiffnesses for the layer can be established by considering two extreme cases. The first case is when the stiffness of the layer being wound is zero. This is the case when one neglects the stiffness of the layer and assumes that the full winding tension in that layer is supported by the underlying structure alone. Such a case does not account for the tension loss due to multiple circuit winding at all. Consequently, the tension level in the layer after winding is equal to the winding tension. The second case occurs when the layer retains full stiffness. In this case, the winding problem becomes similar to the shrink fit problem. That is, the winding tension is assumed to be the initial stress in the layer before it is wound onto the mandrel and allowed to equilibrate. In this case, the tension loss in the layer after winding is significantly higher than the average loss in multiple circuit winding.

The actual winding process falls somewhere in between these two extreme cases. The tension level in the layer after winding is lower than the winding tension because of multiple circuit winding, as explained in Chapter 3. On the other hand, this tension level is higher than the tension level in the second case. In the second case, the tension loss in each circuit is caused by the displacement fields resulted from the winding tension of all circuits in the layer. However, in the actual case, the

tension loss in each circuit is caused only by subsequently wound circuits. Thus, the correct tension level in the layer right after winding can be theoretically achieved by picking a layer stiffness between zero (first case) and the full stiffness (second case). This can be accomplished by dividing the element material stiffness matrix by a reduction factor between 1 and infinity. A hypothesis was forwarded by the author that there is one such reduction factor which would yield reasonably accurate tension levels for all cases, regardless of the relative stiffnesses of the composite layer and the underlying structure.

A multiple circuit winding study was carried out to verify the hypothesis and to select the correct reduction factor. The case study selected is a simple case of hoop winding: a single layer consisting of 20 hoop circuits is wound onto a hollow cylinder. Despite the simplicity of the case study, the results are assumed to be valid for other, more complex cases.

Figure 10 shows a schematic of a cut section of the cylinder and the composite layer. Keeping the elastic modulus of the composite layer constant, there are four parameters that can be varied to achieve different relative stiffnesses of the mandrel and the composite layer: the Young's modulus of the mandrel E, the mandrel thickness TM , the composite layer thickness TC, and the mandrel inner radius R. The physical significance of these parameters is shown in the figure.

By selecting a reference case and varying these four parameters independently, five different cases were obtained. The parameters of the five cases are listed in Table 1. Case 1 was the reference case and the parameters in the other cases were varied with respect to this case. The winding tension in all cases was 100 units of stress. Note that since this is a parametric study, the actual units of the parameters are of no consequence. Also notice that in case 5, a low modulus of elasticity was used for the mandrel in addition to the reduction in the thickness of the com-

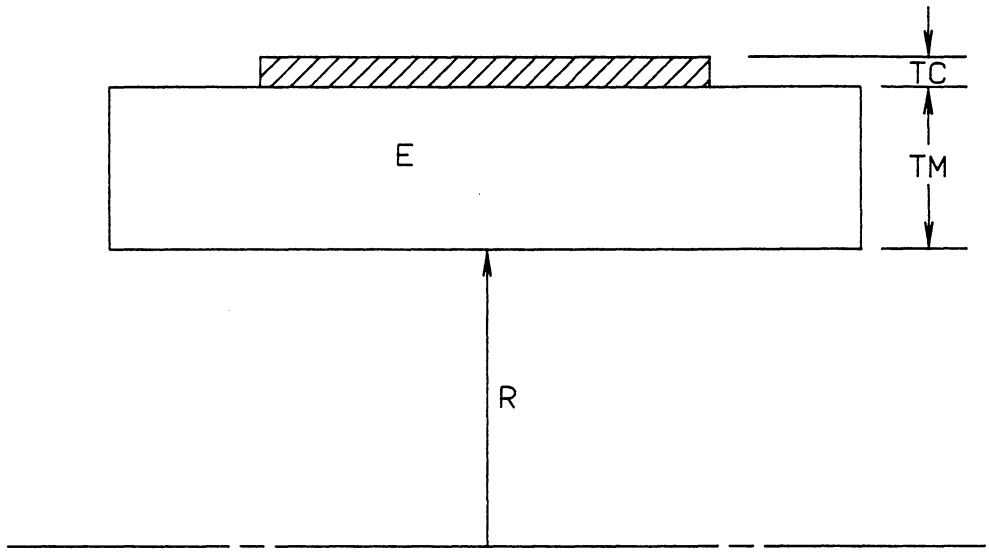

Figure 10. Multiple Circuit Winding Case Study

Table 1. Multiple Circuit Winding Case Studies

Parameter	Case 1	Case 2	Case 3	Case 4	Case 5
R	3.0	3.0	30.0	3.0	3.0
TC	0.02	0.02	0.02	0.02	0.002
TM	1.0	1.0	1.0	0.1	1.0
E	2.9E7	2.9E5	2.9E7	2.9E7	2.9E5

posite layer. This reduction of the elastic modulus was necessary since the small thickness of the composite layer would result in an extremely small tension loss had the full modulus been used.

The finite element model of the case study is shown in Fig. 11. Twenty composite elements were used, each representing a circuit. The mandrel was modeled with four elements through the thickness and was extended beyond the composite layer on both ends. To simulate circuit winding, one composite element was turned on at a time with the element being turned on given an initial stress equal to the winding tension and a very low stiffness (regular stiffness reduced by a factor of 10^6). The low stiffness of the element being turned on results in virtually all of the winding load being supported by the mandrel, thereby generating negligible stress increments in the composite element. As a result, the final stresses in the element would be approximately equal to the initial stresses (the winding tension).

The final tension levels in the circuits are plotted in Figs. 12 to 16. In these figures, the first circuit is at the left end and the last circuit is at the right end. Notice that all five cases display some end effects which are more pronounced in some cases than in others. At the starting end, the end effects are due to the extension of the mandrel beyond the composite layer. The end effects at the finishing end are due to the same extension of the mandrel plus the absence of further circuits which would have caused tension losses in the last few circuits. Barring these end effects, the average tension level of the circuits in the middle represents the average tension level in the whole layer after winding as would be in the actual multiple circuit winding process.

A slice was then taken out from the middle of the finite element model in Fig. 11 and used to compute the reduction factors which would yield a representative tension level for the actual case. This slice is shown in Fig. 17. The first four ele-

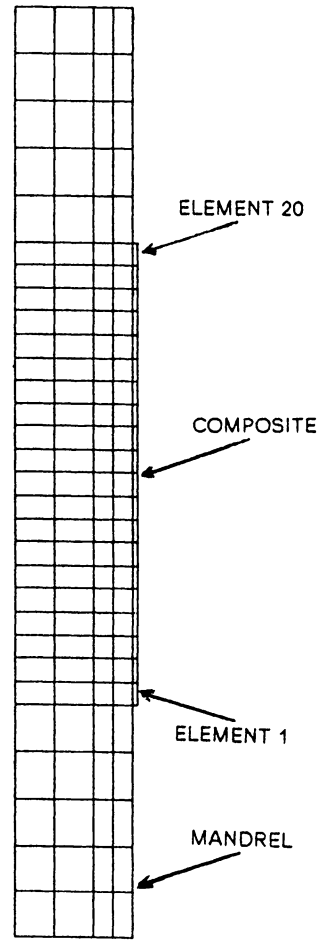

Figure 11. Finite Element Model of Multiple Circuit Winding Case Study

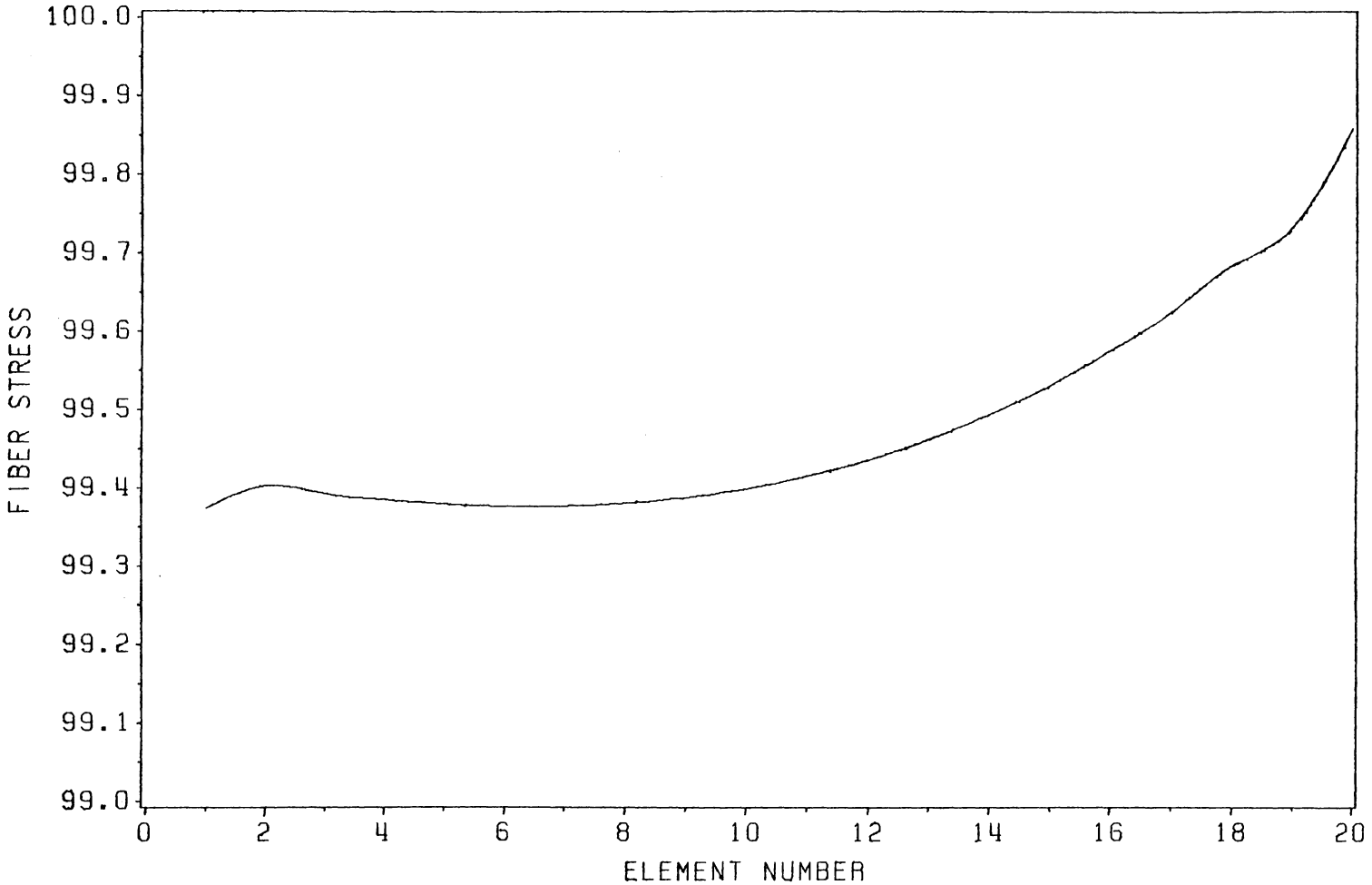

Figure 12. Circuit Tension Levels in Case 1

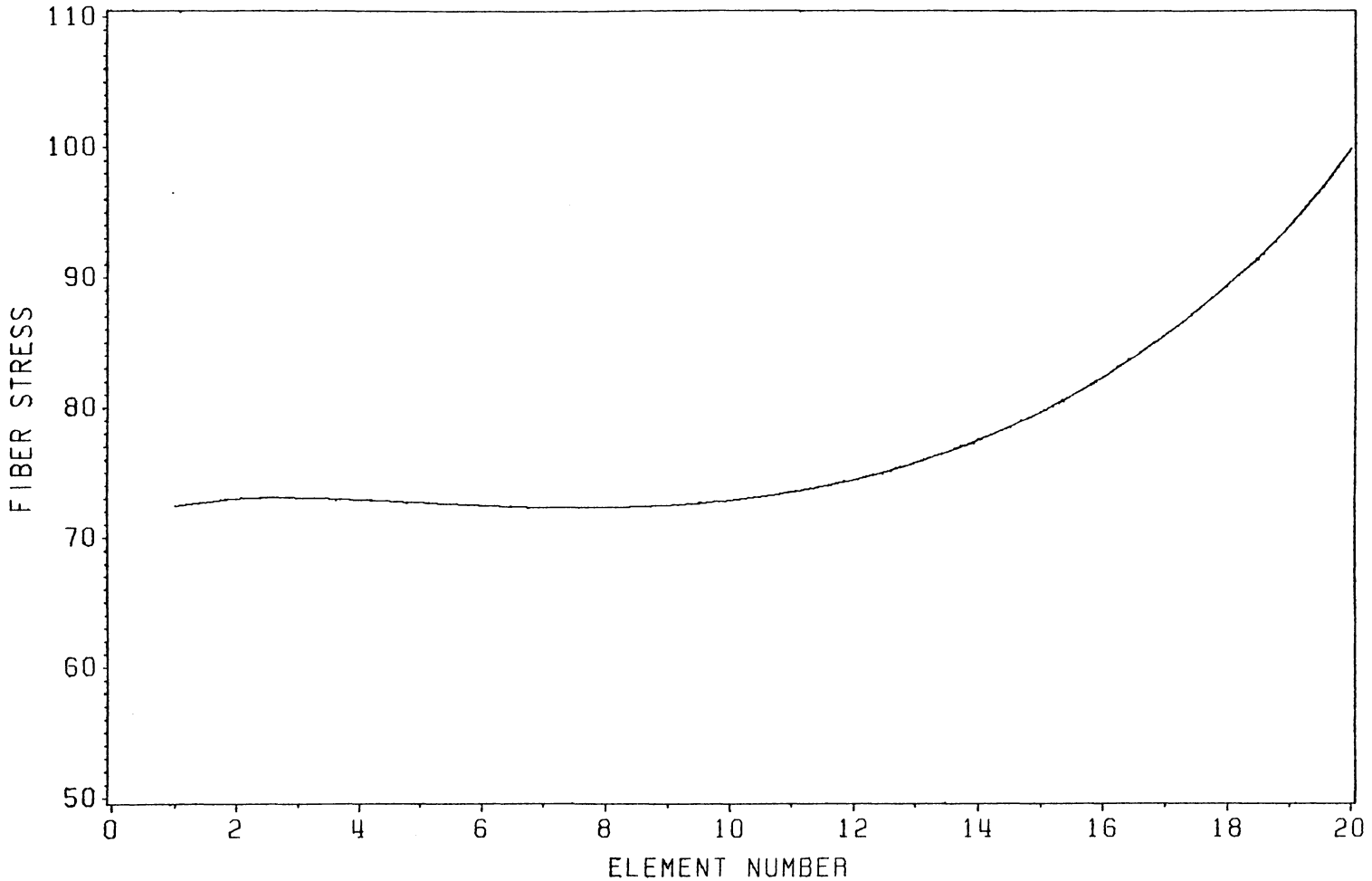

Figure 13. Circuit Tension Levels in Case 2

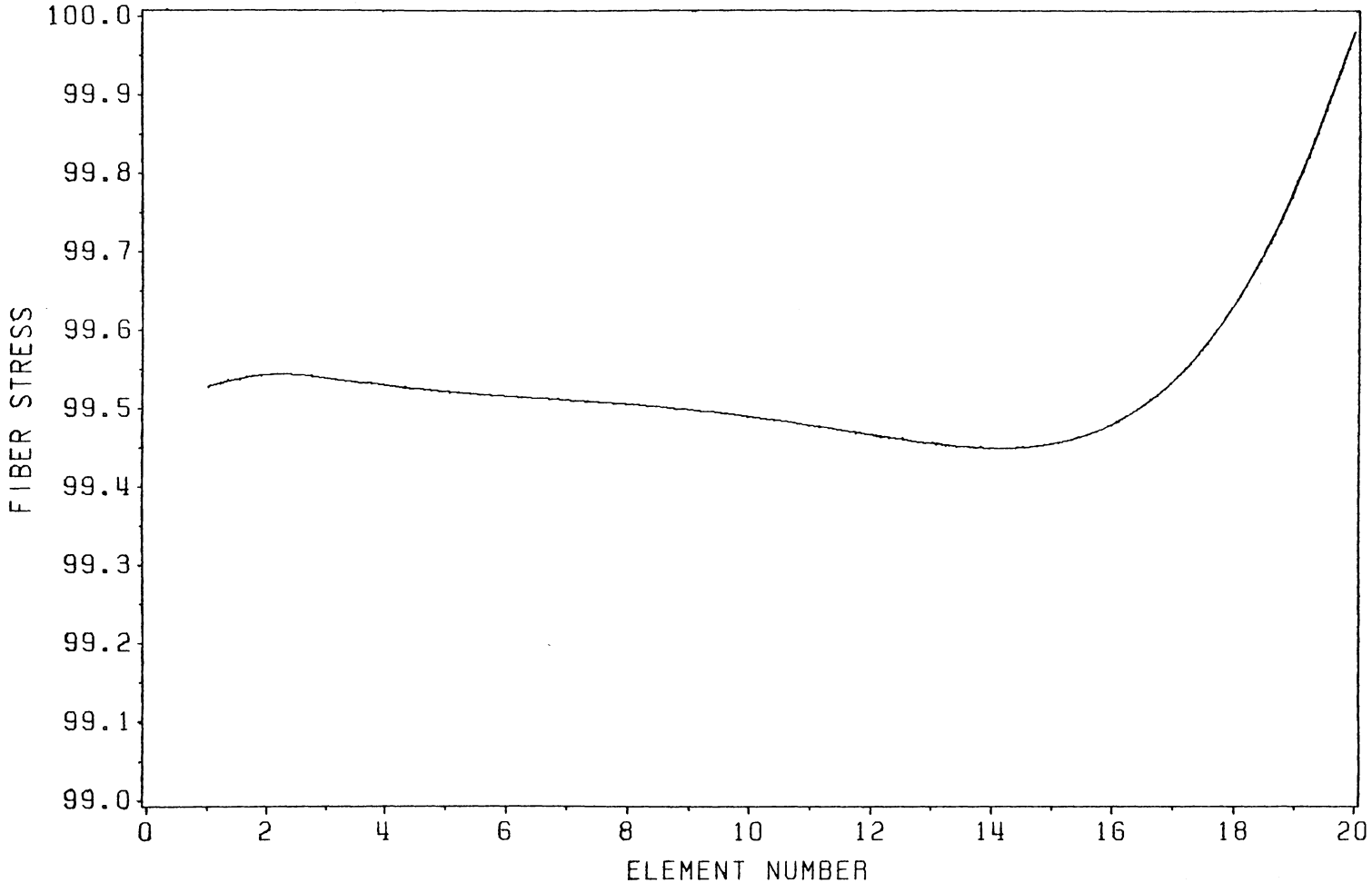

Figure 14. Circuit Tension Levels in Case 3

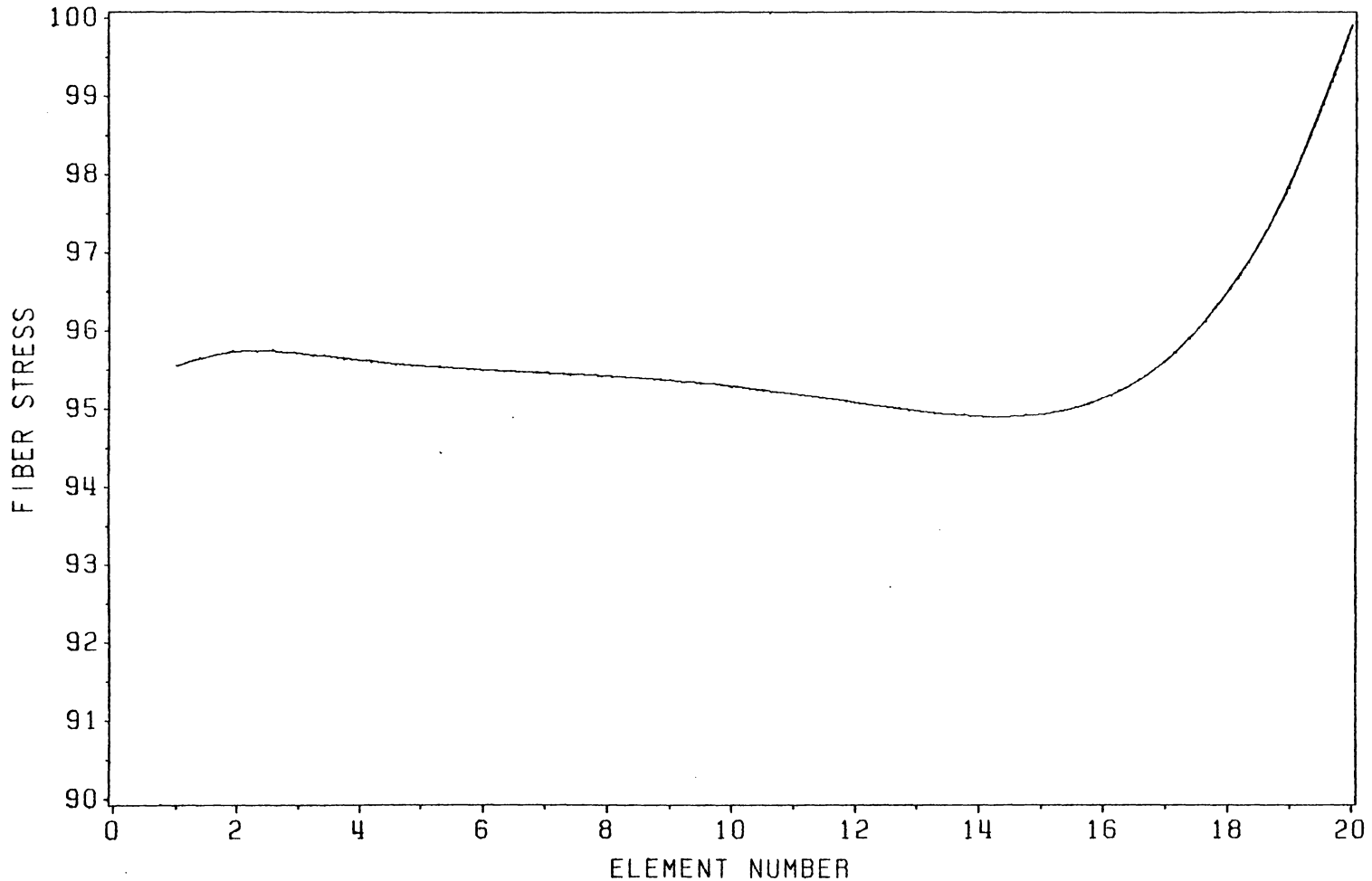

Figure 15. Circuit Tension Levels in Case 4

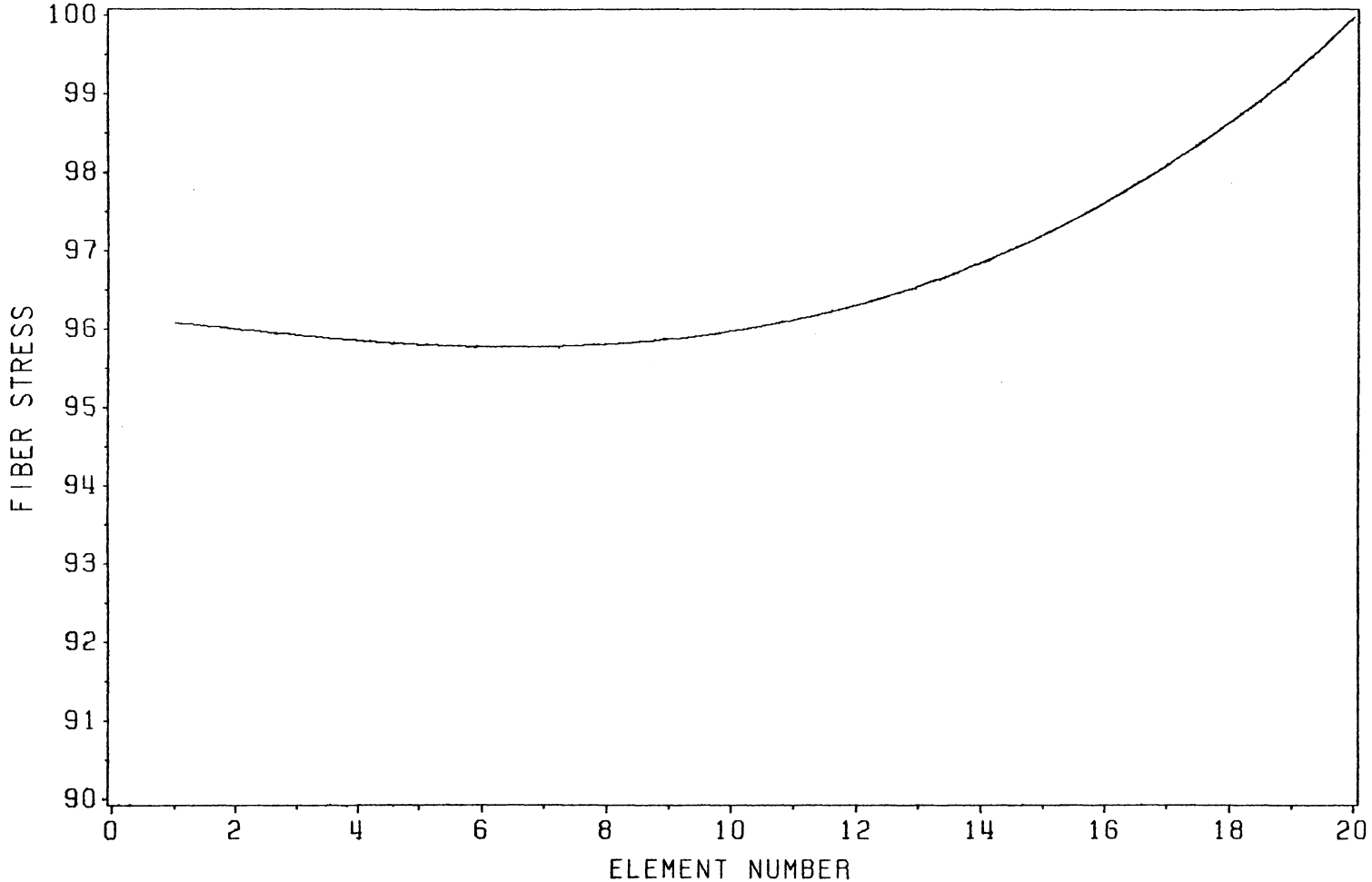

Figure 16. Circuit Tension Levels in Case 5

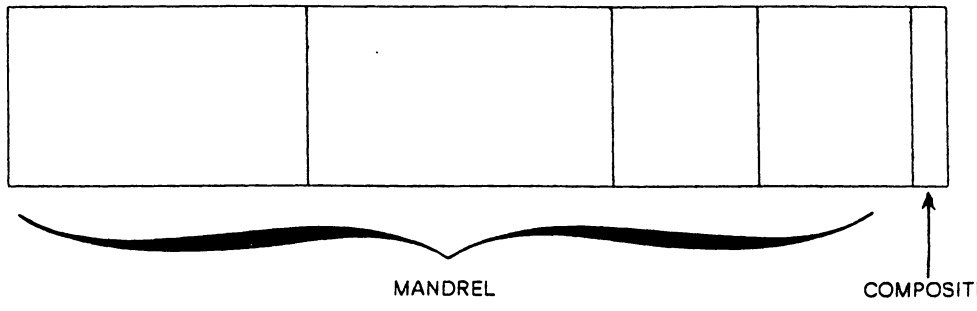

Figure 17. Finite Element Model for Reduced Stiffness Study

ments from the left are the mandrel elements. The last element is the composite element. The material stiffness of the composite element was divided by reduction factors ranging from 2.0 to 2.5 and the final tension level in the element was computed using the reduced stiffness. These tension levels are listed in Table 2 for all reduction factors, along with the actual tension levels (from the multiple circuit winding study) for all five cases. The tension losses computed from the reduced stiffnesses are also plotted in Fig. 18 as the percentage of the actual tension losses. From this figure, one can see that each reduction factor yields the best result for one or at most two cases. However, for all five cases, a reduction factor of 2.2 yields tension losses closest to the actual values, with a maximum difference of about 8%.

Notice that while the reduced stiffness method yields the correct tension level in the layer being wound, the computed strains are not correct, the reason being the layer's reduced stiffness is not the actual stiffness in the real case. Therefore, once the layer stresses are calculated (with the reduced stiffness), they must be used to calculate the correct layer strains using the full stiffness.

5.1.4 Tension Loss Due to Fiber Motion

The fiber motion model computes the radially inward motion of the fibers through the viscous resin in the uncured or only partially cured material. The inputs needed for the fiber motion model are the normal (3 direction) stress component in the element, the resin viscosity, the elastic modulus of the fibers, the fiber volume fraction, and the fiber radius.

The tension loss due to fiber motion is modeled in two steps. In the first step, the elasticity solution of the winding problem is obtained to yield the stress distrib-

Table 2. Tension Levels from the Multiple Circuit Winding Study

	Case 1	Case 2	Case 3	Case 4	Case 5
Actual	99.38	73.0	99.50	95.30	95.9
$a = 2.0$	99.39	69.04	99.42	94.51	95.70
$a = 2.1$	99.41	70.07	99.45	94.75	95.89
$a = 2.2$	99.43	71.04	99.47	94.97	96.07
$a = 2.3$	99.45	71.94	99.50	95.17	96.23
$a = 2.4$	99.47	72.97	99.51	95.35	96.38
$a = 2.5$	99.48	73.58	99.53	95.52	96.52

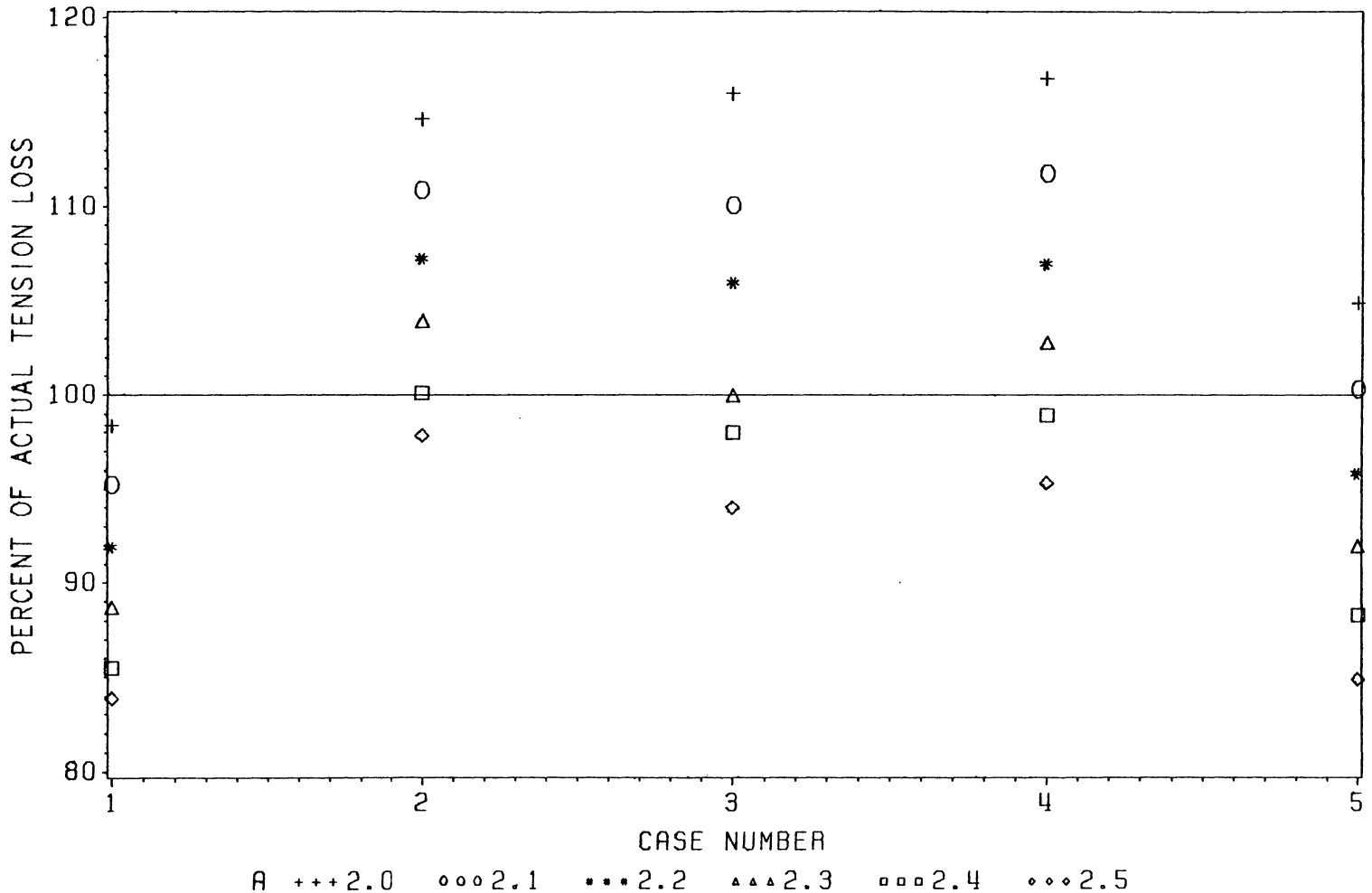

Figure 18. Comparison of Reduced Stiffness Method and Actual Winding

ution in the layers as if there is no fiber motion. In the second step, this stress distribution is used to calculate the amount of fiber motion for the whole duration of that step, with the assumption that the radial velocity of the fibers caused by the stress distribution in the layers is constant for the whole step. The associated tension loss is then used to modify the stress distribution in the layers.

The fiber motion model, which is based on the one dimensional model proposed by Loos et al. [16] is applied on an element by element basis. For each composite element, the fibers' radial velocity is computed from Darcy's law, which governs the motion of the fibers through a viscous resin:

$$\dot{W} = \frac{S}{\mu} \left(\frac{\Delta P}{t}\right) \qquad (5.1.4.1)$$

where $\dot{W}$ is the radial velocity,

μ is the viscosity in the element,

S is the permeability of the element, and

$\Delta P/t$ is the pressure gradient across the element.

The element viscosity and permeability are obtained from a thermo-kinetic model also developed by Loos et al. [16]. The pressure gradient is computed from the radial stress distribution (or the 3 direction stress distribution in the fiber coordinates).

The computation of the pressure across an element involves the radial stresses in three elements: the element under consideration and the radially adjacent elements on the inside and outside. First, the pressures on the radial boundaries of the element in consideration are calculated as weighted averages of the three element stresses with the element thicknesses being the weighting factors. Then, the pressure gradient across the element is computed as the difference of these boundary pressures divided by the thickness of the element. Two special cases have to be

considered: when a composite element is adjacent to a mandrel element and when a composite element lies in the outermost composite layer.

In the first case, when a composite element is adjacent to a mandrel element, the calculation of the pressure gradient must be modified. By analogy with the interference fit problem, the radial stress distribution has a local maximum at the interface. The interpolation of the lower stress values in the elements bordering this interface cannot yield the higher actual value at the interface. Because of this difficulty, instead of interpolating the boundary pressures, the pressure difference across the composite element is computed as twice the difference between the outer boundary value and the value at the element center (with the assumption of linear pressure distribution in the element).

In the second case, when a composite element lies in the outermost layer, the pressure on the outer boundary, which is a free surface, is obviously zero and taken to be as such.

Once the fibers' radial velocity is calculated, the total fiber motion in each step is calculated from the fibers' radial velocity and the time step size (time increment between wound layers):

$$W = \dot{W} \times \Delta t \qquad (5.1.4.2)$$

where W is the radial fiber motion, and

Δt is the time step size.

Associated with the fiber motion in the above equation is a loss of tension in the fibers due to the inward migration of the fibers. This tension loss can be calculated from the fiber motion and the fibers' stress-free radius of curvature in the normal direction, i.e., the direction of fiber motion:

$$\Delta T = E_f \frac{W}{R_o} \tag{5.1.4.3}$$

where ΔT is the tension loss,

E_f is the elastic modulus of the fibers,

W is the fiber motion, and

R_o is the fibers' stress-free radius of curvature in the normal direction.

The fibers' stress-free radius can be easily calculated from the fibers' radius of curvature in the current state of tension (also in the normal direction) and the elastic modulus of the fibers:

$$R_o = \frac{R}{\frac{T}{E} + 1} \tag{5.1.4.4}$$

where R is the fibers' radius of curvature under tension, and

T is the tension in the fibers.

The tension loss ΔT is modeled as a negative initial stress tensor:

$$\{\sigma\}_{tl} = [-\Delta T \;\; 0 \;\; 0 \;\; 0 \;\; 0 \;\; 0]^T \tag{5.1.4.5}$$

The initial stress tensor in the above equation is converted into a nodal load vector as in the simulation of the winding tension. Notice that while the previous two tension losses (instantaneous and multiple circuit winding) occur at the start of the winding step, the tension loss due to fiber motion is assumed to occur after the winding step has been completed. This assumption requires two stress computations for each step: the first is for the stresses due to the fabrication loads and the second is for the stress decrements due to the fiber motions.

Of the input parameters needed in the fiber motion model, three quantities are directly affected by the motion of the fibers: the fiber volume fraction, the element curvature, and the element thickness. The initial fiber volume fraction is a material dependent quantity that has to be specified for the particular composite material. The initial element curvature and thickness are computed from the finite element mesh geometry. These computations are described in Appendix A. The changes in these quantities are caused by the layer compaction resulting from the inward migration of the fibers.

The fiber motion W can be used to update the element thickness directly:

$$t_N = t_O - W \tag{5.1.4.6}$$

where t_N is the updated element thickness,

t_O is the old element thickness, and

W is the fiber motion.

The fiber volume fraction is updated using the new element thickness:

$$FR_N = FR_O\left(\frac{t_O}{t_N}\right) \tag{5.1.4.7}$$

where FR_N is the updated fiber volume fraction,

FR_O is the old fiber volume fraction,

t_N is the updated element thickness, and

t_O is the old element thickness.

The change in the element curvature should be insignificant due to the small magnitude of the fiber motion relative to the overall structure dimensions and therefore can be assumed negligible.

There are three conditions in which the tension loss is not computed: when the element is cured, when the element lies in an area of fiber-mandrel separation, and when the element experiences negative pressure gradient. In the first condition, it is obvious that there is no fiber motion in the cured material.

The second condition happens when certain special geometries induce a partial separation of the layer from the underlying structure. Since the finite element model cannot simulate this separation without a gap element, the radial stresses in the elements in the areas of separation will become positive whereas they should be zero in the actual case. Thus, a positive radial stress in the finite element solution indicates that the element lies in an area of separation. As a result, there is no fiber motion in that element.

The last condition happens when the pressure gradient in the element becomes negative, indicating a resin flow into the layer. In the actual case, once the resin flows out of a layer, very little can flow back. Therefore, it is safe to assume that no resin can flow back into the layers and skip the fiber motion calculation for elements with a negative pressure gradient.

5.2 *Mechanical Curing Simulation*

The mechanical curing simulation can be divided into two substages: the heatup stage where the curing occurs and the cooldown stage in which the material is completely cured. In the heatup stage, the material undergoes a gradual transition from an uncured state to a cured state. In the cooldown stage, the material is completely cured and there is no change in the mechanical behavior of the material.

Two physical phenomena that occur exclusively in the cure process are the material cure transition during the heatup step and the thermal expansion during heatup and contraction in cooldown. The modeling of these actions are described in this section. The fiber motion and stiffness degradation under compression which occur in the winding stage also occur during heatup.

5.2.1 Modeling of Material Transition

During cure, the composite material undergoes both a change in the engineering properties and a change in the mechanical behavior. These changes take place gradually as the material transitions from an uncured state to a cured state. The different mechanical behavior of the uncured material and the cured material has been discussed in the previous chapter. They can be now used to define the material behavior in a state of partial cure.

The cure state of a composite material is quantified by a parameter called the degree of cure, defined by Loos and Springer [24] as:

$$\alpha(t) = \frac{H(t)}{H_R} \tag{5.2.1.1}$$

where α is the degree of cure,

$H(t)$ is the heat of reaction up to time t, and

H_R is the total heat of reaction.

The degree of cure is a measure of how close the material is to being totally cured. When the material is uncured, the degree of cure is zero. When the material is cured,

the degree of cure is 1. When the material is partially cured, the degree of cure has a value between 0 and 1.

The material transition is modeled under the hypothesis that the degree of cure also measures the closeness of the partially cured behavior to the uncured behavior or cured behavior. In other words, the degree of cure can be used as the interpolation parameter in some interpolation scheme of the uncured and cured material stiffness matrices to arrive at the material stiffness matrix for the partially cured material. A linear interpolation is used in the fabrication stress model:

$$[D] = \alpha[D]_c + (1-\alpha)[D]_u \qquad (5.2.1.2)$$

where $[D]$ is the partially cured material stiffness,

$[D]_c$ is the cured material stiffness, and

$[D]_u$ is the uncured material stiffness.

In the above equation, one can see that when the degree of cure is 0, the partially cured stiffness becomes identical to the uncured stiffness. When the degree of cure is 1, the partially cured stiffness is identical to the cured stiffness. When the degree of cure falls in between 0 and 1, the stiffness falls in between the uncured and cured values.

5.2.2 Modeling of Thermal Expansion

The thermal expansion problem is modeled by converting the free thermal expansions of the elements into equivalent initial stresses which are then converted into nodal loads acting on the structure. The equivalent initial stresses are defined as the stresses necessary to hold the element to zero strains:

$$\{\sigma\}_{eq} = -[D]\{\varepsilon\}_{th} = -[D]\{\alpha\}\Delta T \qquad (5.2.2.1)$$

where $\{\sigma\}_{eq}$ is the equivalent element initial stress tensor,

$\{\varepsilon\}_{th}$ is the free thermal strain tensor,

$\{\alpha\}$ is the tensor of coefficients of thermal expansion, and

ΔT is the temperature change in the element for the thermal step.

As in the case of the material stiffness matrix, the calculation of the equivalent initial stresses is different for uncured and cured materials. The form of the equivalent element initial stress tensor in the global coordinate system depends on whether the plus and the minus layers are free to slide with respect to each other or rigidly bonded together.

In the uncured material, the free thermal strains of the two layers are different in the local coordinate system due to the opposite wrap angles:

$$\{\varepsilon\}^{\pm}_{th} = [\varepsilon_s \;\; \varepsilon_t \;\; \varepsilon_n \;\; 0 \;\; 0 \;\; \pm\gamma_{st}]^T \qquad (5.2.2.2)$$

As in the uncured material formulation, the element free thermal strains are taken as the average of the layer values:

$$\{\varepsilon\}^{e}_{th,stn} = \frac{\{\varepsilon\}^{+}_{th,stn} + \{\varepsilon\}^{-}_{th,stn}}{2} \qquad (5.2.2.3)$$

The element free thermal strains are the average strains in the element if it is allowed to expand freely. Thus, the stresses necessary to hold the element to zero strains are:

$$\{\sigma\}^{e}_{eq,stn} = -[D]^{e}_{stn}\{\varepsilon\}^{e}_{th,stn} \qquad (5.2.2.4)$$

The stress tensor in equation (5.2.2.4) will hold only the average strains in the element to zero. The shear strains γ_{st} in the layers cannot be forced to zero. Physically, this corresponds to the scissoring action of the layers.

In the cured material, the layers are never free to expand but always bonded together. Thus, the "free" thermal strains in the layers are different from those of the uncured case. Furthermore, they are equal to each other and equal to the element free thermal strains in the local coordinates. The element free thermal strains can be written as the sum of the layer free thermal strains as if there is no bonding and some mechanical strains:

$$\{\varepsilon\}^{e}_{th,stn} = \{\varepsilon\}^{\pm}_{th,stn} + \{\varepsilon\}^{\pm}_{m,stn} \tag{5.2.2.5}$$

where $\{\varepsilon\}^{\pm}_{m,stn}$ denotes the mechanical strains, which are induced by the bonding of the layers.

The bond-induced stresses in the layers can be written as the product of the layer stiffness matrices and the mechanical strains:

$$\{\sigma\}^{\pm}_{stn} = [D]^{\pm}_{stn}\{\varepsilon\}^{\pm}_{m,stn} = [D]^{\pm}_{stn}(\{\varepsilon\}^{e}_{th,stn} - \{\varepsilon\}^{\pm}_{m,stn}) \tag{5.2.2.6}$$

The sum of the bond-induced stresses over the two layers must be zero since there is no net loading on the element:

$$\begin{aligned} 0 &= \{\sigma\}^{+}_{stn} + \{\sigma\}^{-}_{stn} \\ &= \left([D]^{+}_{stn} + [D]^{-}_{stn}\right)\{\varepsilon\}^{e}_{th,stn} - \left([D]^{+}_{stn}\{\varepsilon\}^{+}_{th,stn} + [D]^{-}_{stn}\{\varepsilon\}^{-}_{th,stn}\right) \end{aligned} \tag{5.2.2.7}$$

Since the average of the layer stiffnesses is the element stiffness in the cured material formulation, equation (5.2.2.7) can rewritten as:

$$[D]^{e}_{stn}\{\varepsilon\}^{e}_{th,stn} = \frac{[D]^{+}_{stn}\{\varepsilon\}^{+}_{th,stn} + [D]^{-}_{stn}\{\varepsilon\}^{-}_{th,stn}}{2} \qquad (5.2.2.8)$$

Thus, the element free thermal strains are:

$$\{\varepsilon\}^{e}_{th,stn} = \left([D]^{e}_{stn}\right)^{-1}\left(\frac{[D]^{+}_{stn}\{\varepsilon\}^{+}_{th,stn} + [D]^{-}_{stn}\{\varepsilon\}^{-}_{th,stn}}{2}\right) \qquad (5.2.2.9)$$

The equivalent element initial stresses can now be computed from the element free thermal strains:

$$\{\sigma\}^{e}_{eq,stn} = -[D]^{e}_{stn}\{\varepsilon\}^{e}_{th,stn} = -\frac{[D]^{+}_{stn}\{\varepsilon\}^{+}_{th,stn} + [D]^{-}_{stn}\{\varepsilon\}^{-}_{th,stn}}{2} \qquad (5.2.2.10)$$

Thus, the equivalent element initial stresses are simply the average of the quantities $[D]^{\pm}\{\varepsilon\}^{\pm}_{th}$ in the local coordinate system.

Above are the calculations of the equivalent element initial stresses for the uncured and cured materials. For the partially cured material, the equivalent initial stresses are calculated by interpolating the uncured and the cured values in the same manner as the stiffness calculation:

$$\{\sigma\}_{eq} = \alpha\{\sigma\}_{eq,c} + (1-\alpha)\{\sigma\}_{eq,u} \qquad (5.2.2.11)$$

where $\{\sigma\}_{eq}$ is the equivalent initial stress tensor for the partially cured material,

$\{\sigma\}_{eq,c}$ is the equivalent initial stress tensor for the cured material, and

$\{\sigma\}_{eq,u}$ is the equivalent initial stress tensor for the uncured material.

Once the equivalent stresses have been determined, they can be converted into nodal loads according to equation (5.1.1.5).

One final note on the modeling of the curing process is that the heatup stage involves a change in the cure state of the material and large variations in the material viscosity. Therefore, this step must be modeled in many smaller steps to assure accuracy of the results. The cooldown step, however, involves no significant change in material properties and thus can be adequately modeled in just one step.

5.3 *Mandrel Removal Simulation*

The mandrel removal problem is treated by removing prestressed material. This problem involves both the removal of the mandrel stiffness and the removal of the interface pressure exerted by the mandrel on the composite. The removal of the mandrel stiffness is simulated by turning the mandrel elements off in the same manner as in the winding process: the mandrel elements' structural stiffness matrices are not included in the assembly of the global stiffness matrix. The removal of the interface pressure is simulated by exerting an equivalent and opposite pressure on the interface. This is accomplished by treating the stresses in the mandrel elements as initial stresses, and from them computing a set of nodal loads according to equation (5.1.1.5). These nodal loads represent the interface pressure exerted by the mandrel on the composite. To remove this interface pressure, apply on the interface nodes the same nodal loads but with a reversed direction. These reversed nodal loads are called excavation loads. The mandrel removal simulation can be done in a single step because of the linearly elastic nature of the cured structure.

5.4 Stress Redistribution Equilibrium

Unbalanced loads are generated during the winding stage when an element loses all tension. When this happens, the fiber stress becomes compressive in the finite element solution. In the actual case, however, the fibers cannot support compressive loads. Therefore, the compressive stress in the element must be unloaded and redistributed to the adjacent elements.

The stress redistribution is based on the fact that the difference between the external loads and the internal loads calculated from element stresses is the residual load that must be supported by the structure:

$$\{R\}_{ext} - \{t\}_{int} = \{R\}_{res} \qquad (5.4.1)$$

where $\{R\}_{ext}$ is the external load vector,

$\{t\}_{int}$ is the internal load vector calculated from element stresses, and

$\{R\}_{res}$ is the residual load vector.

The internal load vector is computed from the accumulated fiber stresses. First, the element stresses are computed by transforming the fiber stresses back to the global coordinate system and averaging. Then, the element stress tensor in the global coordinate system is converted into nodal loads using equation (5.1.1.5).

In the winding stage, the element with a compressive fiber strain is given a zero fiber stress component before the internal load vector computation, simulating the inability of the fibers to support compressive loads.

Chapter 6

Implementation

The fabrication stress model implementation resulted in a finite element program called WACSAFE (Winding And Curing Stress Analysis Finite Element program). WACSAFE utilizes the framework and solution algorithms illustrated in a finite element program called STAP by Bathe and Wilson [25]. This chapter will describe the general structure of the program, the input/output files, and two special features: the element OFFON number for the incremental construction simulation, and the stiffness matrix reduction scheme for execution efficiency. The descriptions of the program and the input/output files will be brief. For a more detailed description of input requirements and the complete program listing, the reader is referred to the WACSAFE User's Guide by Nguyen, Johnson, and Knight [26].

6.1 Program Structure

The WACSAFE flow chart, shown in Figs. 19 and 20, can be divided into three major parts: data input, displacement and stress computation, and fiber motion computation. Each part is described briefly below.

The data input part reads in problem control data, model geometry data, external loading data, and material properties data from a model input file. While reading model geometry data, WACSAFE is capable of linear generation of nodes between two specified nodes or elements between two specified elements if a generation flag is set. The generated nodes are always equally spaced. WACSAFE requires the input of all nonzero external loads in the form of nodal loads. The program then generates an external nodal load vector for each load step. For those load steps which do not involve external loadings, a zero external load vector is generated. The data input is executed once at the beginning of program execution. The input data are then stored on temporary files to be read for the execution of each load step.

Once the data input is completed, WACSAFE loops through all load steps for the displacement and stress computation and the fiber motion computation. Load steps correspond to the winding step, the heatup steps, the cooldown steps, and the mandrel removal step. The nodal displacements and the fiber stresses due to fabrication loadings are computed on the composite material as an elastic system. In other words, this step solves for the elasticity solution in each step of the fabrication process without inclusion of the fiber motion through the viscous resin. The stress increments are then calculated. The displacement and stress computation can be further divided into three substeps: stiffness matrix assembly, displacement solution, and stress computation.

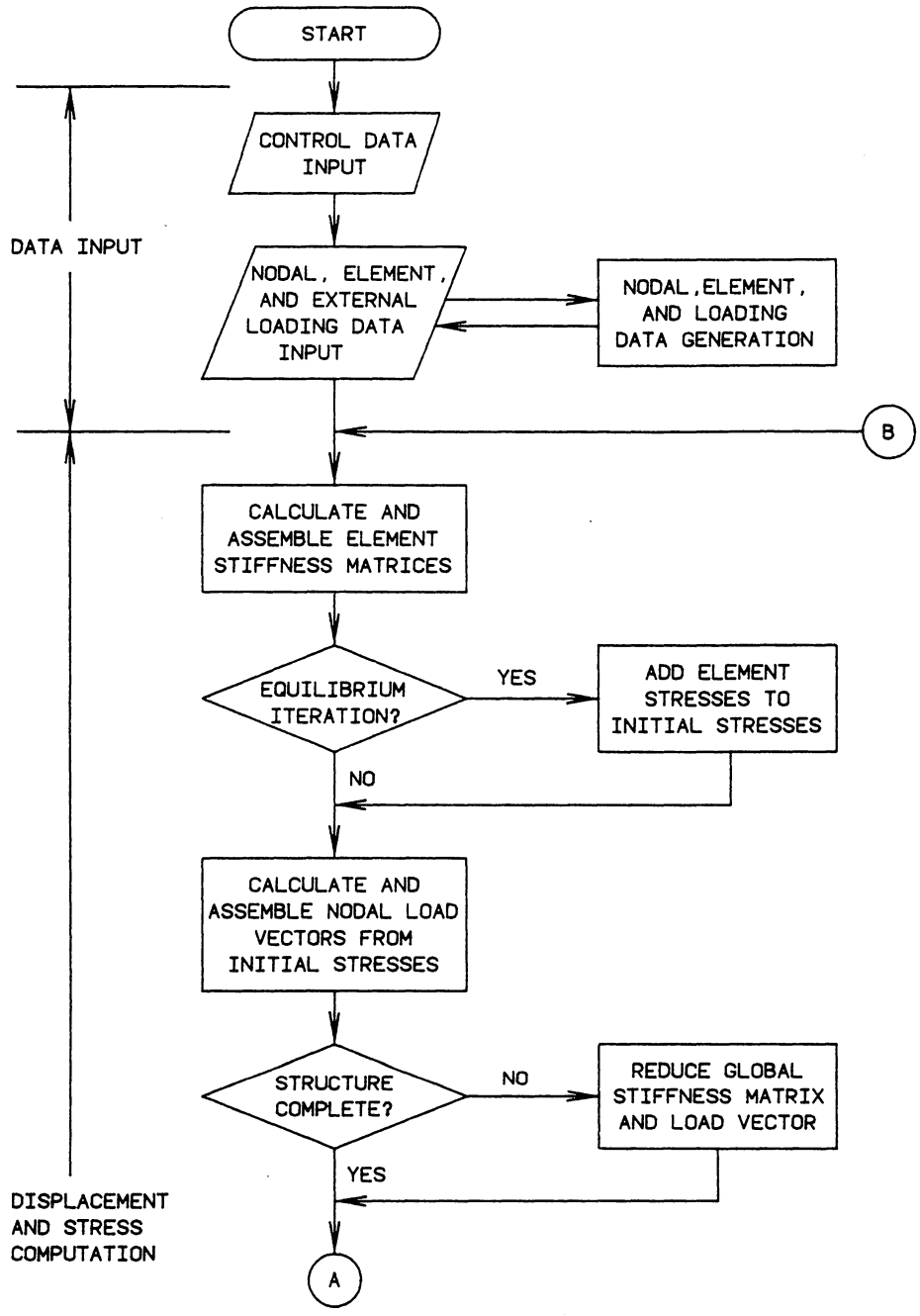

Figure 19. WACSAFE Flow Chart

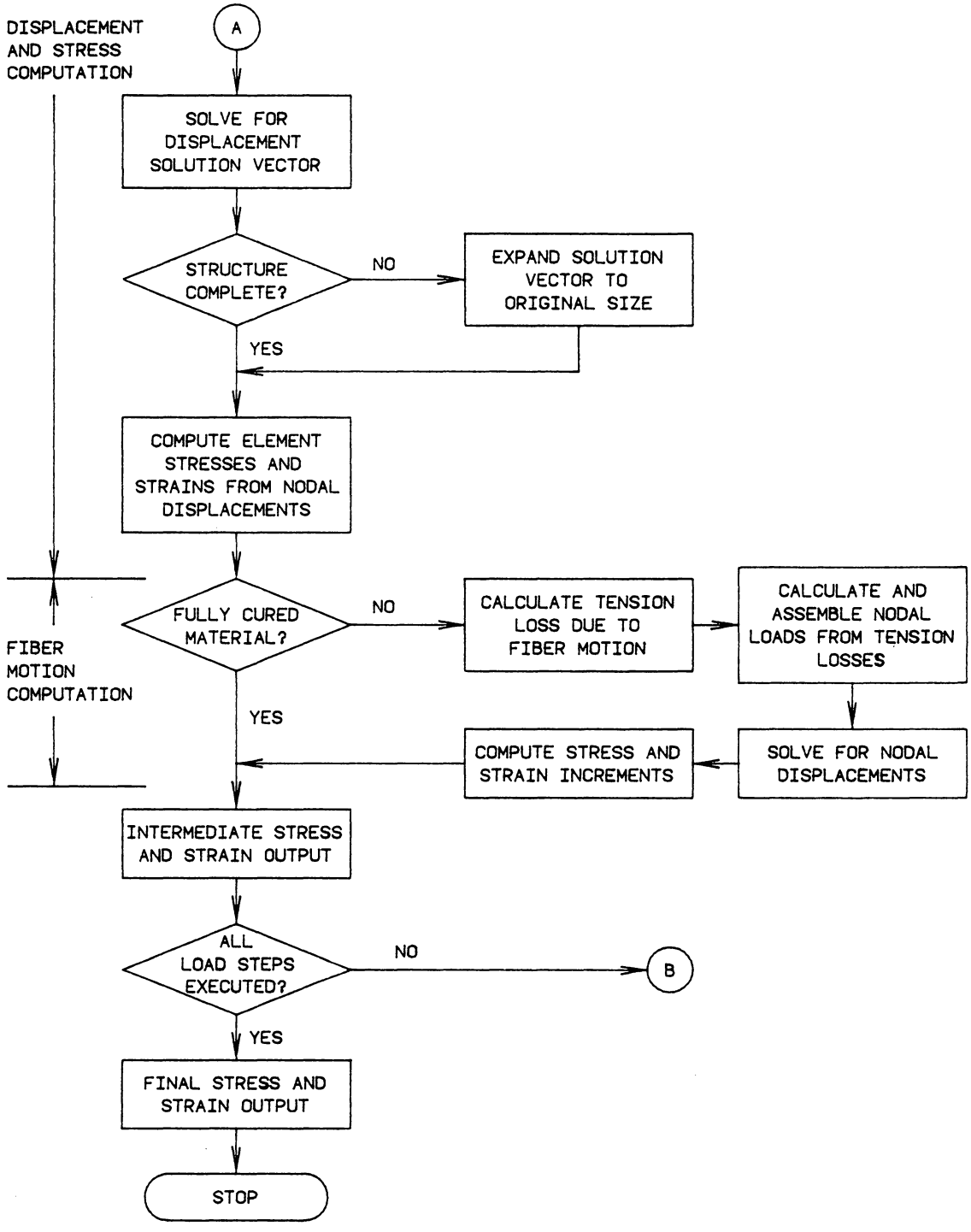

Figure 20. WACSAFE Flow Chart (Continued)

During the stiffness matrix assembly substep, uncured or partially cured elements with compressive fiber strains have their fiber direction stiffness reduced to the transverse direction. Consequently, the element material stiffness matrix becomes transversely isotropic. The in-plane shear modulus is then calculated from the in-plane elastic modulus and Poisson's ratio according to isotropic relations.

The element stiffness matrix is also reduced when the element is being turned on. In this case, all terms in the material stiffness matrix are uniformly reduced by the reducing factor ($a = 2.2$). See section 5.1.3 for the explanation of the reduction factor.

The stiffness matrix assembly process computes both the global stiffness matrix and the nodal load vector due to fabrication loads such as winding tension, thermal loading, or excavation loading. Winding tension data are read from temporary files along with the geometry data. Thermal loading data are read from a thermal input file. This nodal load vector is then added to the nodal load vector from external loading.

In the nodal load vector calculation, the user has the option to activate the one-step equilibrium iteration discussed in section 5.4. The activation of the equilibrium iteration is done by assigning a value to an equilibrium iteration flag in the control data. A value of 0 deactivates the equilibrium iteration completely. A value of 1 activates the equilibrium iteration only in the final fabrication step, whether this step is a winding step, a curing step, or a mandrel removal step. A value of 2 activates the equilibrium iteration only in the final load step of each fabrication stage. Finally, a value of 3 activates the equilibrium iteration in all load steps.

When the equilibrium iteration is activated, the element stresses are computed from the fiber stresses, converted to nodal loads, and added to the total nodal load vector. In the winding stage, elements with compressive fiber strains are assigned

a zero fiber stress before the element stresses are computed. The sum of all three nodal load vectors is the total nodal load vector acting on the structure.

The displacement solution substep involves a stiffness matrix reduction scheme in the winding simulation stage when the structure is incomplete to save computation time. The reduction scheme involves removing all inactive degrees of freedom associated with nodes in layers of the model where the elements have not been turned on yet. This reduction scheme will be described in the last section of this chapter. The reduced matrix equation is then solved for the displacement solution vector. The solution vector is expanded back to the original size before it is used for the stress and strain calculations. When the structure is completely wound, the reduction and expansion steps are skipped.

The stress computation substep uses the full model displacement solution vector to compute average element strain increments due to fabrication loading in the load step. These element strains are then used to compute the incremental fiber stresses and strains in the fiber coordinates, which are added to the cumulative stresses and strains from previous steps.

Aside from the fiber direction stresses and total strains, fiber direction component of the mechanical strain and the element stresses are also computed and stored in the load step. The first quantity is needed in the determination of possible stiffness degradation due to local fiber buckling and it is computed by subtracting the layer free thermal strains from the layer total strains. The element stresses are needed for the equilibrium iterations and are computed directly from the average element strains, the element free thermal strains, and the element material stiffness matrix.

The fiber motion computation is performed only when the material is not fully cured. The element degree of cure is compared with the value at the gel point of the material, at which the resin is sufficiently solid that there is no more fiber motion.

Thus, when the degree of cure equals or exceeds the value at the gel point, the fiber motion calculation is skipped. The gel point is a material dependent quantity and has to be obtained experimentally.

The radial fiber motion and the associated tension loss are computed from the fiber motion model. The tension loss is then converted into a nodal load vector. These computations are performed after the calculation of fiber stresses from fabrication loading. The nodal load vector due to fiber motion and the structural stiffness matrix, which has already been Gauss reduced in the displacement calculation, are used to solve for nodal displacements due to fiber motion.

The calculation of incremental stresses and strains from the nodal displacements due to fiber motion is accomplished in an identical manner to the previous stress and strain calculation.

At the end of the stress and fiber motion computations, the degree of cure is checked to see whether an element has just become cured. If this happens, that is if the element degree of cure has just become equal to or greater than the gel value, the fiber direction component of the cumulative layer mechanical strain is stored in an array which contains the fiber direction component of the layer mechanical strain at cure. The element strains are necessary for the determination of possible strength degradation in the final structure. Cumulative stresses and strains, and the strain-at-cure array are then printed out to the output file.

A dynamic storage scheme is utilized to allow easy storage allotment for problems of different sizes. In this storage scheme, all arrays are stored in one single column vector, with the start of each array marked by a pointer. The memory allocation for each problem is controlled by the size of the column vector only. WACSAFE also offers a data check option which calculates the total amount of stor-

age needed for a particular problem to let the user know how much memory to allocate for that problem.

6.2 Input/Output Files

Input data for WACSAFE is read from two input files: a model geometry file (Fortran Logical Unit Number 15) and a thermal data file (Fortran Logical Unit Number 19). These files, which completely define the problem, are described below.

The model geometry file contains control data, nodal data, loading data, material data, and element data, in that order. Control data control the program execution and output. Control data include the number of nodes and elements in the finite element model, the number of material groups, the number of steps in each fabrication stage, the step at which curing is complete, the equilibrium iteration flag, the execution mode flag, and output control flags. The equilibrium flag activates the stress redistribution equilibrium iteration, as explained in the previous section. The execution mode flag allows the choice of execution mode or data check mode. Finally, output control flags allow the suppression of output quantities such as the nodal load vector, the displacement solution, and the element strains.

Nodal data include the nodal coordinates and the boundary conditions on the nodes. The boundary conditions are specified by setting a boundary constraint flag to 1 (fixed) or 0 (free) for each degree of freedom on a node.

Loading data include external loads on the structure, either as additional pressure during fabrication or as external loading on the final structure. Loading data

needs to be specified only when there are external loads on the structure. Loading data are specified in nodal form.

Material data include the mechanical properties of the material groups such as the elastic moduli, the Poisson's ratios, and the coefficients of thermal expansion. Since the composite material usually undergoes changes in the mechanical properties when cure occurs, two input lines are required for each material group: one to represent the uncured material condition and one for the cured material. For consistency, two input lines are also required for materials which do not undergo curing (such as the mandrel), in which case the two input lines are identical. Other data necessary for the fiber motion model such as the winding time for winding steps, the initial material viscosity, the radius of the fiber, the fiber modulus of elasticity, and the initial fiber volume fraction are also included in the material data.

Element data include the connectivity data (which defines the element), the OFFON data (explained in next section), the material set assigned to the element, the wrap angle *BETA*, the polar angle *SETA*, and the winding tension. The elements have to be numbered sequentially in the radial direction for the computation of the pressure gradients needed in the fiber motion model. This requirement comes from the fact that the pressure gradient computation uses three radially adjacent elements, and the simplest way to determine which elements are radially adjacent is to number all elements sequentially in the radial direction.

The thermal data file contains information necessary for the curing stage of fabrication. This data file includes the reference temperature, i.e., room temperature at which the part is wound, and for each thermal step, the time step size, the element temperatures, the element degrees of cure, and the element viscosities. The thermal data file is supplied by the thermo-kinetic cure model by Loos [16]. When only winding is being modeled, the thermal data file is not needed by WACSAFE.

The analysis results are written to a main output file, and several auxiliary output files if there are intermediate outputs. The main output file (Fortran Logical Unit Number 16) contains a printout of the problem data and the final fiber stresses and (total) strains in the fiber coordinates, listed by the element number. The fiber stresses are always printed but the strain output is optional. The user can choose to have the strain output by setting an output flag to 1. In addition to the final stresses and strains, the main output file also contains a printout of the fiber direction component of the mechanical strains at cure. The user can also choose to print intermediate results by setting another output flag to the number of intermediate outputs desired and by specifying the step number of those intermediate outputs. The stresses and strains of each intermediate output are printed in a separate auxiliary output file with the Fortran logical unit number starting from 21 and incrementing with each output. The format of the stress output in the auxiliary output files are identical to the format of the stress output in the main output file.

6.3 *Element OFFON Number*

The incremental construction problem is simulated by assigning to each element an OFFON number. The OFFON number denotes the step number in which the element is turned on. Once an element is turned on, it stays on unless it is part of a mandrel to be removed. In that case, the element stays on until the removal step in which it is removed. Elements which have OFFON numbers greater than the current load step number are not included in the structure stiffness matrix assembly. An element with an OFFON number less than the load step number is already on prior to

that load step and thus has the full stiffness. An element with an OFFON number equal to the load step number is just turned on for that load step, and thus will have a reduced stiffness to account for multiple circuit winding, as described in the previous chapter.

The mandrel removal stage is simulated in a similar manner. Here, the mandrel element to be removed is assigned a negative OFFON number with the magnitude equal to the step number in which it is to be removed. When a mandrel element is part of the final structure, it must be assigned an OFFON number of 0 or a negative number with a magnitude greater than the total number of load steps.

6.4 *Stiffness Matrix Reduction*

The complete final model is created at the beginning of the analysis with layers of elements having OFFON numbers to prompt their inclusion. During the winding simulation when the structure is not completely wound, the structure stiffness matrix is reduced in size by removing the rows and columns associated with inactive degrees of freedom on nodes due to the absence of yet to be wound layers. The removal of these rows and columns reduces the size of the matrix equation, and consequently minimizes the number of arithmetic operations in the solution stage. The stiffness matrix reduction scheme is explained below, after a description of the format of the full form stiffness matrix and the associated arrays.

The stiffness matrix is associated with two arrays: ID and MAXA. These arrays are needed in both the assembly process and the solution process. The ID array contains the equation numbers of the active degrees of freedom in the fully wound

structure. It has a length equal to the number of nodes in the finite element model and a width equal to the number of degrees of freedom at each node (2 in the case of axisymmetric formulation). Each row of the ID array corresponds to a node and each column corresponds to a degree of freedom at that node: the first column corresponds to the *r* degree of freedom and the second column corresponds to the *z* degree of freedom. Thus, the ID array contains all the degrees of freedom in a finite element model, both active and inactive. The ID array is generated in the following manner. For every degree of freedom fixed by boundary conditions (inactive), a 0 is assigned to the corresponding location in the ID array. The remaining degrees of freedom are active and the corresponding locations are numbered sequentially. These numbers are the equation numbers of the active degrees of freedom. The ID array is used in the assembly process to take the inactive degrees of freedom out of the stiffness matrix. It is also used in the stress computation routine to match the displacement solution vector with active degrees of freedom only.

Array MAXA is required because the structure stiffness matrix is stored in the skyline format. In this format, the entries within the skyline above and including the diagonal are stored in a column vector. Array MAXA contains the addresses of the diagonal entries in the column vector. These addresses are needed to figuratively reconstruct the stiffness matrix in matrix form.

The matrix reduction scheme starts with the assembly of the stiffness matrix. In the load step when the structure is incomplete, the element stiffness matrices of dormant elements are excluded from the assembly process, resulting in zero diagonal entries corresponding to the inactive degrees of freedom. An ID2 array is then generated from the ID array by making the active degrees in ID inactive in ID2 whenever the corresponding diagonal entry in the stiffness matrix is 0. Thus, the

degrees of freedom which are active in ID but inactive in ID2 are those to be removed from the stiffness matrix.

The reduction of the stiffness matrix is accomplished through an auxiliary integer column vector IA associated with the stiffness matrix. Each entry in IA corresponds to an entry in the stiffness matrix. Initially, the column vector IA contains all 0's. Then, the entries in the rows and columns corresponding to the degrees of freedom to be removed are given a value of 1. The final step of the matrix reduction scheme involves removing all entries in the stiffness matrix with a corresponding entry of 1 in the IA column vector. As an entry is removed, the remaining entries are moved up to fill the gap. The final reduced stiffness matrix is stored in the same location as the initial stiffness matrix.

As the entries are removed from the stiffness matrix, the addresses of the diagonal entries of the remaining columns also change. The updated addresses are stored in array MAXA2. Arrays MAXA2 and ID2 are used with the reduced stiffness matrix in the solution routine.

In addition to the stiffness matrix, the nodal load vector is also reduced by removing the entries associated with the inactive degrees of freedom. The reduction of the nodal load vector is simply done by comparing ID2 with ID. After the reduction of both the stiffness matrix and the nodal load vector, the reduced size matrix equation can be solved for the displacement solution vector. Since the matrix equation was reduced, the solution vector is also in reduced form. Before being used for the stress computation, the displacement solution vector is expanded back to the full form. The expansion process is simply the reverse of the reduction process.

Chapter 7

Case Studies

Two case studies were selected to illustrate the use of WACSAFE: the joint overwrap of the space shuttle booster and a filament wound bottle. The first case carries the analysis through the winding and curing stages. It was selected because the availability of some experimental strain data (supplied by Morton Thiokol, Inc.) enables an evaluation of the accuracy of the fabrication stress model.

The second case carries the analysis through the mandrel removal stage. It was selected because its dome geometry and its slightly more complex winding pattern typify the general winding problem.

This chapter will describe each case study briefly before presenting the finite element model and the results from the analysis of each case. The fabrication stresses and strains are also used to predict the possibility of strength degradation in each case.

7.1 *Space Shuttle Booster Joint Overwrap*

The space shuttle booster joint overwrap is a design proposal to remedy the problem of large gap displacements in the booster joints when the rocket is in operation. The proposal calls for an overwrap of graphite-epoxy material on the outer surface of the rocket casing, near the joint. In theory, the presence of the overwrap would help increase the flexural stiffness of the joint and thus reduce the undesirable gap displacement. In this case study, the booster wall serves as the mandrel and is consequently not removed at the end of fabrication.

7.1.1 Overwrap Proposal

A schematic of the overwrap proposal is shown in Fig. 21. The steel casing has a thickness of 12.7 mm (0.5 in.) and an inside diameter of 3683 mm (145 in.). The overwrap has an overall thickness of 49.3 mm (1.94 in.) and the sides are sloped at an angle of 45 °. The width of the overwrap is 142.2 mm (5.60 in) at the top. The distance from the base edge of the overwrap to the joint is approximately 178 mm (7 in.). A strain gage is attached to the outside wall of the casing, at the center of the overwrap to provide experimental hoop strain data during fabrication.

The overwrap consists of 22 sets of the T40/982 Fiberite graphite-epoxy composite. Each of the first 21 sets contains a polar cloth layer, followed by 9 unidirectional hoop layers. The last set contains a polar cloth layer and 2 hoop layers. Each polar cloth layer is a woven fabric layer with most of the fibers running along the axis of the casing (wrap angle = 90°) and has a thickness of 0.254 mm (10

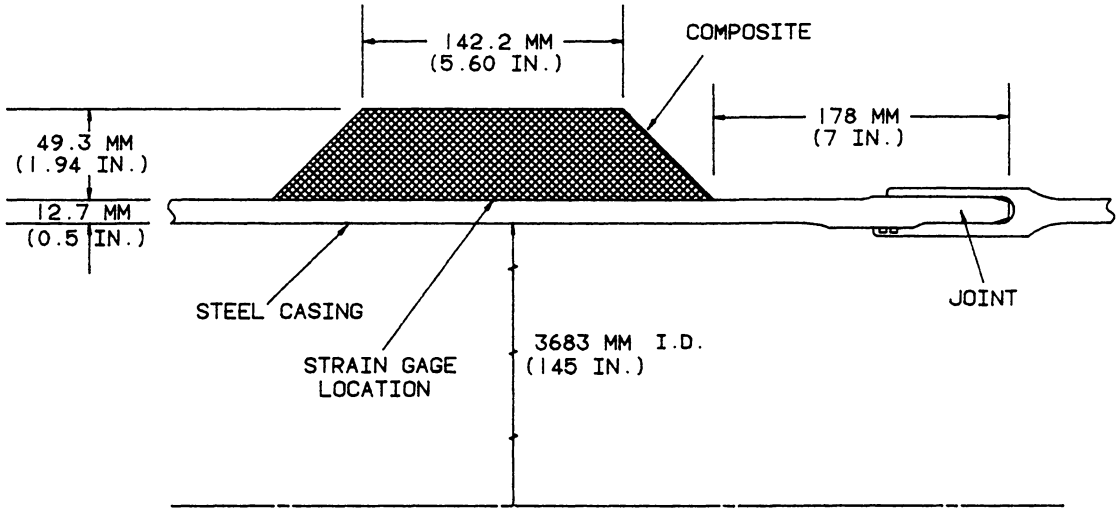

Figure 21. Space Shuttle Booster Joint Overwrap Proposal

mils). Each hoop layer (wrap angle = 0°) has a thickness of 0.229 mm (9 mils). The winding force in the hoop layers varies linearly from 67 N (15 lbf) in the innermost set to 9 N (2 lbf) in the outermost set. The tow area, i. e., the cross-sectional area of the fiber band, is given as 0.19 mm^2 (3.0×10^{-4} $in.^2$). The corresponding spool tension in the hoop layers can be computed by dividing the winding force by the tow area. The winding tension in the hoop layers is computed from this spool tension and the fractional instantaneous tension loss. Due to lack of experimental data, a typical value of 50% is assumed for the instantaneous tension loss. Consequently, the computed winding tension varies from 136.1 MPa (19.74 kpsi) in the innermost layer to 18.14 MPa (2.63 kpsi) in the outermost layer. The polar cloth layers are laid on with negligible tension; however, they are given a small tension of 34.5 kPa (5.0 psi) so that their stiffness is not degraded during winding. The whole winding process takes about 6 hours, translating to an average of 100 seconds per layer.

After winding, the overwrap undergoes a cure cycle which includes a heatup from an ambient temperature of 32°C (90 ° F) to an intermediate temperature of 68°C (155°F), which is sustained for 20 hours, and then to a cure temperature of 99°C (210°F), which is sustained for another 10 hours. Afterward, the overwrap is allowed to cool back down to the ambient temperature. A plot of the cure cycle for the 982 epoxy resin, up to the end of the 37^{th} hour is shown in Fig. 22.

7.1.2 Finite Element Model

The WACSAFE finite element model of the overwrap is shown in Fig. 23. In the finite element model, mid-plane symmetry has been utilized so that only half of the

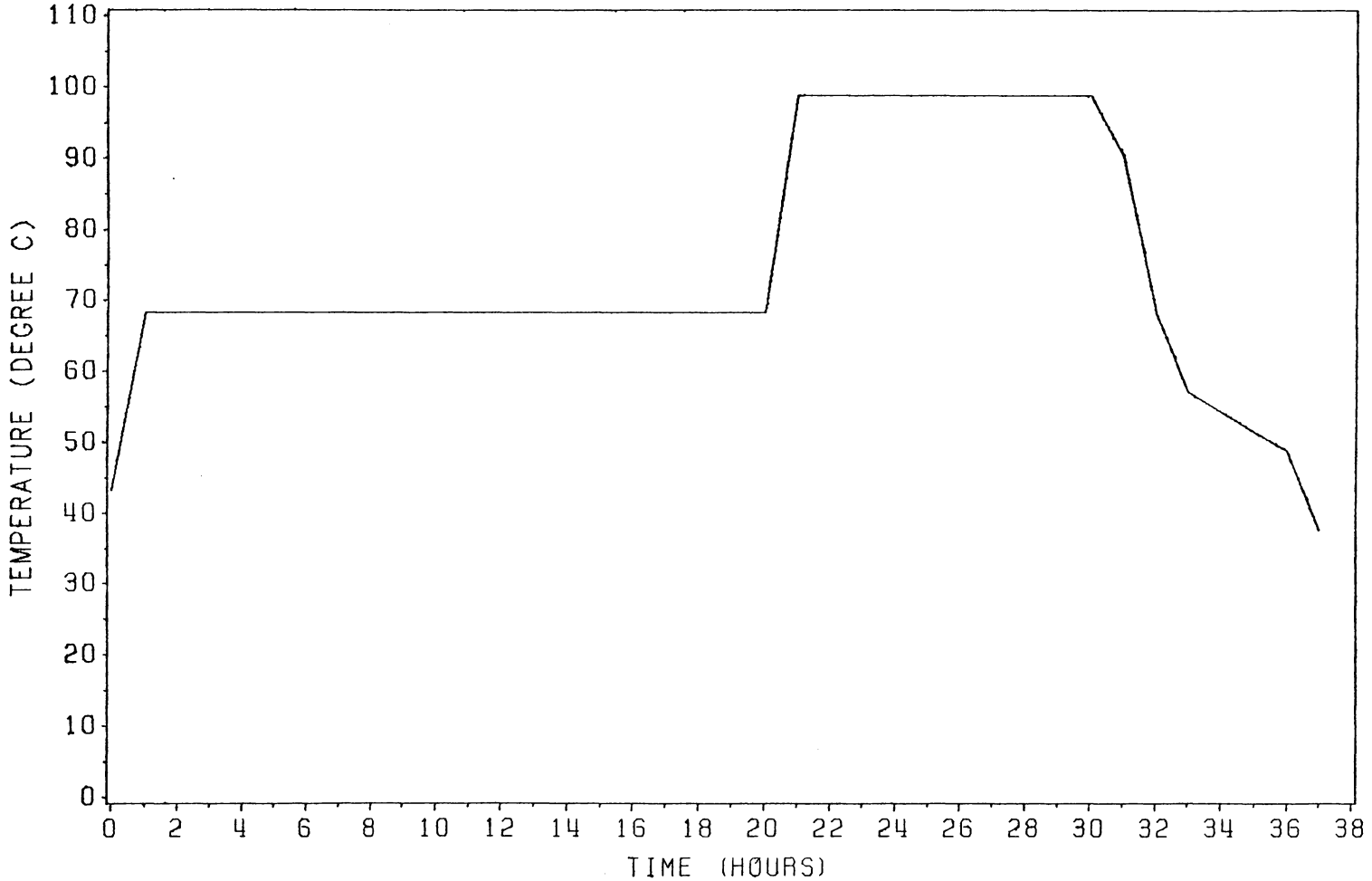

Figure 22. Cure Cycle for the Overwrap

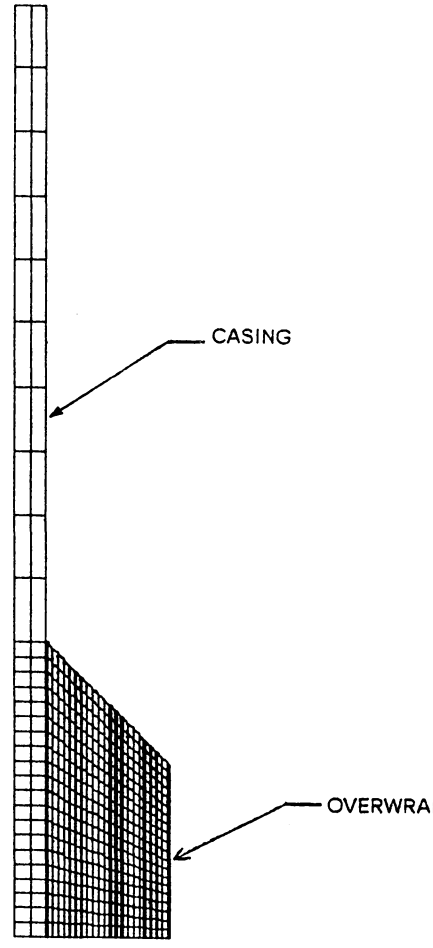

Figure 23. Finite Element Model for Overwrap

overwrap needs to be modeled. A total of 1017 nodes and 940 elements were used in the model.

The steel casing was modeled with two layers of elements which extend 254 mm (10 in.) beyond the overwrap. An extension of 254 mm (10 in.) was used in the model instead of the real length of 178 mm (7 in.) because the casing is slightly stiffer at the joint due to the somewhat greater thickness there. The extra extension of 76 mm (3 in.) was used to compensate for the constant casing thickness in the finite element model.

To reduce the model size and the execution time, elements in the hoop layers were made to contain more than one layer each. In each winding set, the polar cloth layer was modeled with one element layer and the 9 hoop layers were modeled with another element layer. Thus, only two element layers were used to model each winding set. In the last winding set, the final two hoop layers were modeled with one element layer. In all, 44 element layers were used. A close up view of the first 4 composite element layers is shown in Fig. 24. In each step, an element layer was turned on. Consequently, there were 44 winding steps in the model.

The only boundary conditions imposed on the models are the restriction of the nodes on the line of symmetry from moving in the z direction to preserve symmetry and to eliminate the free body motion mode of displacement from the model.

The thermo-mechanical material properties used for the analysis are listed in Table 3 for both the steel casing and the composite overwrap. The material properties of the composite are listed for both the uncured material and the cured material. The degree of cure at gel for the 982 resin was assumed to be 0.67.

The thermo-kinetic cure model provided the thermo-kinetic data for the curing stage of the overwrap up to the 37^{th} hour. The heatup stage was modeled with 7 steps with time increments of 1 hour, 2 hours, 2 hours, 10 hours, 5 hours, 5 hours, 3 hours,

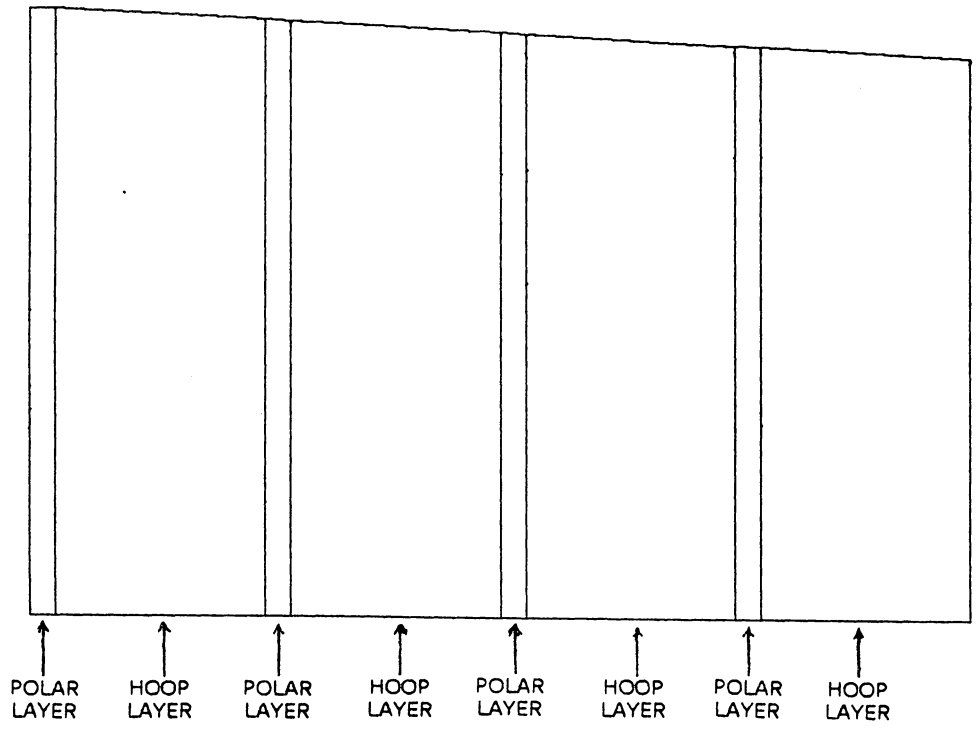

Figure 24. Close Up View of the First Four Composite Element Layers

Table 3. Material Properties for Overwrap Analysis

T40/982 COMPOSITE MATERIAL:			
E_1	=	166 GPa	(2.40×10^7 psi)
E_2 (uncured)	=	3.86 GPa	(5.6×10^5 psi)
E_2 (cured)	=	7.72 GPa	(1.12×10^6 psi)
E_3 (uncured)	=	3.86 GPa	(5.6×10^5 psi)
E_3 (cured)	=	7.72 GPa	(1.12×10^6 psi)
ν_{23}	=	0.300	
ν_{31} (uncured)	=	0.007	
ν_{31} (cured)	=	0.014	
ν_{21} (uncured)	=	0.007	
ν_{21} (cured)	=	0.014	
G_{12} (uncured)	=	0.414 GPa	(6.0×10^4 psi)
G_{12} (cured)	=	4.14 GPa	(6.0×10^5 psi)
α_1	=	9.0×10^{-7} / °C	(5.0×10^{-7} / °F)
α_2	=	2.05×10^{-5} / °C	(1.14×10^{-5} / °F)
α_3	=	3.76×10^{-5} / °C	(2.09×10^{-5} / °F)
Fiber Modulus	=	276 GPa	(4.0×10^7 psi)
Fiber Radius	=	3.0×10^{-3} mm	(1.18×10^{-4} in.)
Volume Fraction	=	0.638	
Viscosity (at 32 °C or 90 °F) (976 resin)	=	0.3725 Pa-sec.	(5.401×10^{-4} psi-sec.)

STEEL CASING:			
E	=	200 GPa	(2.90×10^7 psi)
ν	=	0.32	
α	=	1.17×10^{-5} / °C	(6.50×10^{-6} / °F)

and 7 hours, totaling 30 hours. The cooling stage was modeled in two steps, the first step ends at the 37^{th} hour into the curing stage and the second step ends when the overwrap is completely cooled down to the ambient temperature.

The viscosity data for the 982 resin was not available at the time of the analysis. Instead, viscosity data of the 976 resin was used. The 976 resin is known to have higher viscosity than the 982 resin.

The analysis was run with the equilibrium iteration option flag set to 3, which means the iteration was activated for every load step.

7.1.3 Results and Discussions

Theoretical results are compared with experimental data (supplied by Morton Thiokol) in Fig. 25 for the winding stage and in Fig. 26 for the curing stage. These figures are plots of the hoop strain in the casing, at the location of the strain gage (see Fig. 21), as a function of the number of winding sets.

The theoretical hoop strain plotted in Figs. 25 and 26 is actually the average value for the mandrel element closest to the point of measurement. In other words, the WACSAFE hoop strain data is for the point at the center of this element, a point which is neither on the surface nor at the center of the overwrap. However, since the element is small, the center point of the element is very close to the center of the overwrap (see Fig. 23). Furthermore, since the wall thickness is very small compared to the casing diameter (see Fig. 21), the hoop strain should not vary significantly through the wall thickness. As a result, the plotted hoop strain should be a good approximation of the hoop strain at the point of measurement.

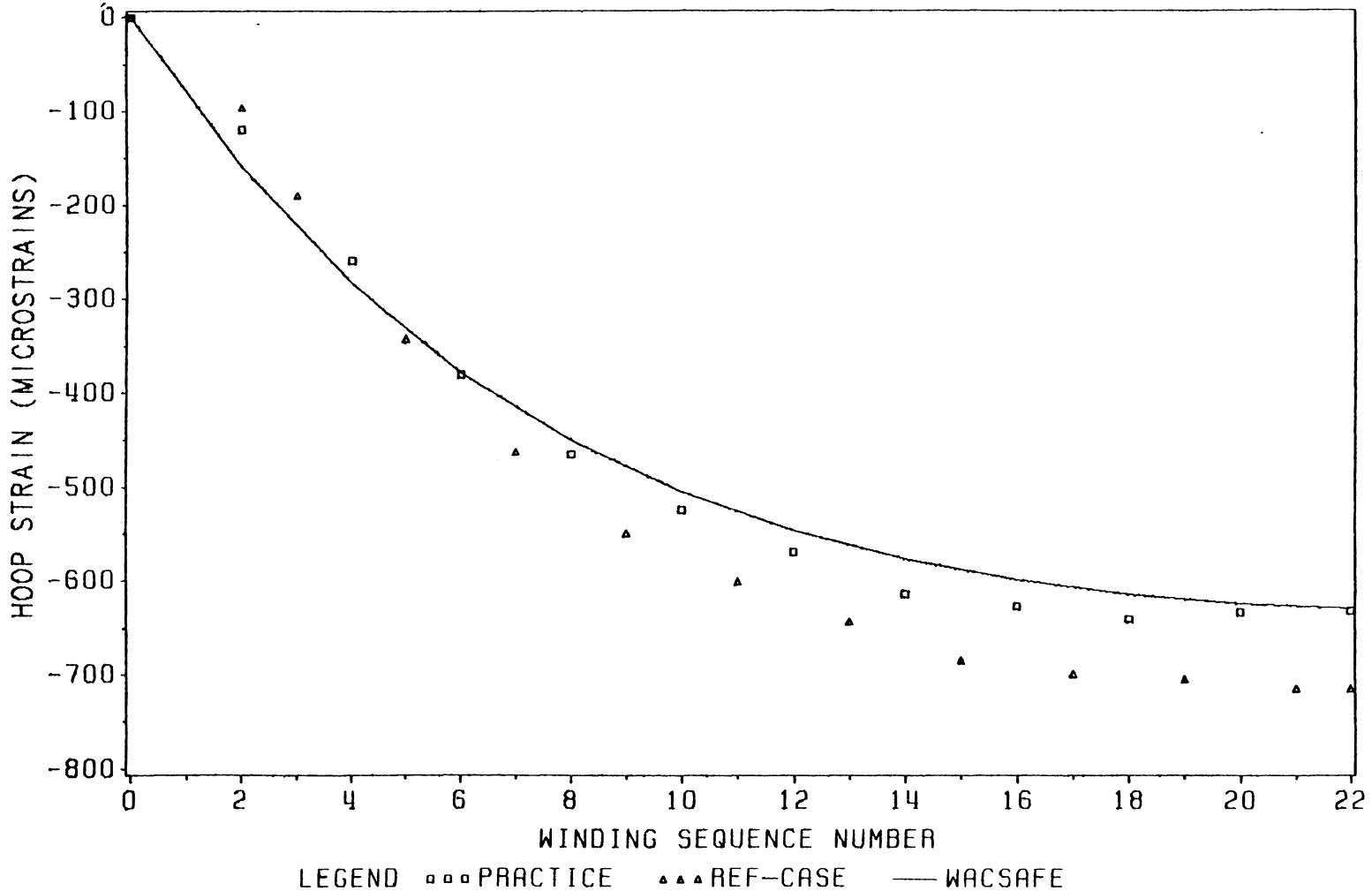

Figure 25. Comparison of WACSAFE Results with Experimental Data (Winding)

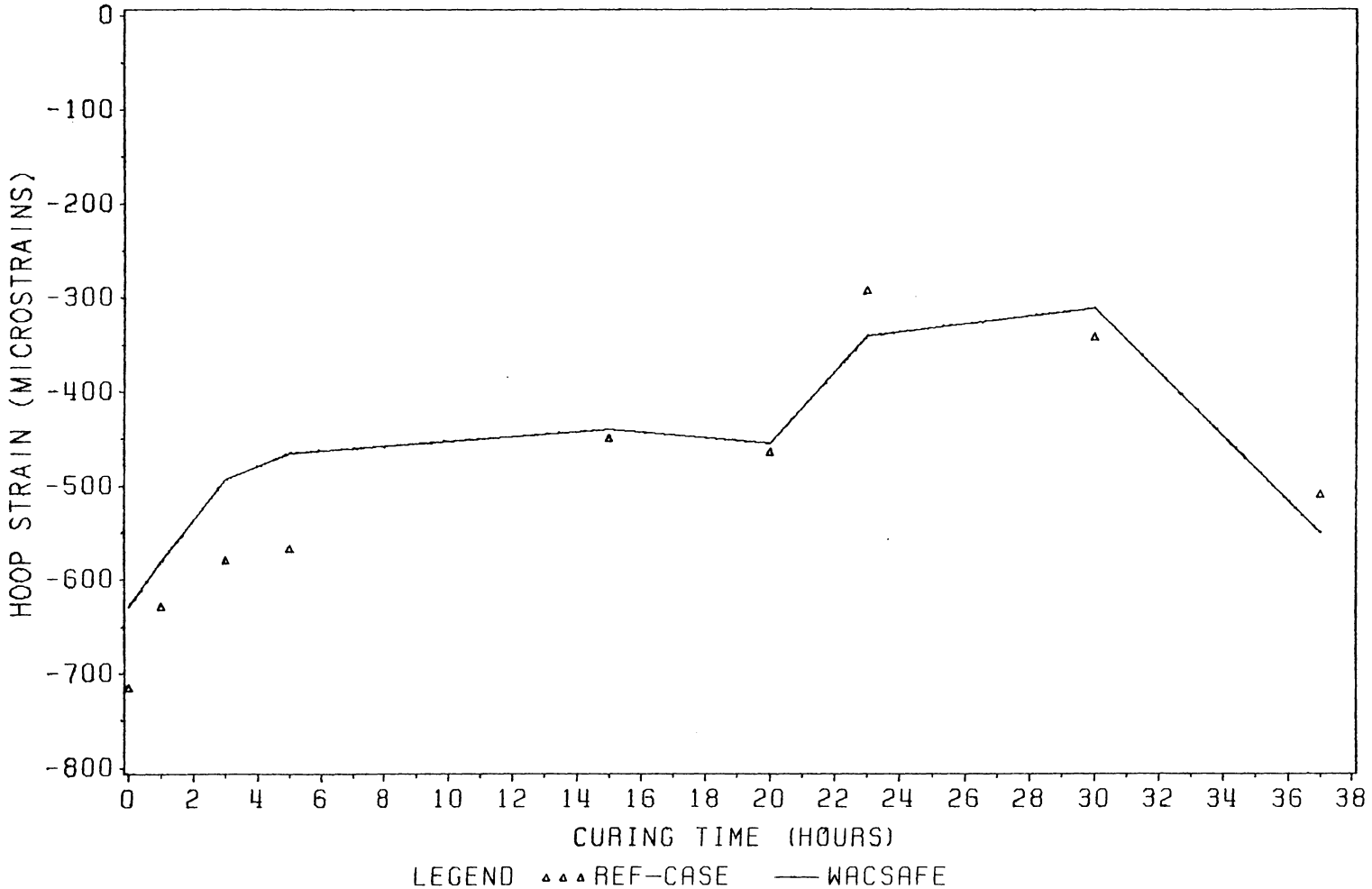

Figure 26. Comparison of WACSAFE Results with Experimental Data (Curing)

Two experimental data sets are available for the winding stage: practice winding and referee case winding. They are labeled in Fig. 25 as 'practice' and 'ref-case'. In each of the experimental data sets, values of hoop strain are provided at every other winding step. Figure 25 shows excellent agreement between WACSAFE results and the practice winding data set. The WACSAFE curve has the same concave shape as the practice winding data. Furthermore, the last data point of this experimental data set falls almost exactly on the WACSAFE curve at the end of winding. The hoop strains in the referee winding set are somewhat greater than both the WACSAFE results and the other experimental data set, with a difference of about 80 μin./in. at the end of winding. These curves show that the fabrication stress model yields accurate results for the winding stage, within the limits of the assumptions.

Only one experimental data set is available for the curing stage: the referee winding set. Fig. 26 shows lower level of hoop strain in the WACSAFE result from the beginning of curing up to the 6^{th} hour, with the difference coming from the winding stage. Between the 6^{th} hour and the 16^{th} hour, the WACSAFE curve has come up to the hoop strain level of the experimental data set, implying that the WACSAFE result exhibits smaller tension loss than the experimental results during winding. This is expected since the 976 resin, whose viscosity data was used in the analysis, has much higher viscosity than the 982 resin. After the 16^{th} hour, the WACSAFE curve shows excellent agreement with the experimental data set. Thus, other than the lower tension loss exhibited by the WACSAFE result in from the 6^{th} to the 16^{th}, when most fiber motion is suspected to occur, the WACSAFE curve shows excellent agreement with experimental data.

Various components of the fabrication stresses in the overwrap at the end of winding, heating, and curing are plotted in Figs. 27 to 38. In these figures, the stresses are plotted from the center plane of the overwrap to the free edge, starting

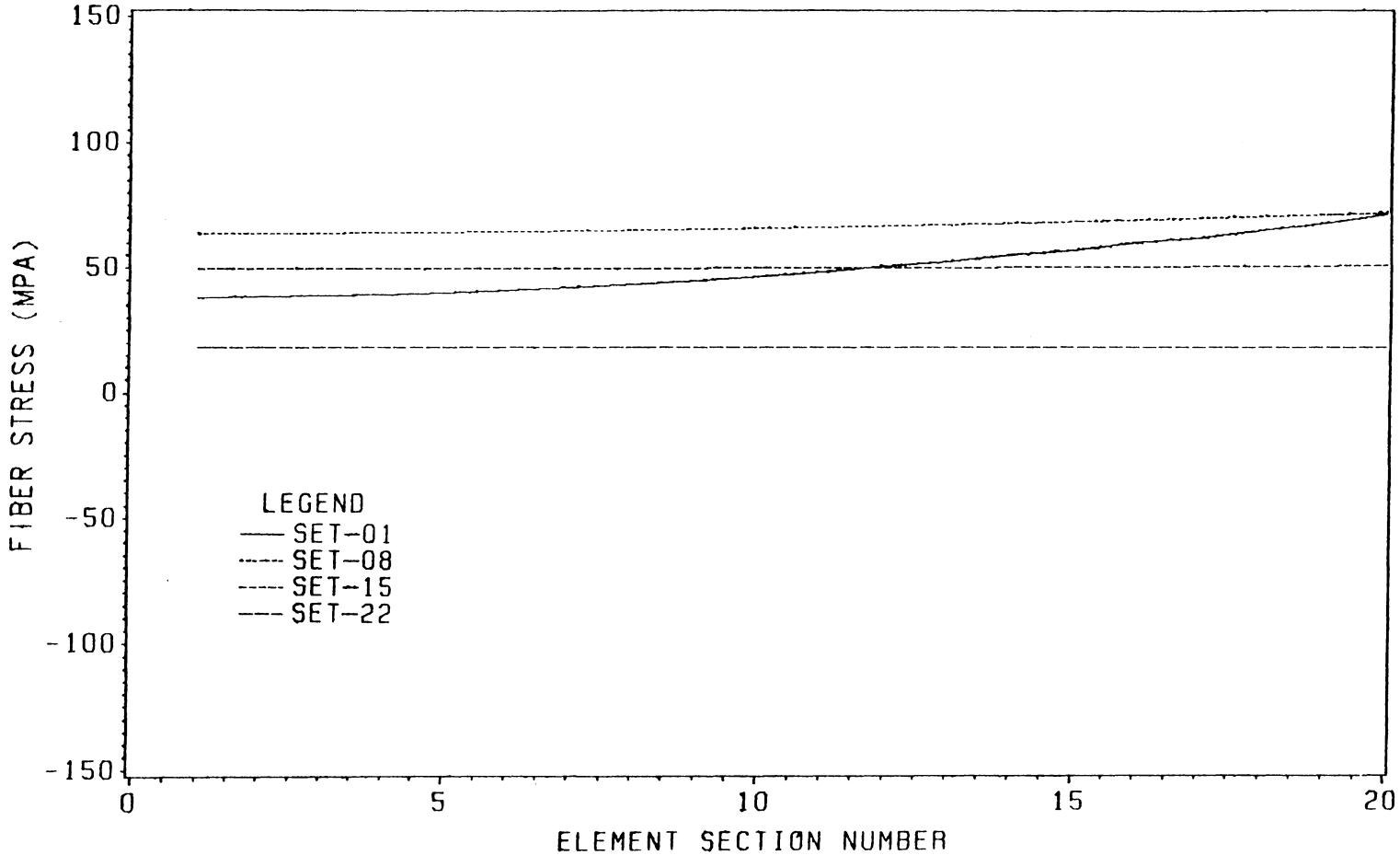

Figure 27. Fiber Stress in Hoop Layers after Winding

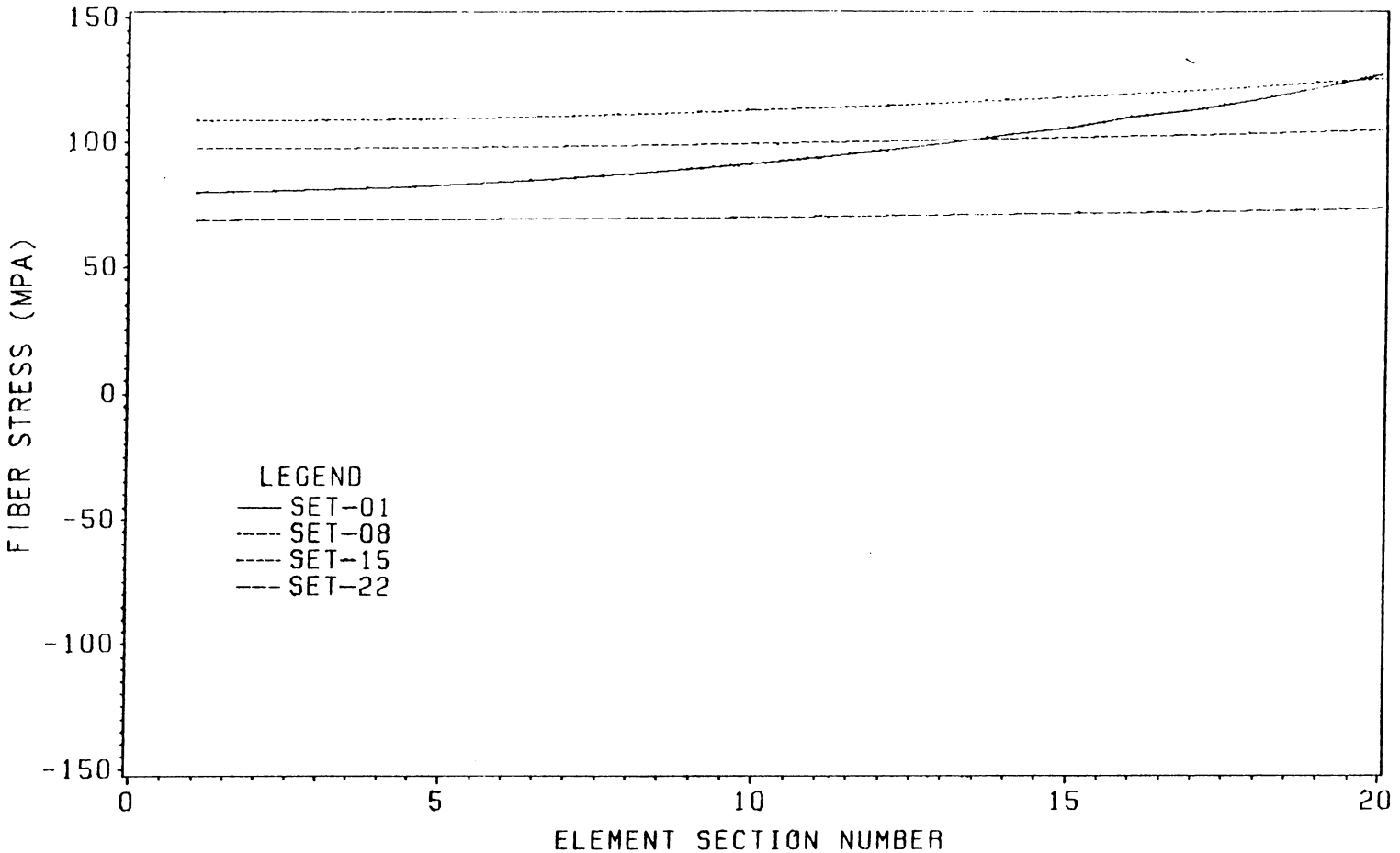

Figure 28. Fiber Stress in Hoop Layers after Heating

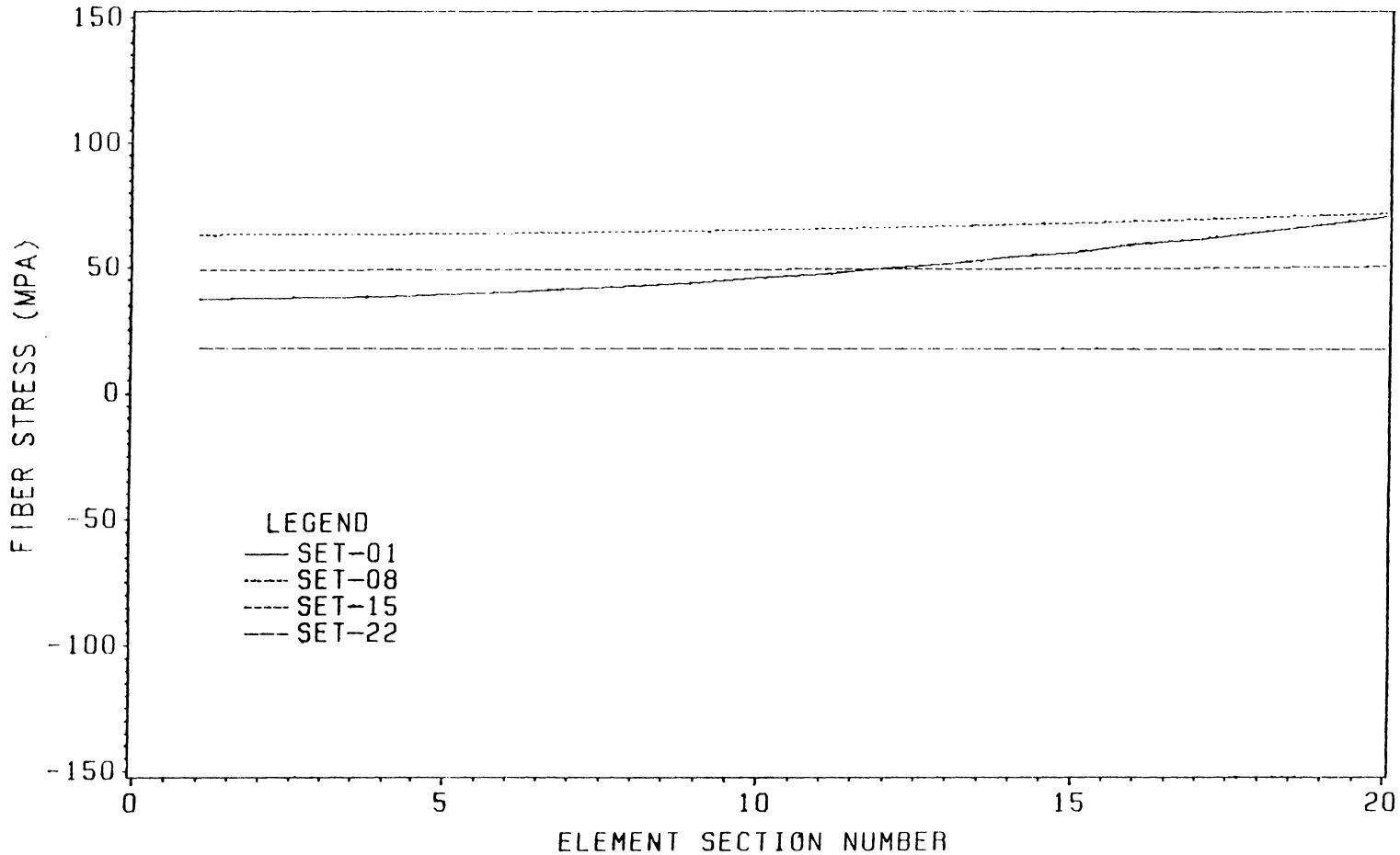

Figure 29. Fiber Stress in Hoop Layers after Cooling

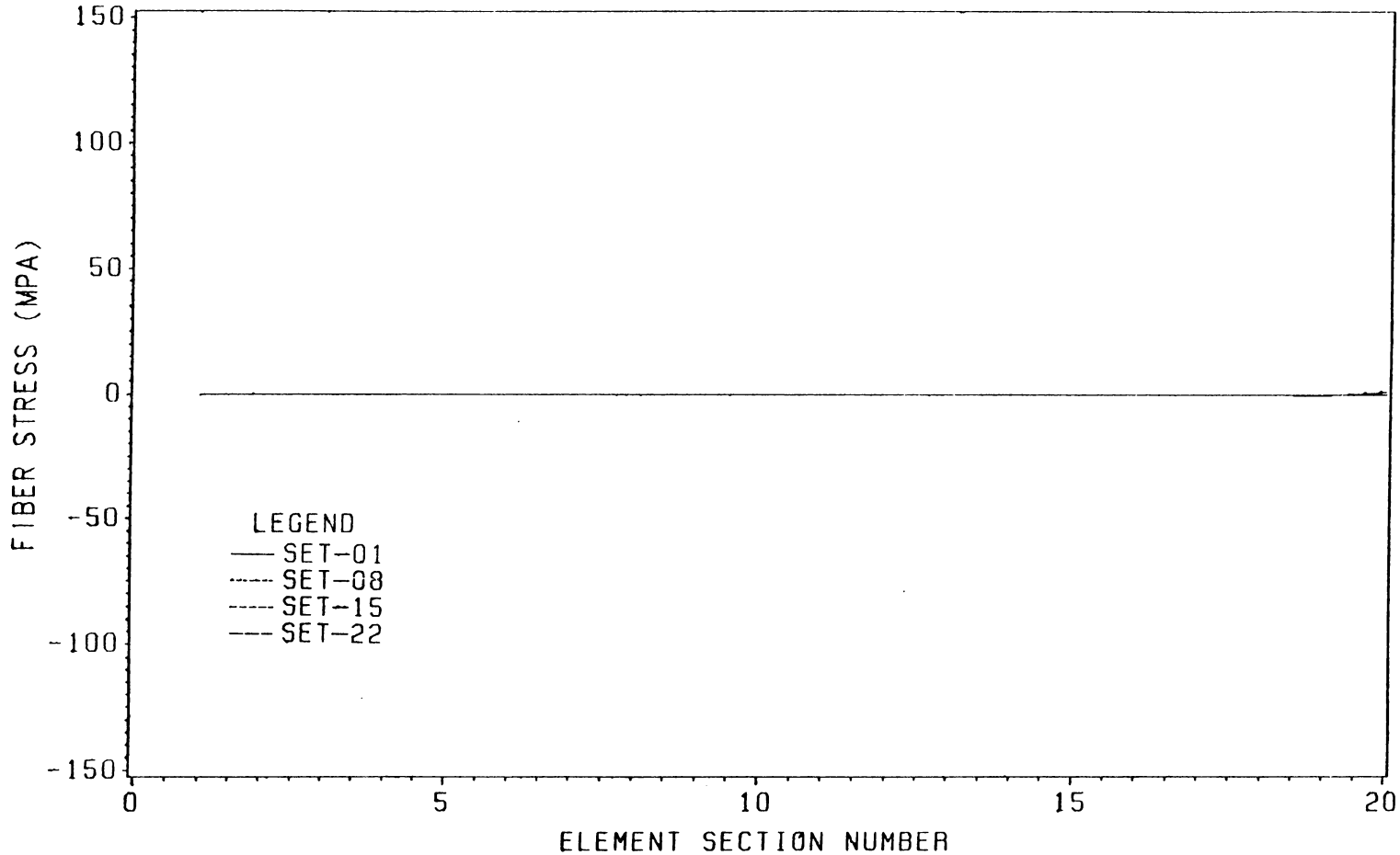

Figure 30. Fiber Stress in Polar Layers after Winding

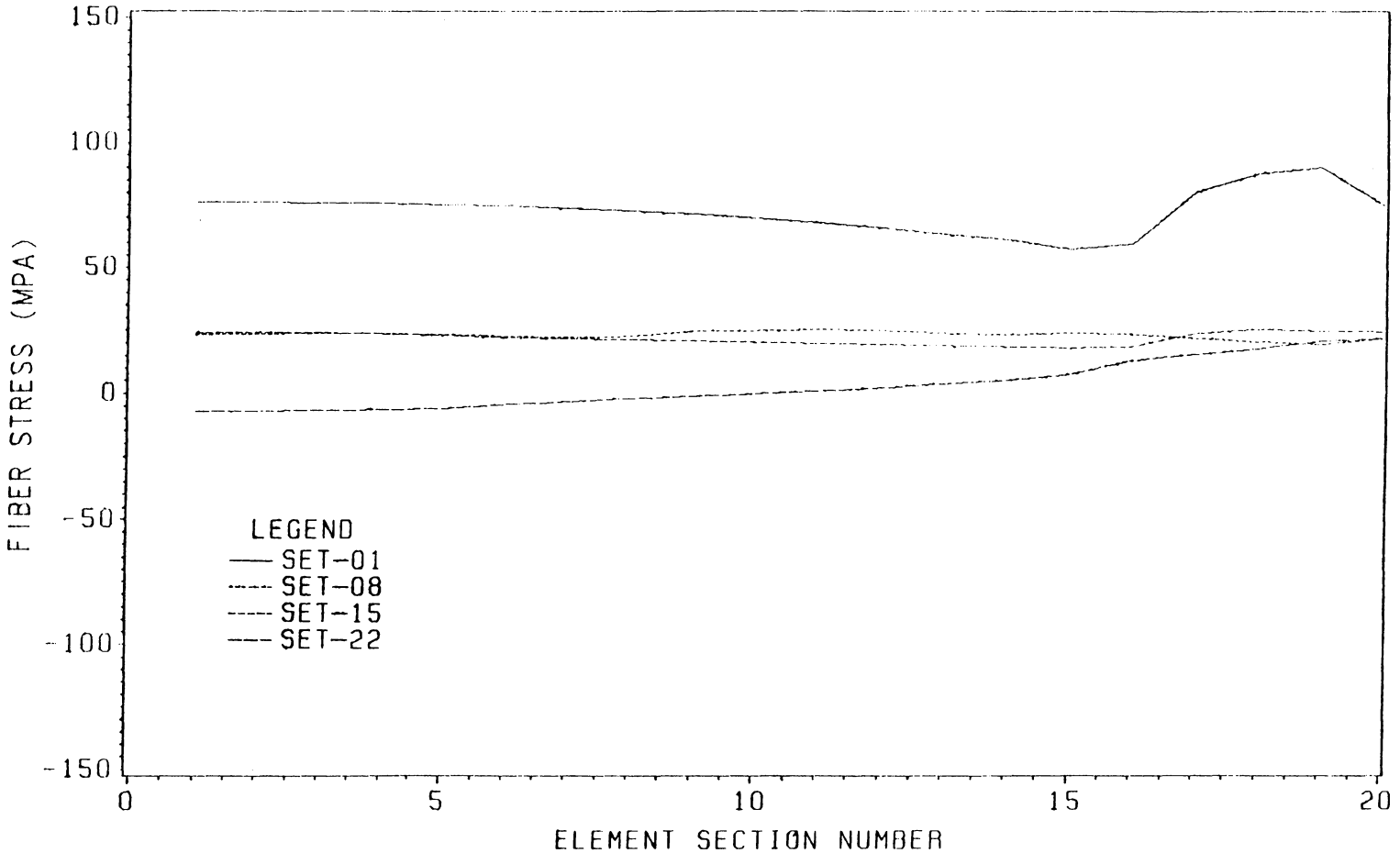

Figure 31. Fiber Stress in Polar Layers after Heating

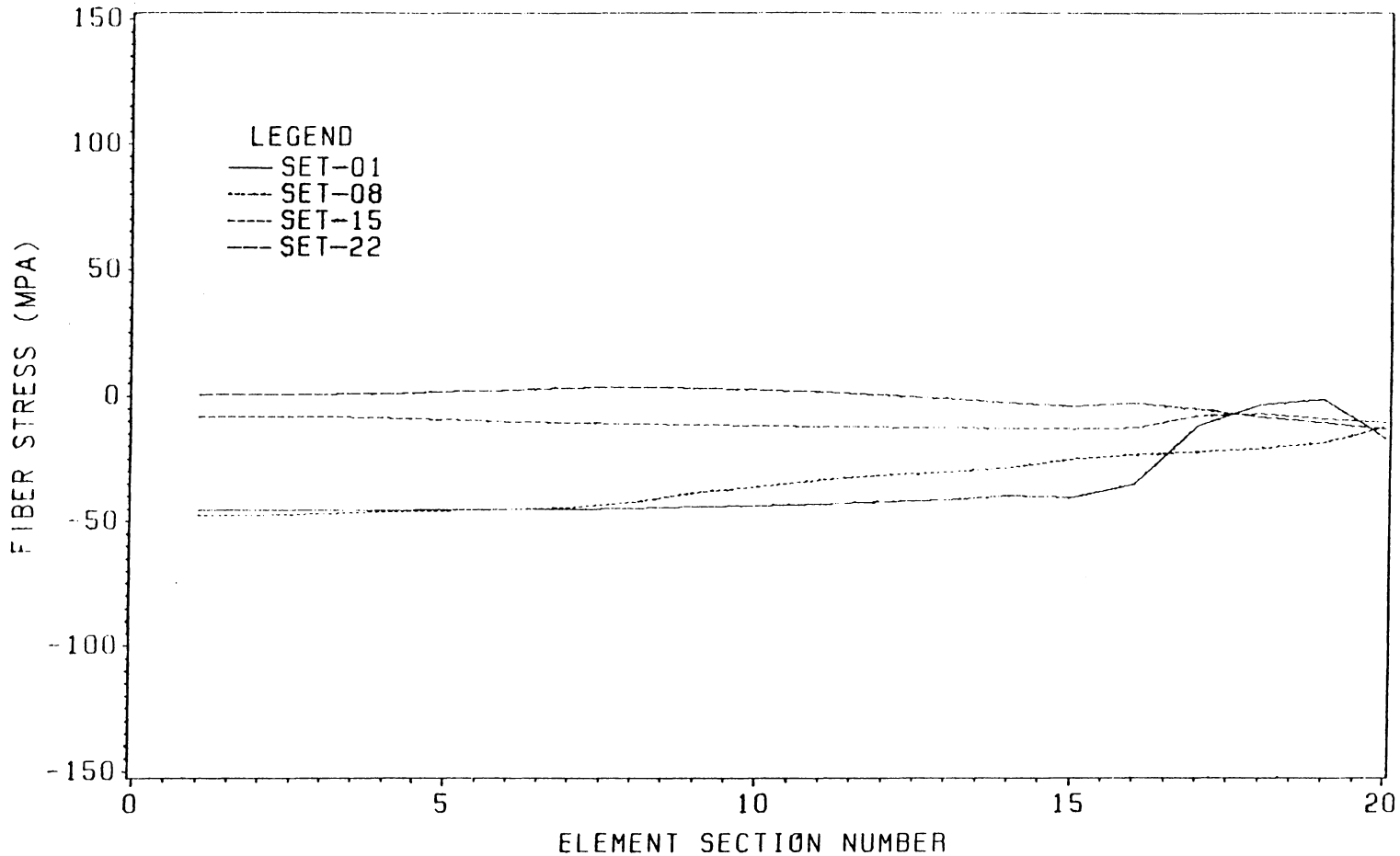

Figure 32. Fiber Stress in Polar Layers after Cooling

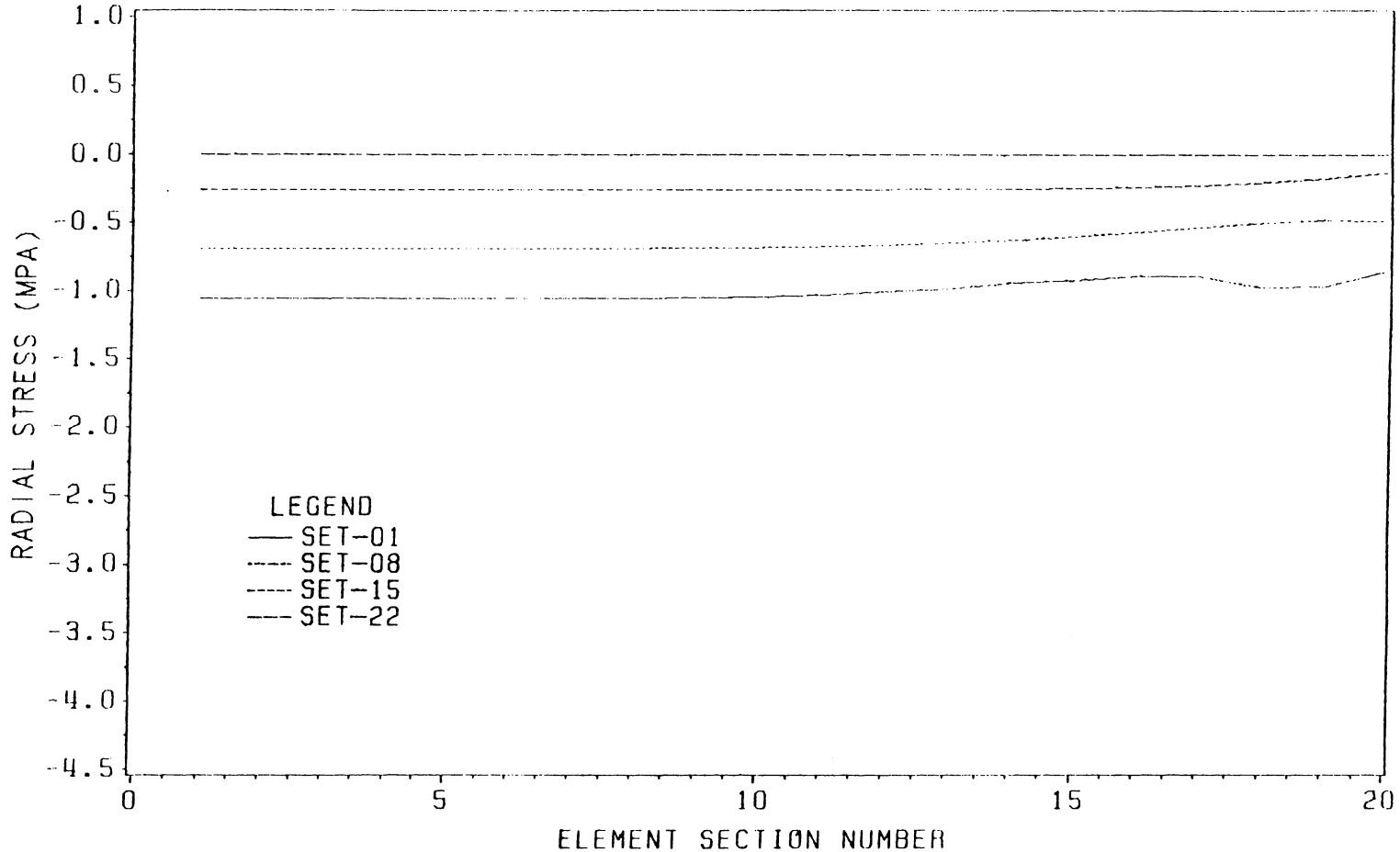

Figure 33. Radial Stress in Hoop Layers after Winding

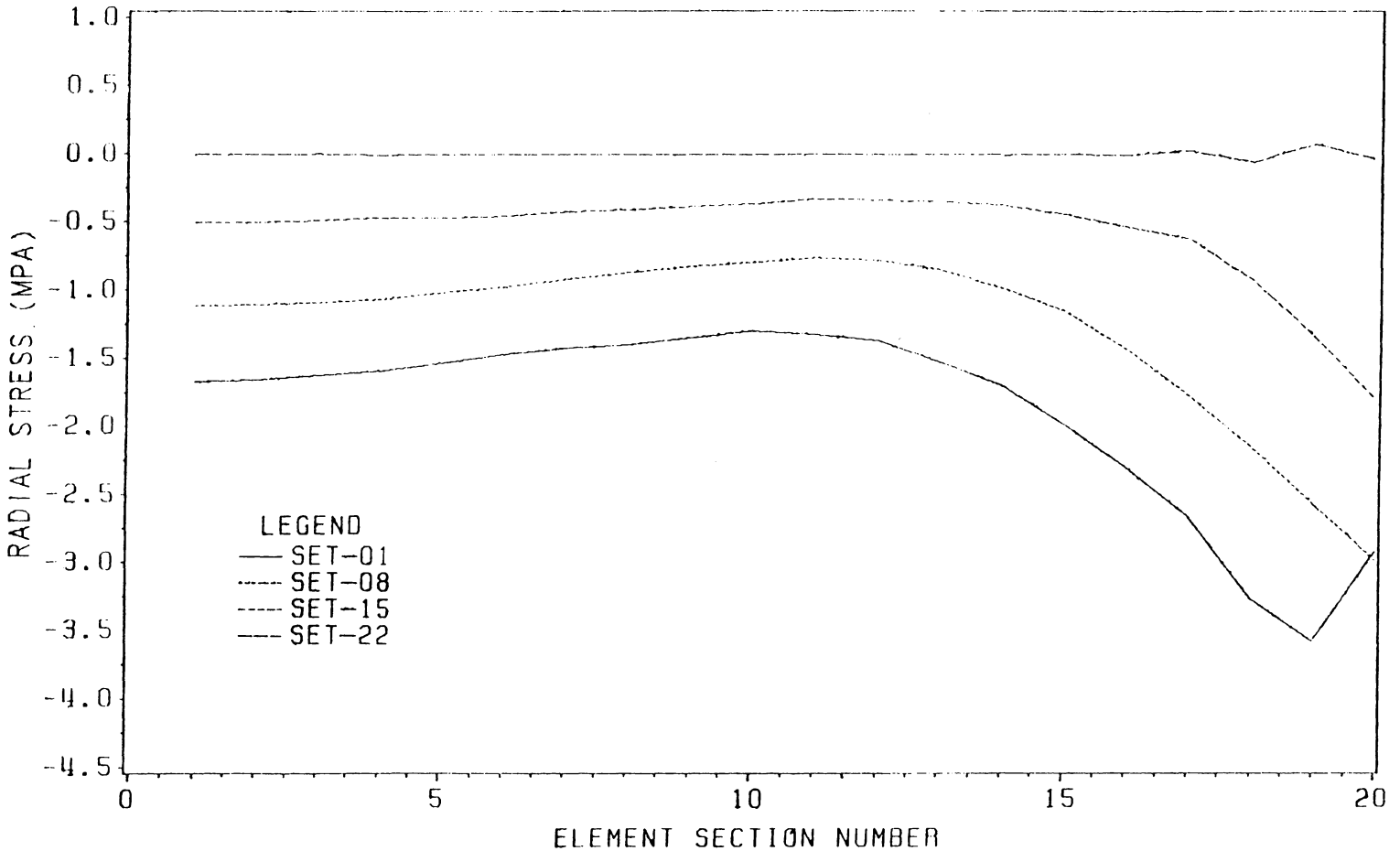

Figure 34. Radial Stress in Hoop Layers after Heating

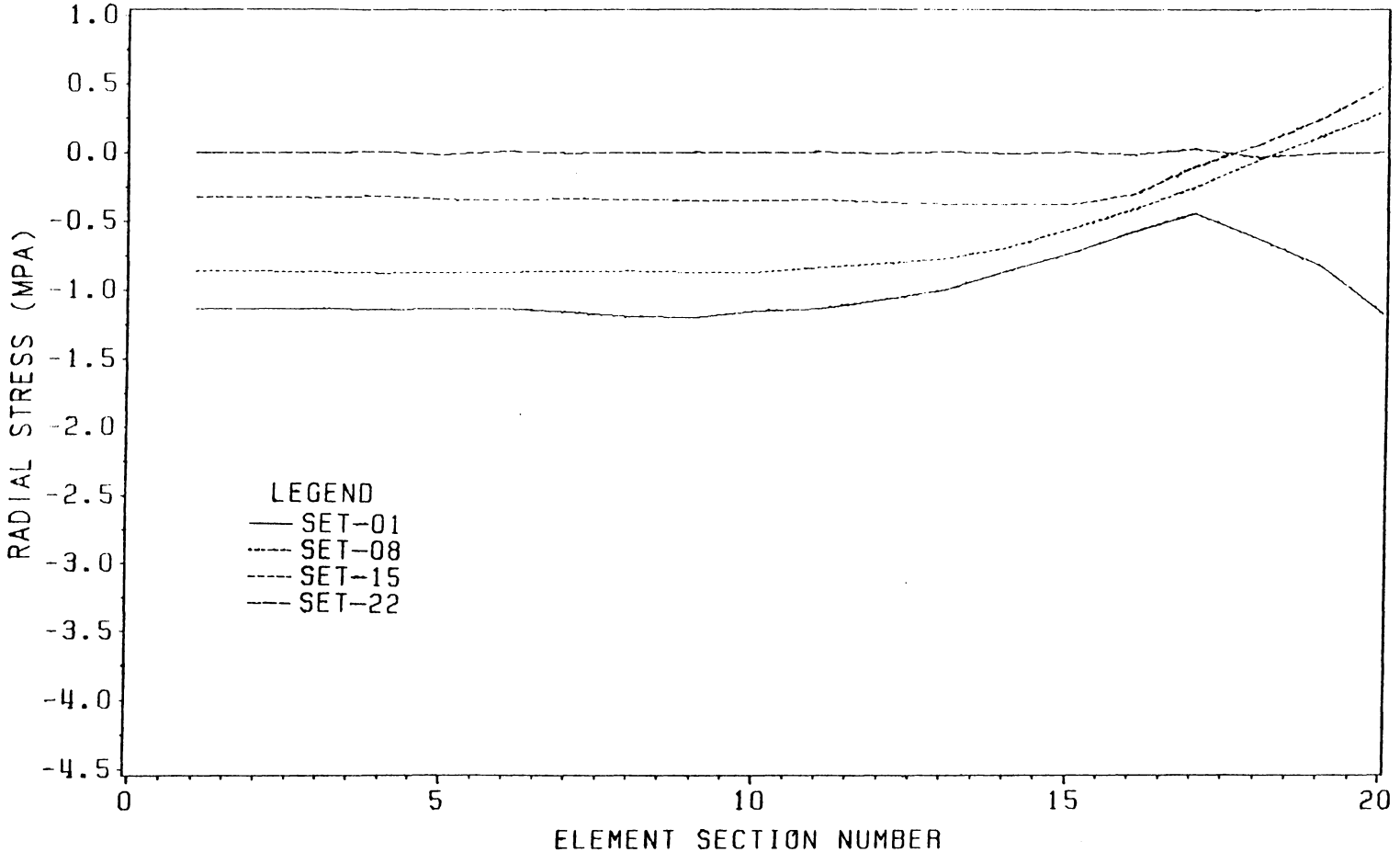

Figure 35. Radial Stress in Hoop Layers after Cooling

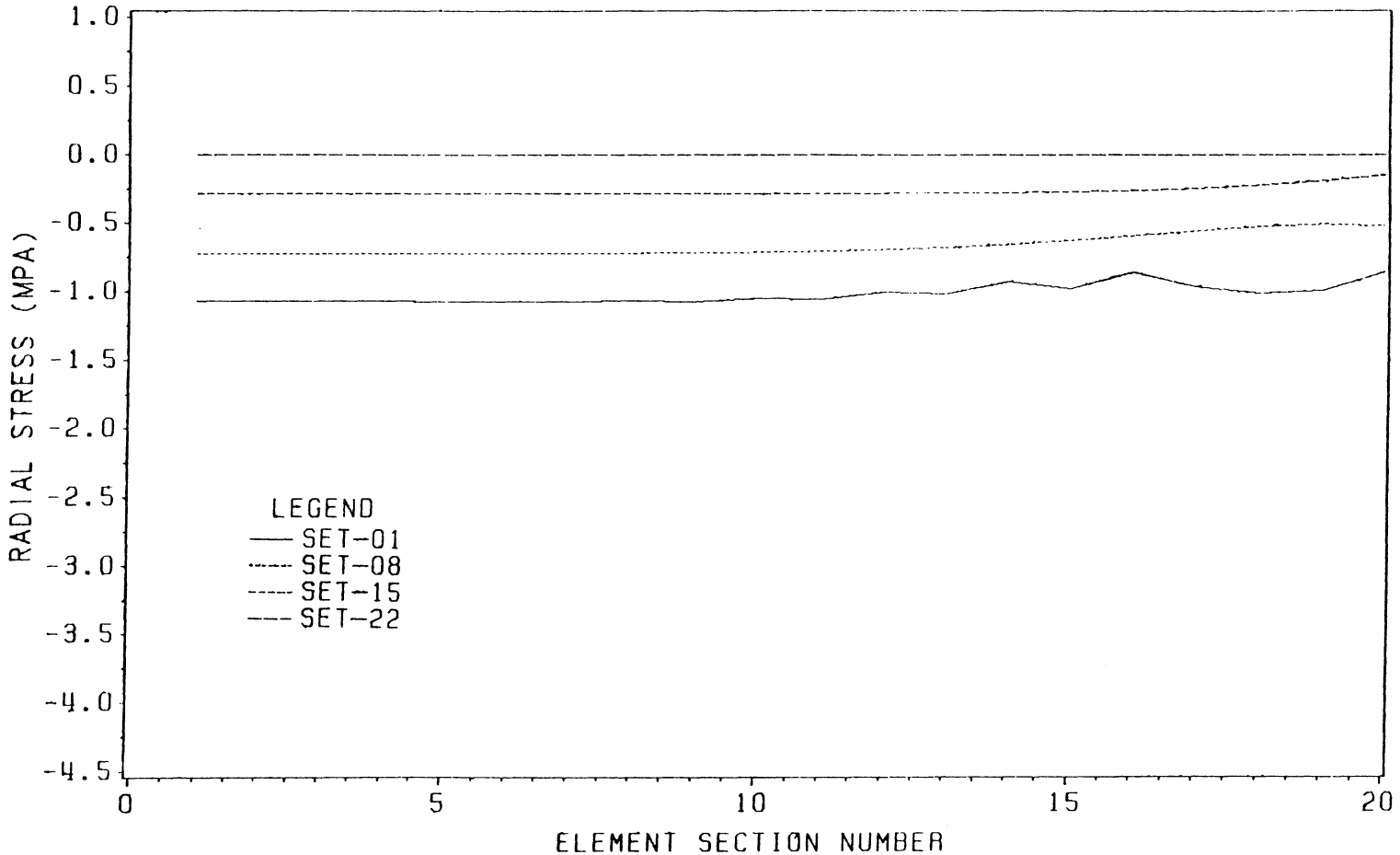

Figure 36. Radial Stress in Polar Layers after Winding

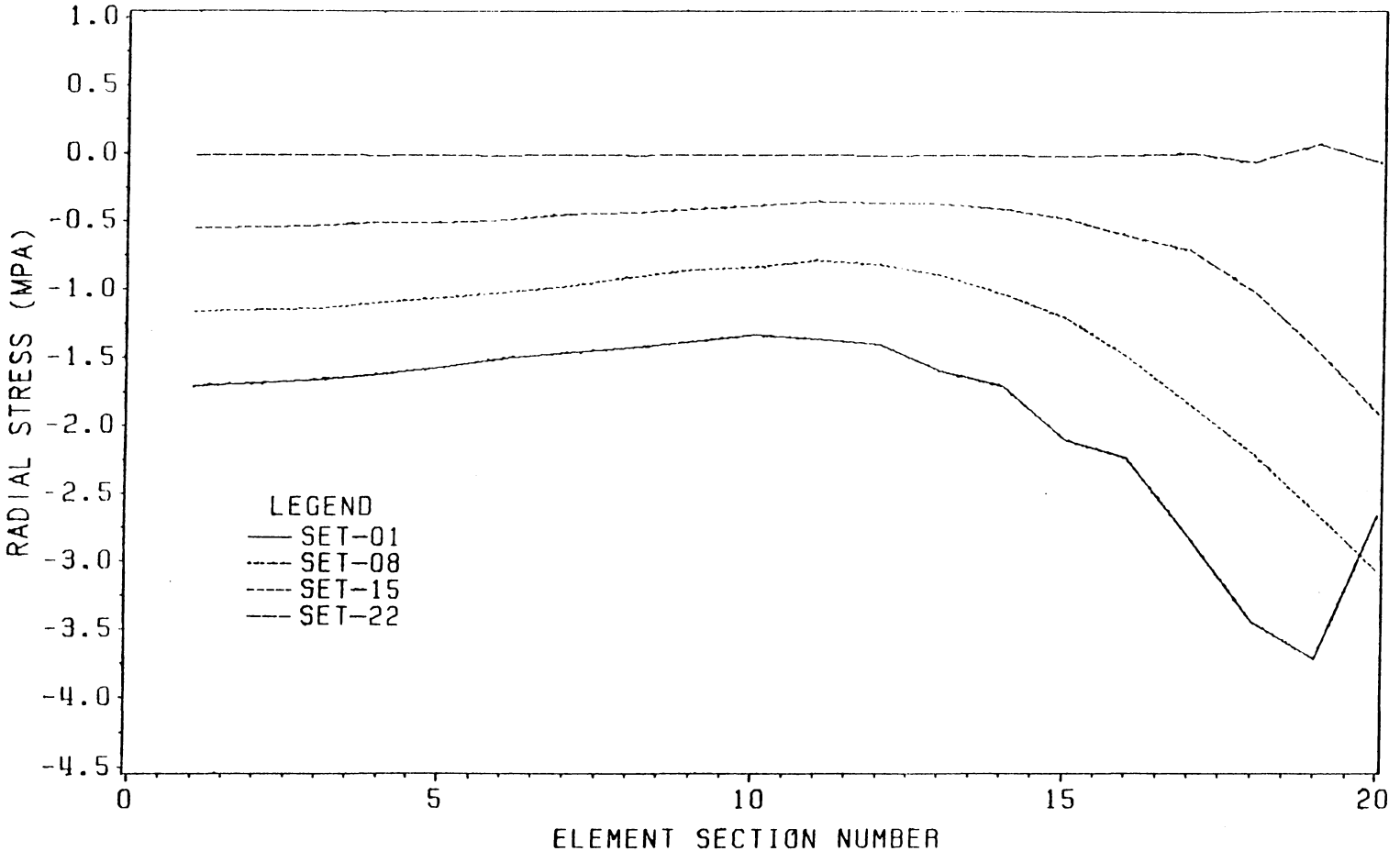

Figure 37. Radial Stress in Polar Layers after Heating

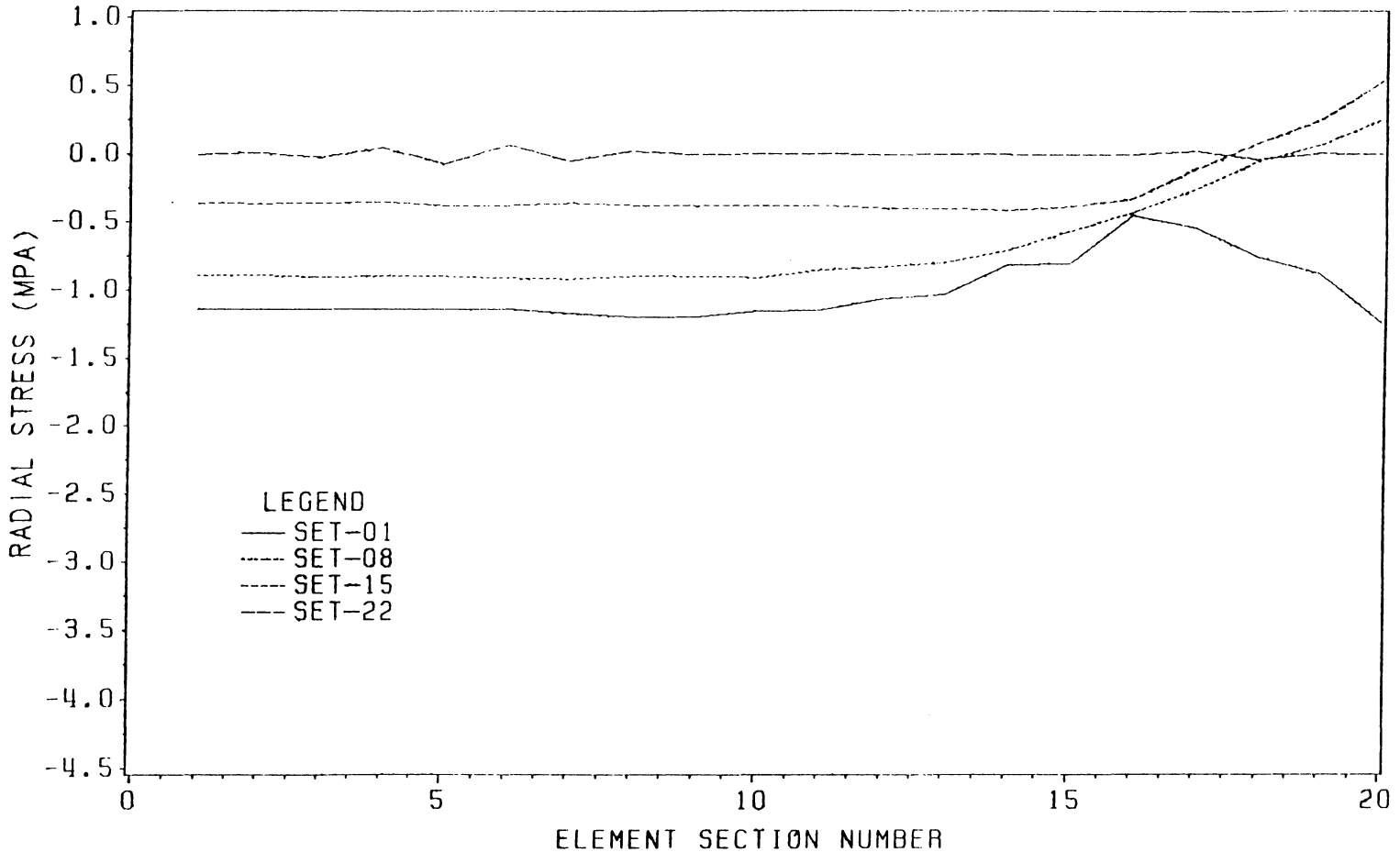

Figure 38. Radial Stress in Polar Layers after Cooling

with element section 1 as the elements closest to the center and element section 20 as the elements along the free edge.

Figures 27 to 29 show the fiber stresses in the hoop layers. In these figures, all hoop fibers are in tension at any stage of fabrication. At the center of the overwrap, the innermost layers have lost more tension than the middle and outer layers after winding. As a result, the maximum fiber stresses are located in the middle layers instead of the innermost layers. After heatup, all hoop layers are driven up into tension, gaining an average of about 45 MPa (6.5 kpsi). The distribution of the fiber stresses in the layers are not changed significantly, however. After cooling, the fiber tensions in the layers come back down to the same level as after winding. The stress curves after winding and after cooling are almost identical, the reason being the effects of the different material formulations for uncured and cured are not apparent for hoop or polar layers. Thus, the only sources of difference come from the different mechanical properties of the uncured and cured materials and the fiber motion during the heatup stage.

Figures 30 to 32 show the fiber stresses in the polar layers. The fiber stresses in the polar layers are practically zero at the end of winding, indicating that the fibers have lost all tension. After the heating stage, however, the fibers in the polar layer gain a lot of tension. This phenomenon can be explained by the curing of the composite. In the winding steps, the composite is uncured; therefore, the layers tend to slip along each other. In the curing stage, however, the composite become cured and the transverse expansion of the hoop layers drives the polar layers in to high tension through bonding of the layers. At the end of cooling, the fiber stresses in the polar layers become compressive from being pulled in by the transverse contraction of the hoop layers. Notice that after heating, the innermost layer exhibits a jump in tension level in the elements near the free edge. This phenomenon can be explained

by the fact that these elements are the only elements with tensile fiber stress at the end of winding. As a result, only these elements retain the full material properties while all other elements have degraded properties. This discontinuity in material properties produces the jump in the stress curve at the end of heating, which carries into the cooling stage.

Figures 33 to 35 show the radial (delamination mode) stresses in the hoop layers. These stresses are compressive at the end of winding and heating. Notice that the stress levels are higher at the end of heating than at the end of winding because the radial expansion of the casing generates a pressure on the inner surface of the overwrap, driving it into higher compression in the radial direction. After cooling, radial stresses in the hoop layers are also compressive, except near the free edge for some middle and outer layers. The inner layers, however, have compressive radial stresses everywhere.

Figures 36 to 38 show the radial stresses in the polar layers. These stresses exhibit almost identical behavior as the radial stresses in the hoop layers. This similarity is expected since the through-the-thickness stresses should be continuous across the layers. The fact that the radial stresses in all inner layers are compressive after fabrication, i. e., at the end of cooling, indicates that there should be no separation of the composite overwrap from the casing at the end of fabrication.

The fiber strains at cure (in this case, after heating) are shown in Fig. 39. The figure shows that all layers have tensile fiber strains at cure, implicating that the fibers are cured straight and aligned. Consequently, there is no possibility of strength loss in the overwrap due to local fiber buckling. Notice that one needs not consider the fiber strains in the polar cloth layer for the determination of strength loss because of the inheritant waviness of the fibers in a woven fabric.

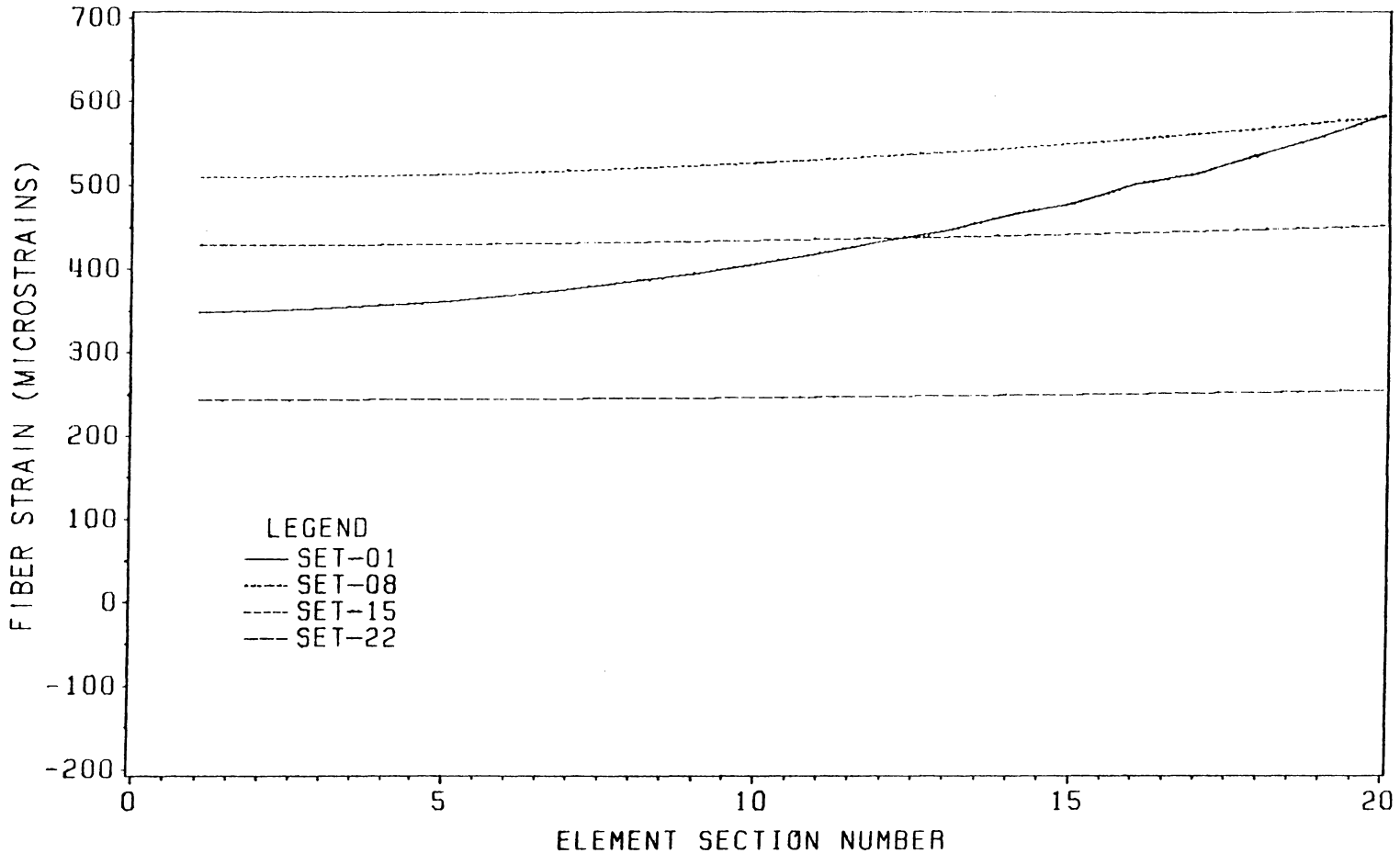

Figure 39. Fiber Strains at Cure in Overwrap

In summary, the fabrication stress analysis for the overwrap shows that the fabrication stress model yields hoop strain results which agree well with measured data for the winding stage. Also, the fabrication stresses and strains in the overwrap indicate that there should be no strength degradation in the final structure due to local fiber buckling and that there should be no overwrap-casing separation after fabrication.

7.2 *Filament Wound Bottle*

The filament wound bottle is fabricated by winding composite layers on a mandrel which is removed from the bottle after cure. This problem is more typical of the filament winding fabrication problem since the geometry is somewhat arbitrary and the winding pattern is more complex than the overwrap case. Also, the analysis carries through the mandrel removal stage. Unfortunately, there is no experimental data for this case. Therefore, the significance of the results stops with the examination for reasonable and explicable behaviors. A prediction of possible strength loss will also be made for this case based on the fabrication stresses and strains obtained.

7.2.1 Bottle Description

The bottle, shown in Fig. 40, is wound on a cast sand/PVA mandrel which is covered with a 1.52 mm (0.060 in.) layer of rubber insulation. The rubber layer is to act as an insulator when the bottle is in service. At the ends of the bottle are steel

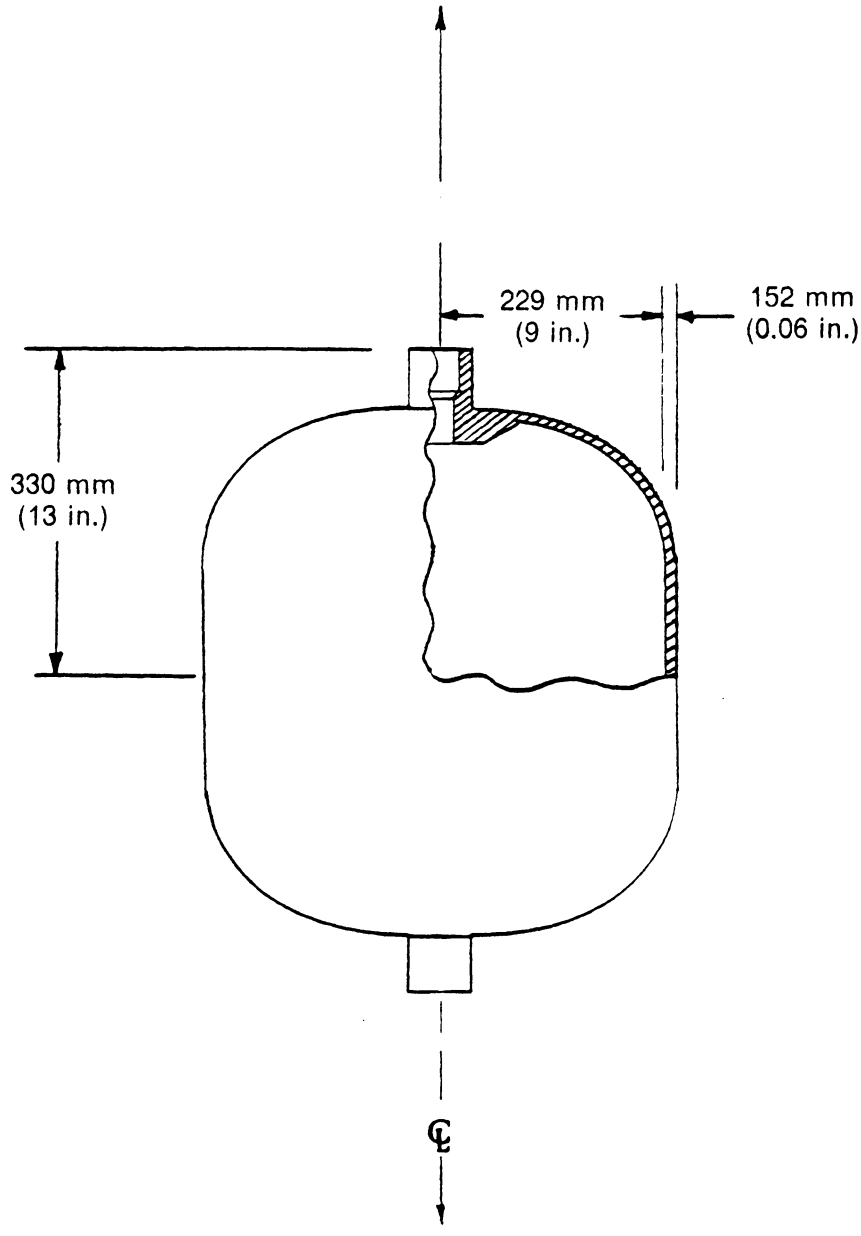

Figure 40. Schematic of Filament Wound Bottle

polar bosses which are to remain part of the bottle after fabrication. The mandrel and the rubber insulation together have an outside radius of 229 mm (9.0 in.) which forms the inside radius of the finished structure. The composite bottle, which is made out of the T300/976 prepreg graphite-epoxy system has a wall thickness of 1.52 mm (0.06 in.) in the dome region and 4.34 mm (0.171 in.) in the cylindrical region (excluding the rubber layer).

The winding pattern includes two helical layers, followed by two hoop layers in the cylindrical region only. Outside of these layers are two more helical layers. Thus, there are six composite layers in the cylindrical region and only four in the dome region. The helical layers have a wrap angle of 77° in the cylindrical region. Moving up the dome toward the polar boss, the wrap angle decreases gradually to a value of 0° at the very top.

The winding force was given to vary between 22 N (5 lbs) and 31 N (7 lbs) for a tow area of 9.78×10^{-3} mm^2 (3.85×10^{-4} in.^{2}). Using the median value of 27 N (6 lbs) and an instantaneous tension fractional loss of 50%, the winding tension in the layers is computed to be 54 MPa (7.9 kpsi).

The winding time was not given but assumed to be 600 seconds for each helical layer and 200 seconds for each hoop layer. The knowledge of the actual winding time is not crucial in the analysis since there is very little fiber motion due to the high material viscosity at ambient temperature.

The cure cycle for the 976 resin system is a one-step heat up from the ambient temperature of 21 °C (70 °F) to a cure temperature of 177 °C (350 °F), which is then sustained for a duration of 4 hours.

At the end of heatup, the mandrel is removed from the structure, leaving the rubber layer and the composite shell as the finished structure.

7.2.2 Finite Element Model

The finite element model of the filament wound bottle is shown in Fig. 41. complete with composite layers, mandrel, rubber insulation, and polar boss. The finite element model utilized plane symmetry; and therefore, only the upper half of the bottle was modeled. A total of 1431 nodes and 1275 elements were used in the model. Three element layers were used to model the mandrel, one was used for the rubber insulation, and six were used for the composite shell. Since there are only four composite layers in the dome section, the first two element layers in the dome represent the first helical layer. Similarly, the last two element layers in the dome represent the fourth helical layer. Figure 42 is a close up view of the finite element model, showing the transition from the cylindrical section to the dome section.

The boundary conditions imposed on the finite element model are the restriction of the nodes on the plane of symmetry from displacements in the z direction to preserve symmetry.

The curing stage was divided into 8 steps, with 7 heatup steps and a cooldown step. The heatup steps are of durations of 20, 20, 16, 24, 20, 80, and 60 minutes. The smaller times steps were used for better approximation of the viscosity variations in that region. The thermo-kinetic data in the heatup steps were obtained from the thermo-kinetic model by Loos et al. [16].

The analysis were carried out for two different mandrel materials: a soft sand/PVA mandrel and a stiffer steel mandrel. The material properties used in the analysis are listed in Table 4.

Again, the analysis was carried out with the equilibrium iteration flag set to 3, resulting in the activation of the iteration in every load step.

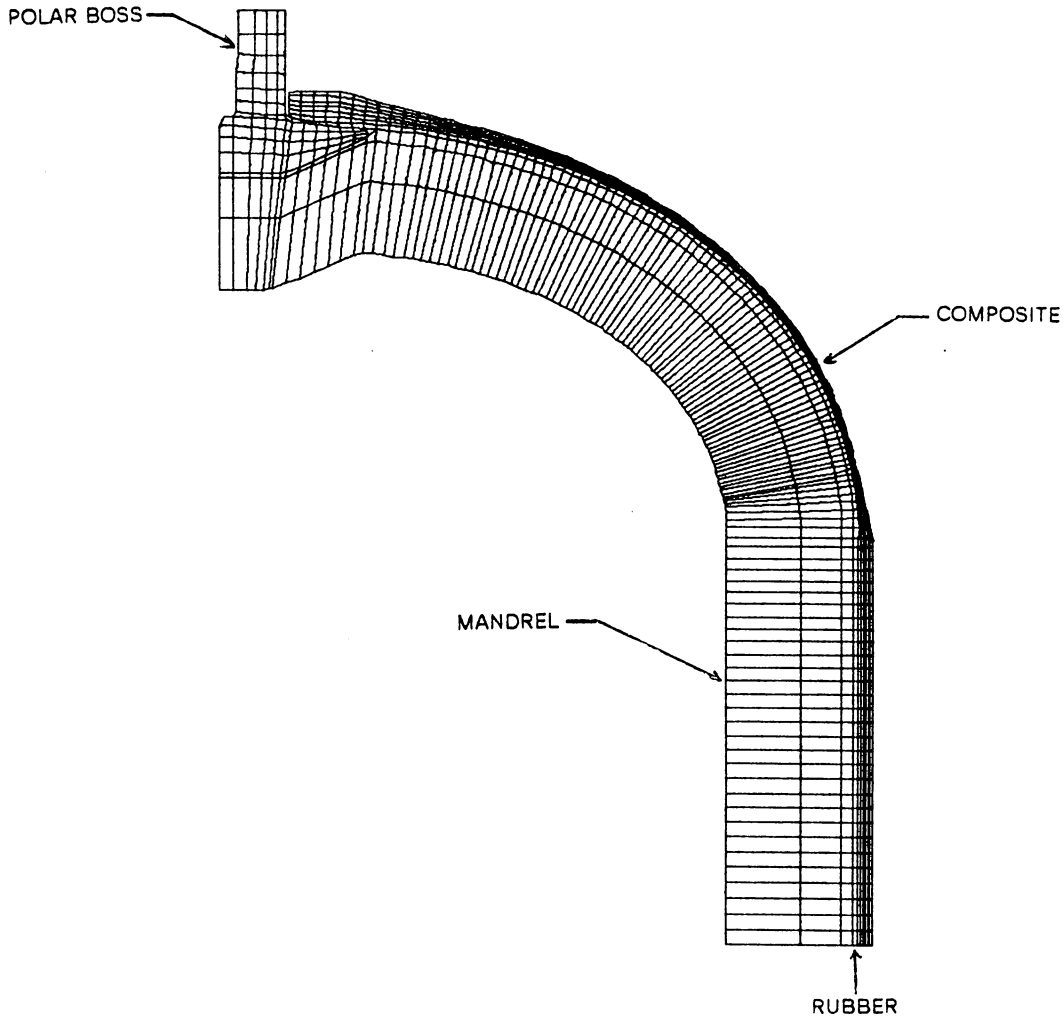

Figure 41. Finite Element Model of the Filament Wound Bottle

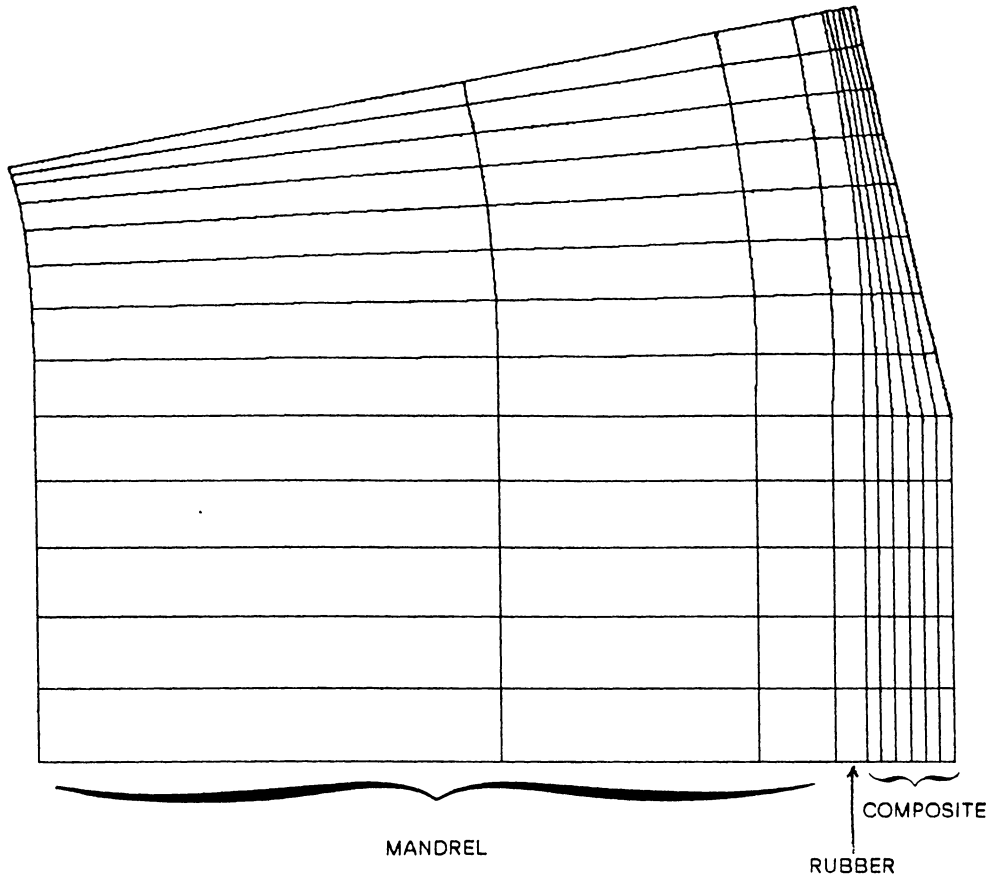

Figure 42. Close Up View of the Cylinder-Dome Intersection

Table 4. Material Properties for Composite Bottle Analysis

T300/976 COMPOSITE MATERIAL:			
E_1	=	129 GPa	(1.87×10^7 psi)
E_2 (uncured)	=	3.86 GPa	(5.60×10^5 psi)
E_2 (cured)	=	7.42 GPa	(1.12×10^6 psi)
E_3 (uncured)	=	3.86 GPa	(5.60×10^5 psi)
E_3 (cured)	=	7.42 GPa	(1.12×10^6 psi)
ν_{23}	=	0.3000	
ν_{31} (uncured)	=	0.0085	
ν_{31} (cured)	=	0.0161	
ν_{21} (uncured)	=	0.0085	
ν_{21} (cured)	=	0.0161	
G_{12} (uncured)	=	0.503 GPa	(7.30×10^4 psi)
G_{12} (cured)	=	5.03 GPa	(7.30×10^5 psi)
α_1	=	-7.74×10^{-7} / °C	(-4.30×10^{-7} / °F)
α_2	=	2.45×10^{-5} / °C	(1.36×10^{-5} / °F)
α_3	=	2.45×10^{-5} / °C	(1.36×10^{-5} / °F)
Fiber Modulus	=	215 GPa	(3.12×10^7 psi)
Fiber Radius	=	3.0×10^{-3} mm	(1.18×10^{-4} in.)
Fiber Volume	=	0.60	
Viscosity (at 21 °C or 70 °F)	=	0.6805 Pa-sec.	(9.867×10^{-4} psi-sec.)
POLAR BOSS (steel):			
E	=	200 GPa	(2.90×10^7 psi)
ν	=	0.32	
α	=	1.17×10^{-5} / °C	(6.50×10^{-6} / °F)
SAND/PVA (mandrel):			
E	=	6.03 MPa	(8.75×10^2 psi)
ν	=	0.3000	
α	=	-5.58×10^{-6} / °C	(-3.10×10^{-6} / °F)
RUBBER (insulator):			
E	=	3.10 MPa	(4.50×10^2 psi)
ν	=	0.4900	
α	=	1.62×10^{-4} / °C	(9.00×10^{-5} / °F)

7.2.3 Results and Discussions

The fiber stresses obtained from the analysis of the sand/PVA mandrel are shown in Figs. 43 to 46 for the end of winding, heating, cooling, and mandrel removal, respectively. In these figures, the fiber stresses are plotted as functions of the element sections, starting from the line of symmetry and going to the polar boss. The vertical lines in the figures represent the intersection of the cylindrical region with the dome region. Notice that there are six separate stress curves in the cylindrical region. However, two of these curves merge into others in the dome section. This merging of the curves is consistent with the fact that only four composite layers are present in the dome section.

There is a lot of tension loss in the composite shell after winding due to the softness of the sand/PVA mandrel. In fact, the first two layers are driven into complete compression, except near the polar boss. A stress discontinuity is observed in two of the curves, near the intersection of the cylindrical region and the dome region. These two curves represent the hoop layers. The stress discontinuity is best explained by the fact that the hoop layers terminate right at the intersection, creating a geometrical discontinuity in the structure, which in turns causes the discontinuity in the fiber stresses. Also, the stress curves show singular behavior at the polar boss end. This singular behavior could be due to both the presence of a free edge at the polar boss and the large variations in the wrap angles in this region.

After heating, the composite layers gain little tension because of the negative thermal expansion coefficient of sand/PVA mandrel and the low thermal expansion coefficient of the composite. Notice in Fig. 44 that the first (innermost) layer stays at the same tension level as after winding, indicating that the shrinkage of the mandrel

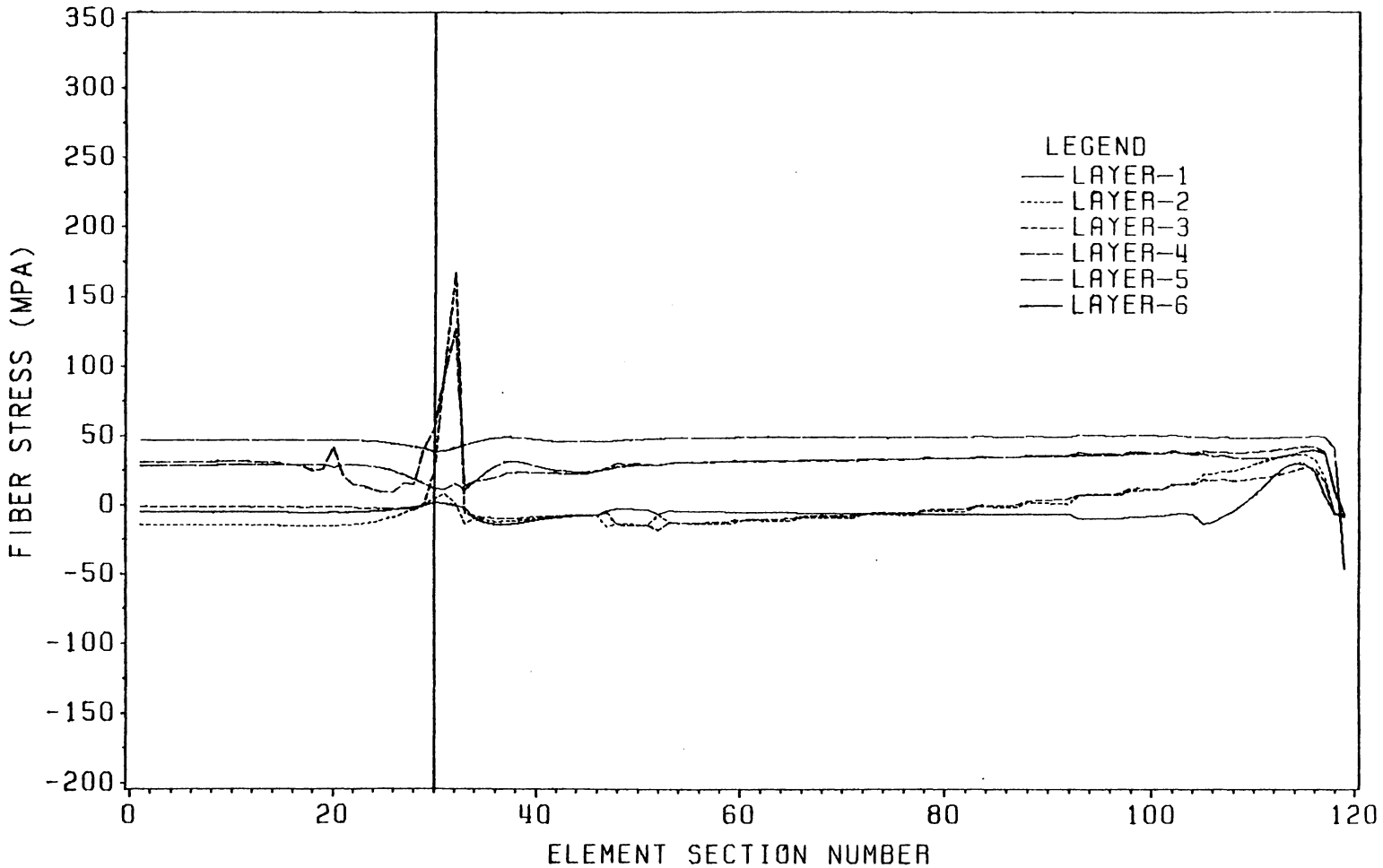

Figure 43. Fiber Stresses in Sand/PVA Mandrel Case after Winding

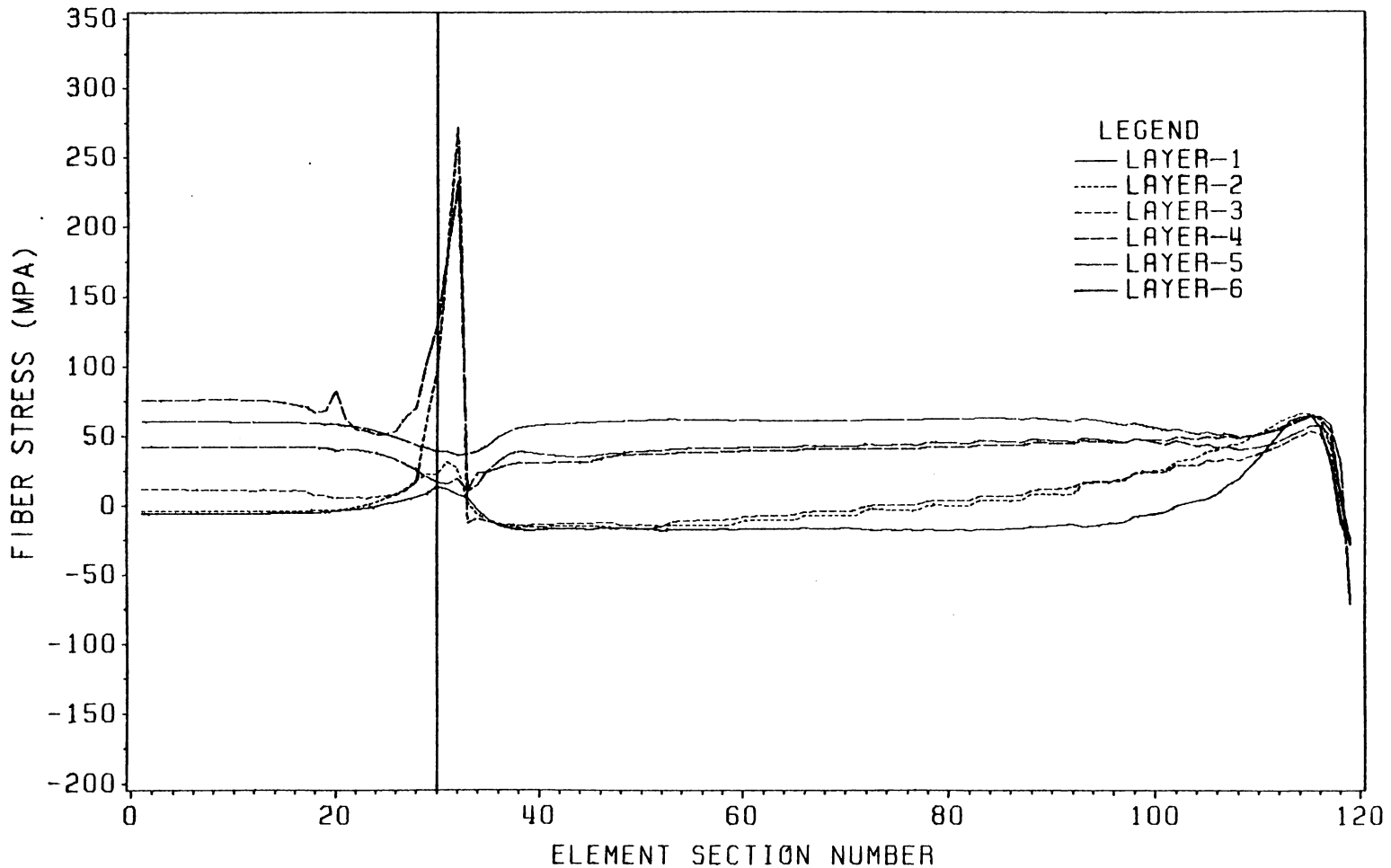

Figure 44. Fiber Stresses in Sand/PVA Mandrel Case after Heating

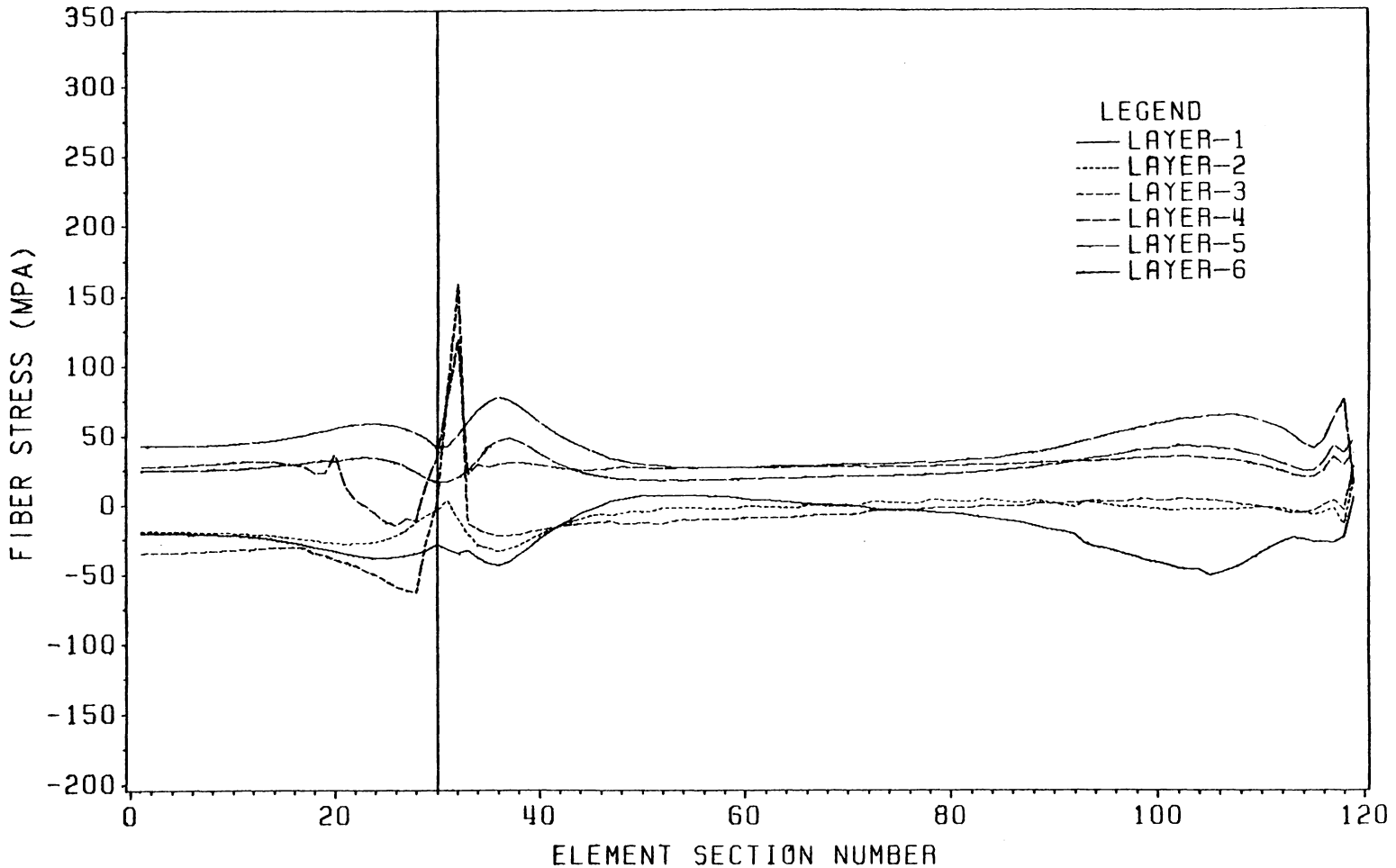

Figure 45. Fiber Stresses in Sand/PVA Mandrel Case after Cooling

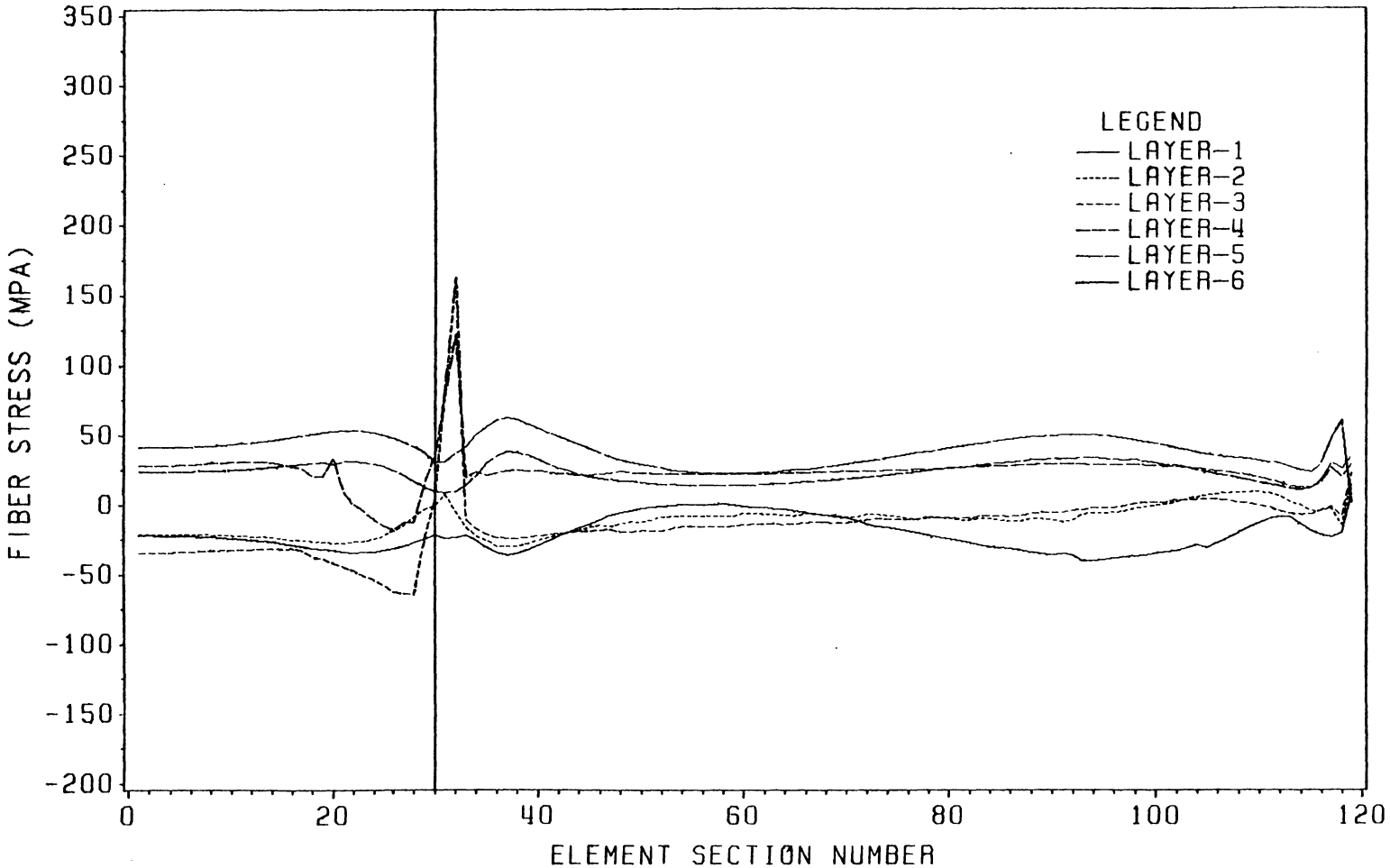

Figure 46. Fiber Stresses in Sand/PVA Mandrel Case after Mandrel Removal

and the expansion of the rubber insulation cancel each other out completely (rubber has a very high coefficient of thermal expansion). The other layers, however, gain a little tension due to the radial expansion of the composite layers themselves. Thanks to this radial expansion, the second layer is driven back partly into tension in the dome section. In the cylindrical section, the second layer also gains tension but not enough to bring it to the tensile side. Finally, the stress discontinuity and singularity seen after winding become even more pronounced after heating.

After cooling, the stress curves come closer together. Again, the first layer stays at the same tension level. The fiber stress in the second layer in the dome section, having become tensile after heating, remains tensile at the end of cooling. Also, the stress discontinuity and singularity become less pronounced due to shrinkage of the composite.

The stress curves in the composite after the removal of the mandrel are almost identical to those after winding, indicating a very low stress level in the sand mandrel, not enough to have any significant effect on the composite when the mandrel is removed. These stress curves also represent the fiber direction component of the residual fabrication stresses in the composite wall of the bottle. Figure 46 shows a fairly wide distribution of the residual stresses with an average range of about 60 MPa (8.7 kpsi), centered about the zero line. The highest tensile residual fiber stress is 163 MPa (23.6 kpsi) at the stress discontinuity.

The stress plots in Figs. 43 to 46 show that the sand/PVA mandrel has little effect on the stress states in the composite layers. Instead, the fiber stresses are almost exclusively determined by the behavior of the composite itself. In other words, in the sand/PVA mandrel case, the composite shell is the primary influence on the fiber stresses. As a result, any geometrical discontinuity in the composite shell would cause very pronounced discontinuities in the fiber stresses, as shown in the figures.

Figure 47 shows the fiber strains in the layers at cure in the sand mandrel case. The figure shows that all layers except the innermost layer and part of the second layer, near the cylinder-dome intersection, are cured in a state of tensile strain. The innermost layer, however, is cured with very large compressive strains implicating a high possibility of strength loss in this layer due to local fiber buckling resulting from the compressive strain. The radial stresses in the layers need not be examined for possible composite-mandrel separation since the mandrel is already removed.

The fiber stresses for the steel mandrel case are shown in Figs. 48 to 51 for the end of winding, heating, cooling, and mandrel removal, respectively. Again, the vertical line in the figures indicates the intersection of the cylindrical region with the dome region.

After winding, the composite layers have lost very little tension and none of the layers is in compression. Whatever little tension losses in the layer are due to the presence of the soft rubber insulation. As a result, the stress curves are very close to each other. Notice that there is actually a tension gain in part of the innermost layer, near the intersection. This phenomenon can be explained by the presence of the rubber layer. When the hoop layers are wound in the cylindrical section, their high stiffnesses generate a very large shrinkage in the layers underneath. The steel mandrel, being very stiff, shrinks very little. Therefore, the soft rubber layer experiences a large compression in the cylindrical region between the high stiffnesses of the hoop layers and the steel mandrel. Due to the incompressible nature of rubber, the 'compressed' material is actually displaced elsewhere, and the only place to displace to is in the dome section where there are no hoop layers. This displacement of the rubber material generates a bulge in the dome section near the intersection which drives the innermost layer into higher tension. This effect is not propagated to the second layer because of the relatively high stiffness of the composite layers.

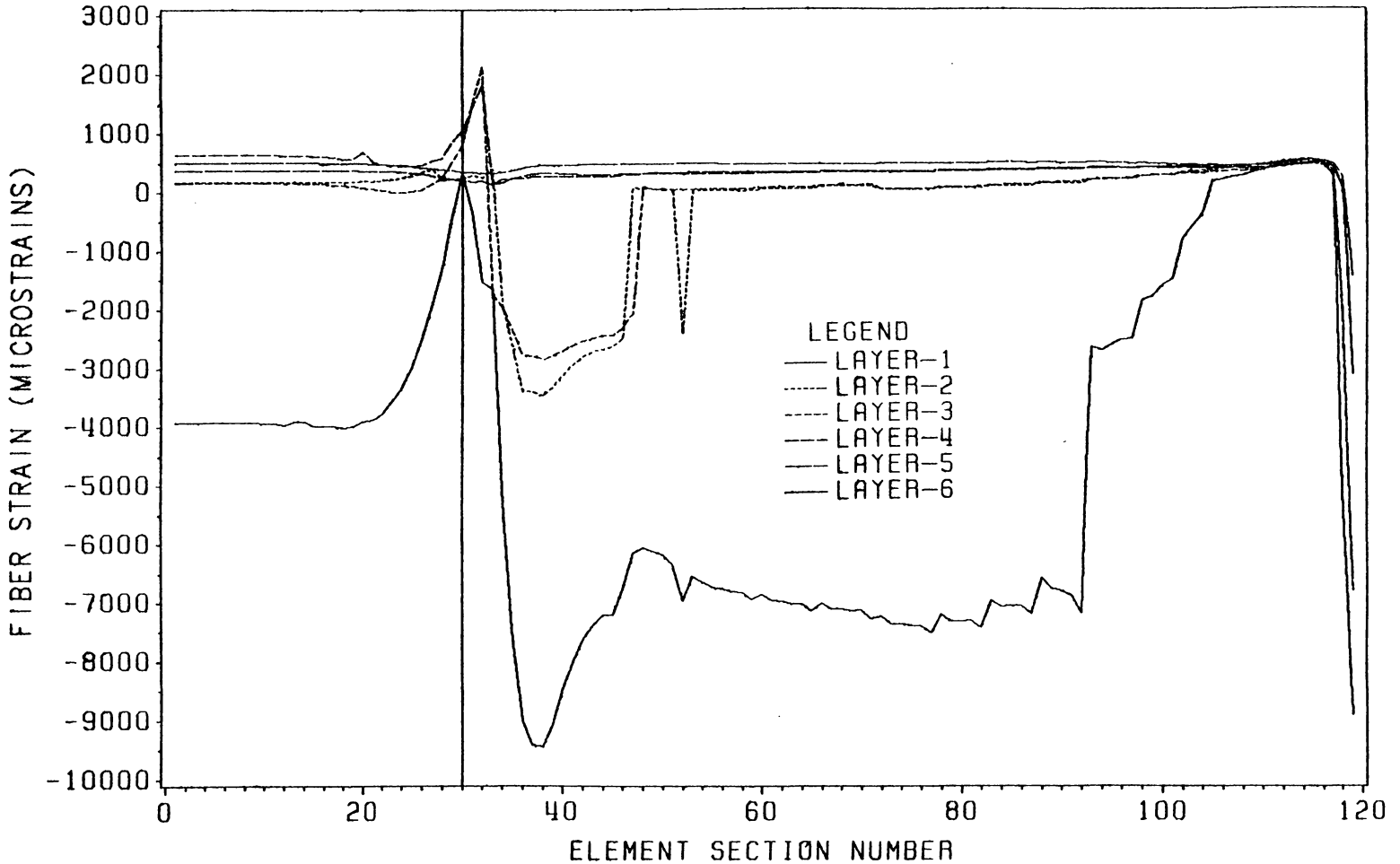

Figure 47. Fiber Strains at Cure in Sand/PVA Mandrel Case

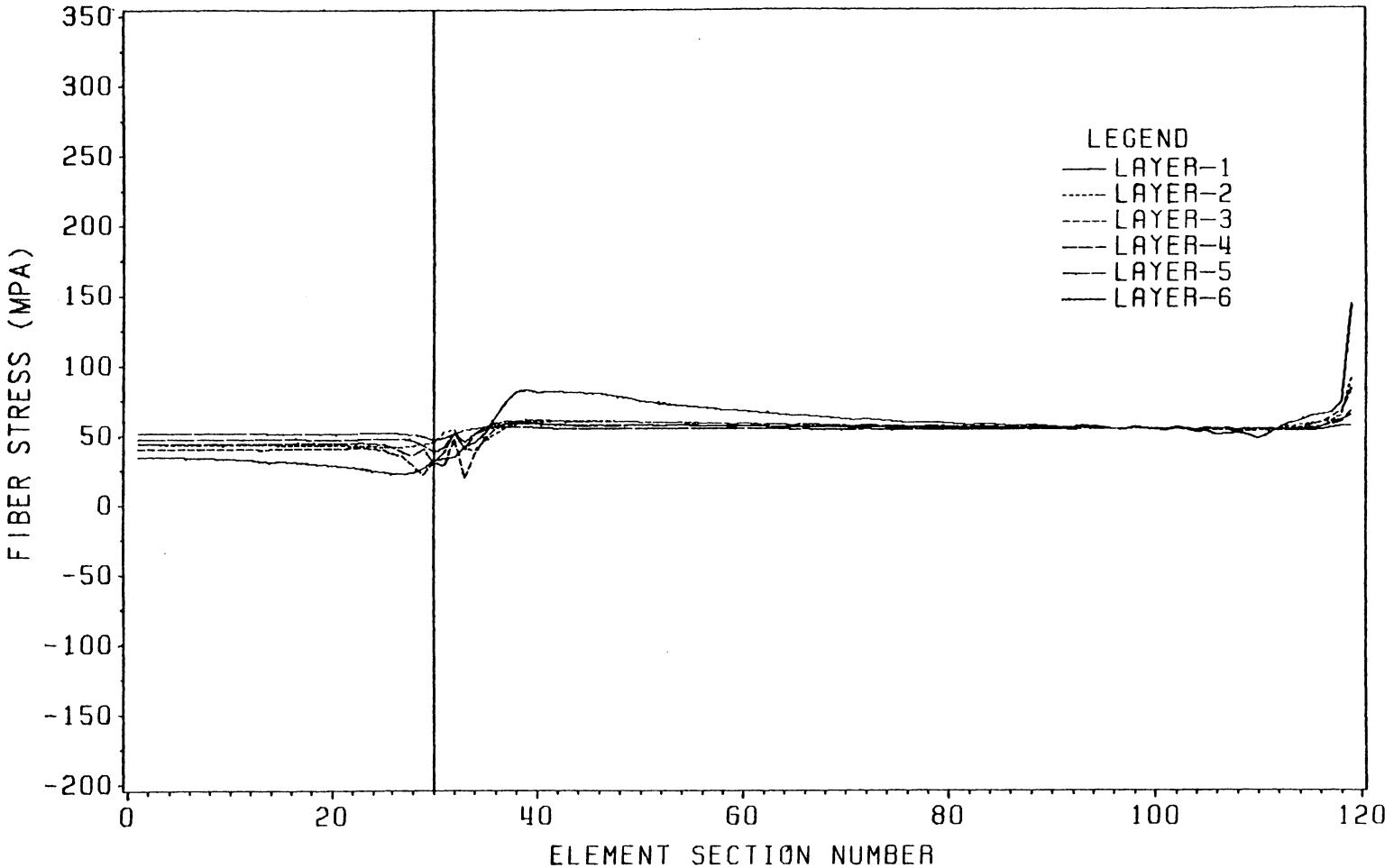

Figure 48. Fiber Stresses in Steel Mandrel Case after Winding

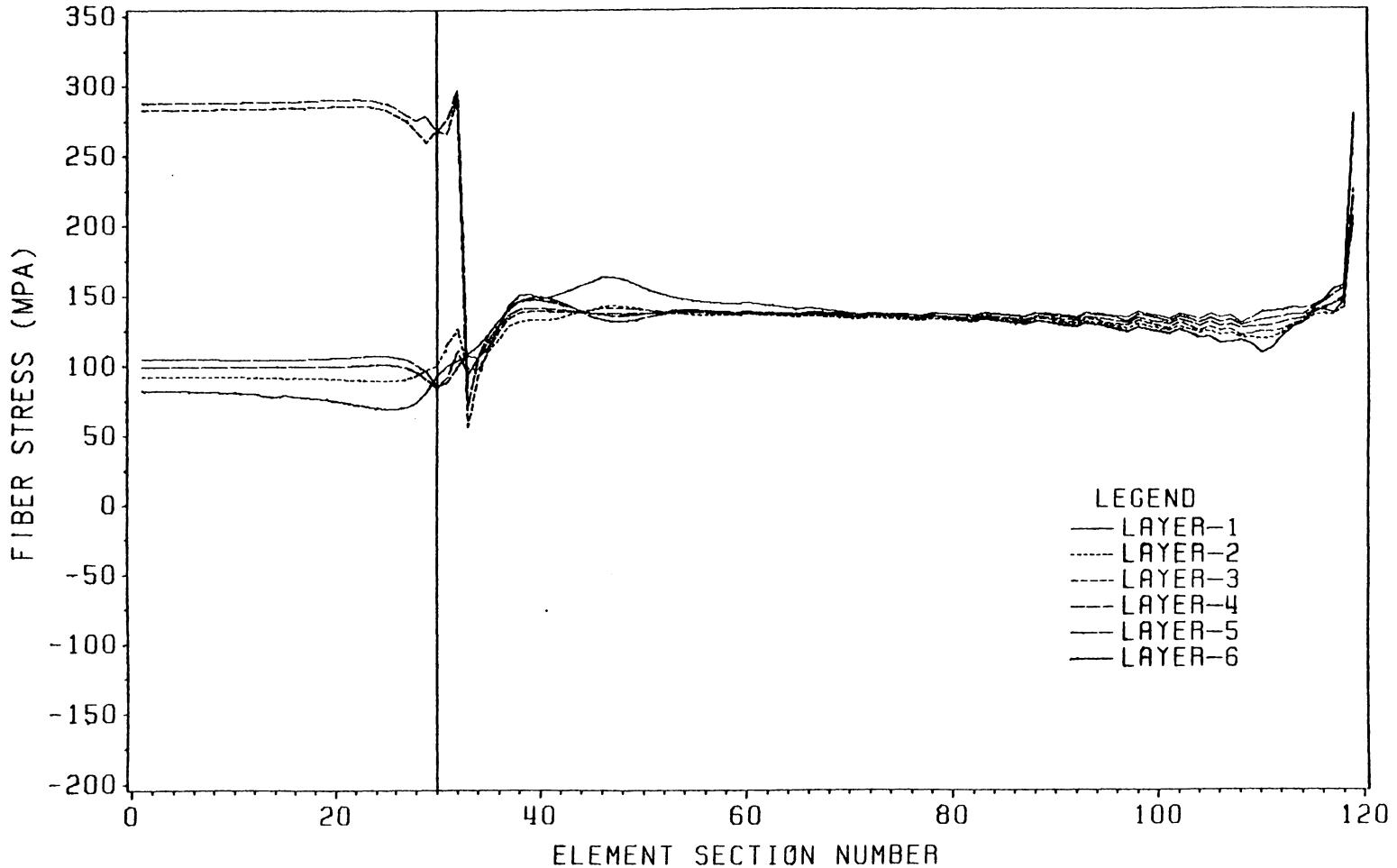

Figure 49. Fiber Stresses in Steel Mandrel Case after Heating

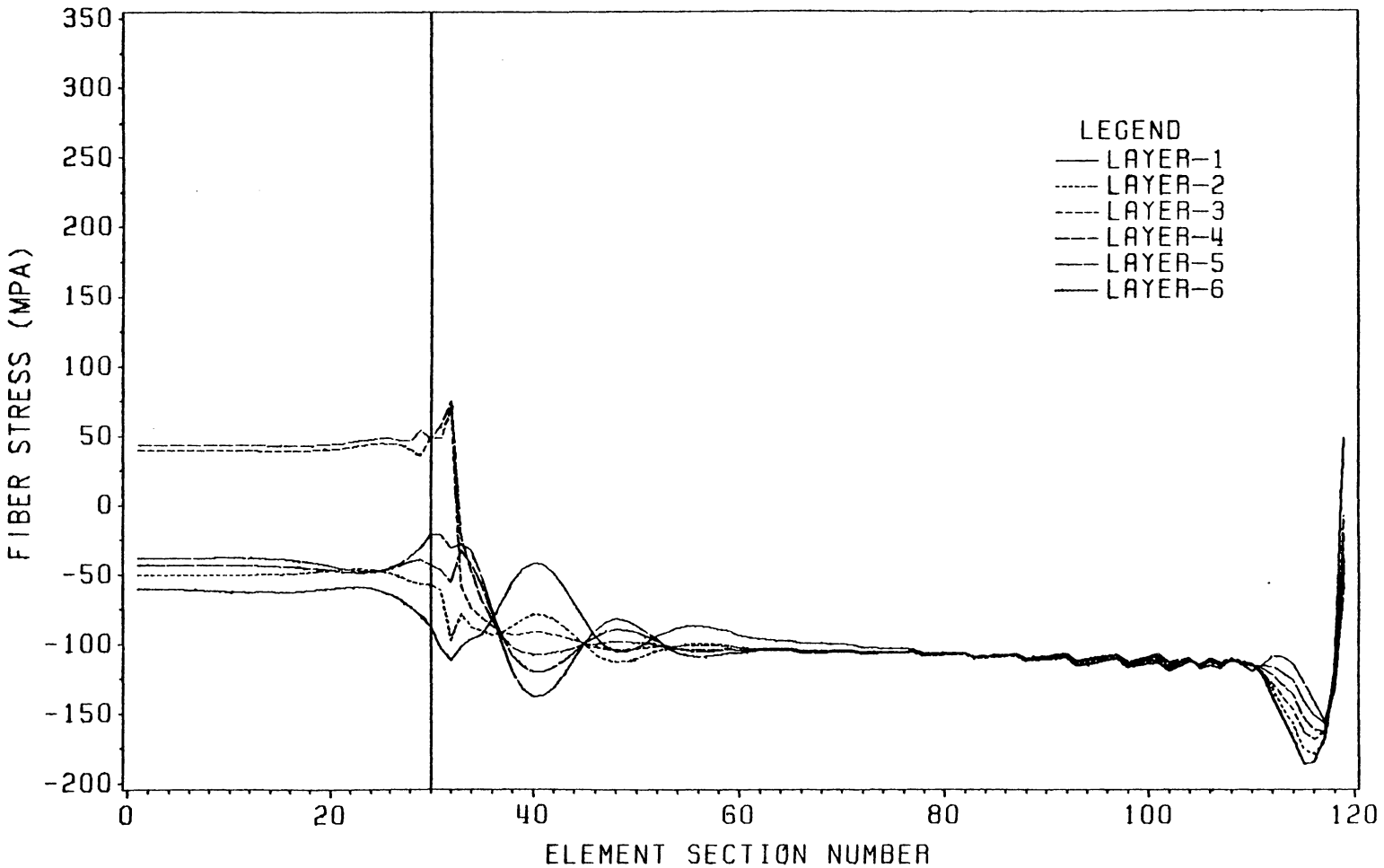

Figure 50. Fiber Stresses in Steel Mandrel Case after Cooling

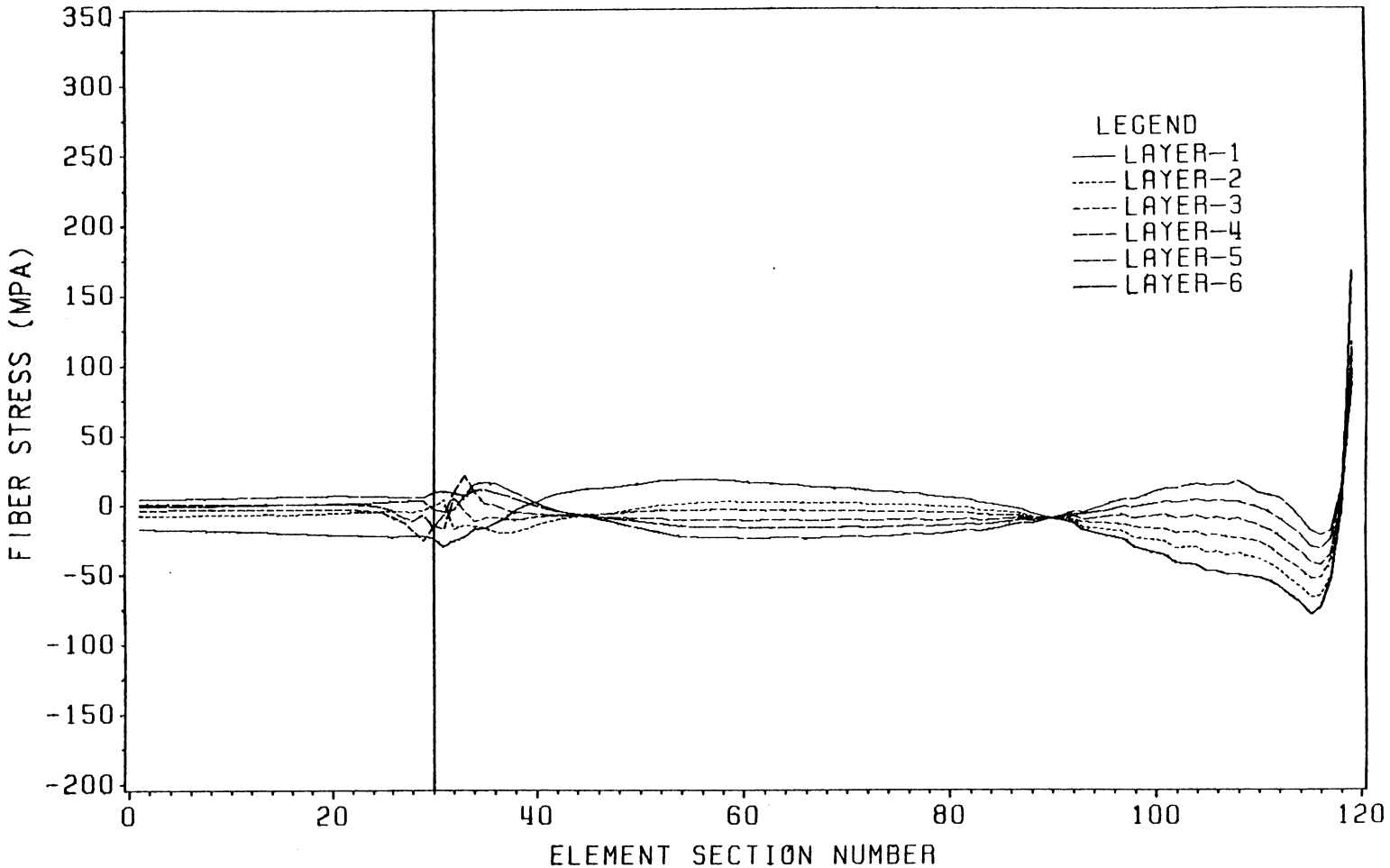

Figure 51. Fiber Stresses in Steel Mandrel Case after Mandrel Removal

This phenomenon did not occur in the sand mandrel because the low stiffness of the sand mandrel cannot generate enough pressure to sustain a compression of the rubber layer in the cylindrical region. Notice that the stress discontinuity near the cylinder-dome intersection is still present but barely noticeable. The small magnitude of the stress discontinuity in the steel mandrel case is a direct result of the high stiffness in the mandrel which makes it the dominant influence of the fiber stresses. Since there is no geometrical discontinuity in the mandrel, the fiber stresses should not exhibit any pronounced discontinuities. The singular behavior in the stress curves at the polar boss is still visible, however.

At the end of heating, all layers are driven into higher tension, especially the hoop layers, which have higher stiffnesses than the helical layers. Also, all helical layers gain about the same amount of tension, indicating that the expansion of the steel mandrel is a much larger influence than the expansion of the composite layers.

After cooling, all helical layers are shown to be in compression in Fig. 50. These compressive stresses in the layers are caused by the shrinkage of the mandrel which also pulls the composite layers along in the finite element model. In the actual case, however, the mandrel cannot pull the composite layers in that much because the bonding between the mandrel and the composite is very weak. Instead, there would be a composite-mandrel separation during cooling. The fabrication stress model, having no gap element, cannot model this behavior. Therefore, the stresses in Fig. 50 are not indicative of the real behavior of the composite after cooling. Instead, the stress curves at the end of mandrel removal in Fig. 51 represent more accurately the actual fiber stresses after cooling (and also after mandrel removal).

As in the case of the sand/PVA mandrel, the fiber direction residual stresses (after mandrel removal) in Fig. 51 are centered about the zero line. The average range of the stress curves is only about 25 MPa (3.6 kpsi), which is less than half of

the range in the sand/PVA mandrel case. The highest tensile residual fiber stress is at the stress singularity at the polar boss and has a value of 167 MPa (24.2 kpsi), or only 4 MPa (0.58 kpsi) higher than the highest value in the sand/PVA mandrel case.

The stress plots in Figs. 48 to 51 show that the steel mandrel is the major factor influencing the fiber stresses in all stages of fabrication. The retention of fiber tension after winding and the large gain in fiber tension after heating are both due to the high stiffness and high coefficient of thermal expansion of the mandrel.

The fiber strains at cure of the steel mandrel case are plotted in Fig. 52. As can be seen in the figure, all layers are cured in a state of tensile strain, implicating that there should be no strength degradation in the finished structure due to local fiber buckling. The only possible source of tension loss is the high fiber stresses at the end of heating which may cause breakage of the fibers. However, the tensile strength for the T300 graphite fibers is 3.31 GPa (480 kpsi), much higher than the maximum tension in the fibers at the end of heating. Therefore, there should be no degradation of strength in the final structure if the steel mandrel is used.

In summary, the low stiffness of the sand/PVA mandrel causes large tension losses in the fibers after winding. In the heating, cooling, and mandrel removal stages, the low stiffness and negative coefficient of thermal expansion of the sand/PVA mandrel, cancelled by the presence of the rubber insulation have insignificant effect on the fiber stresses. As a result, the fibers in the first layer are cured under large compressive strains, resulting in a high possibility of strength loss in the finished structure. On the other hand, the high stiffness of the steel mandrel prevents tension loss in the fibers after winding. Furthermore, the high coefficient of thermal expansion of steel generates large expansion of the mandrel in the heatup step which drives the fibers into further tension. As a result, the fibers are cured under a state of tensile strain, implicating no possibility of strength loss due to local fiber buckling.

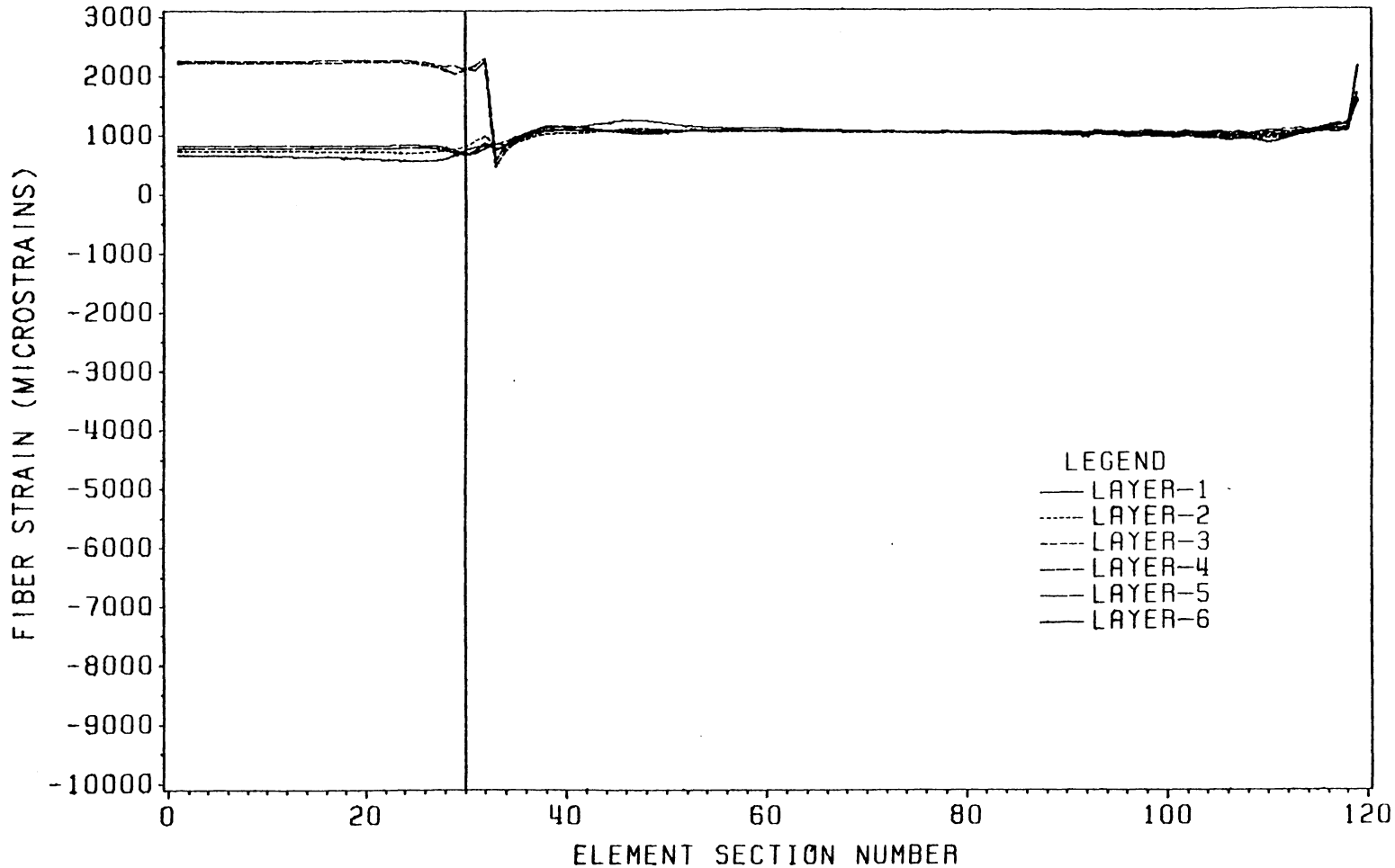

Figure 52. Fiber Strains at Cure in Steel Mandrel Case

Also, a lower scatter in the residual stresses in the steel mandrel case indicates that, in the average sense, the finished bottle can withstand higher internal pressure. Pointwise, the maximum residual fiber stress in the steel mandrel case is only 4 MPa (5.1 kpsi) higher than that in the sand/PVA mandrel case while the strength of the latter case must be significantly degraded. The bottle fabricated with the steel mandrel should be able to withstand higher internal pressure.

Chapter 8

Conclusions and Recommendations

8.1 Conclusions

Two main conclusions can be drawn from the case studies in the previous chapter: the fabrication stress model yields accurate results for both the winding and the curing stages, and the results obtained from the fabrication stress model can be used to predict the performance of the composite structure.

The WACSAFE hoop strain result from the overwrap case study shows excellent agreement with experimental data for the winding stage, with the largest difference with either experimental data set of 80 μin./in. out of 768 μ in./in., or about 11%. The hoop strain result from the curing stage of the same case study shows the same behavior as experimental data, with the exception of lower tension loss due to fiber motion near the beginning of the curing stage. This lower tension loss, however, is expected since the 976 resin's viscosity data used in the analysis is known to be

higher than that of the 982 resin used in the actual overwrap. Furthermore, the stress results from the analysis show very reasonable and expected behaviors.

The filament wound bottle case study also shows that the fabrication stress model yields reasonable, expected, and explicable results for all three stages of fabrication of a typical filament wound structure. The results from the sand/PVA mandrel case and the steel mandrel case show similarities and contrasts that are intuitively correct. Among the the similarities are the stress discontinuity near the cylinder-dome interface and the stress concentration at the polar boss. Among the well expected contrasts are the higher tension levels in the steel mandrel case before mandrel removal, the greater influence of the steel mandrel on the fiber stresses, and smaller range of the stress distribution after mandrel removal.

The fabrication stresses and strains can be used to predict the qualitative strength performance of the structure. In particular, the fiber strains at cure were used to predict possible strength degradation in the final structure due to local fiber buckling or wrinkling at cure. The positive fiber strains at cure in the overwrap case study and in the steel mandrel bottle case study showed that there should be no strength degradation due to local fiber buckling. On the other hand, compressive fiber strains in the sand/PVA mandrel case study implies possible strength reduction in the bottle.

The residual radial stresses were also used to predict the possibility of delamination or composite-mandrel separation in the overwrap case study, where the mandrel is part of the final structure. The compressive residual radial stress implies that there should be no delamination or composite-mandrel separation.

In summary, the fabrication stress model can indeed be used as a tool for the qualitative prediction of performance of the final product from the fabrication process

variables. Consequently, it can also serve as a tool for the evaluation and comparison of fabrication process designs.

8.2 Recommendations

The accuracy of the fabrication stress model can be further improved by improving the accuracy of the models discussed in this dissertation and by incorporating into the stress model other phenomena not considered in the dissertation. Towards this end, the following recommendations are made for future research:

1. Conduct a winding experiment of a single fiber band on mandrels of various sizes and stiffnesses to determine the correct amounts of instantaneous strength loss for the composite materials used in the analyses of the case studies. Also, a multiple circuit winding experiment can be carried out to determine experimentally the amount of tension loss due to multiple circuit winding. The results from such an experiment will serve to verify the multiple circuit winding study presented in this dissertation and perhaps will enable the selection of a more accurate stiffness reduction factor.

2. Model the possible composite-mandrel separation during fabrication by implementing gap elements and geometrical nonlinearity iterations in WACSAFE.

3. Take into account the variation of the 3 direction properties of the composite material such as the modulus of elasticity and the coefficient of thermal expansion, as pointed out by Tarnopol'skii and Beil' [7]. One suggested solution to the

modeling of this phenomenon is the implementation of some mathematical model for these quantities as functions of temperature, and possibly stress level. The mathematical model of such quantities will have to be constructed for each material system and can be interfaced with WACSAFE as a subroutine. Such a functionalization of the material properties would also enable the implementation of an equilibrium iteration for material nonlinearity in the curing process.

4. Interface WACSAFE with the thermo-kinetic model so that both models can be run as a single program. This interface would allow WACSAFE direct access to the inter-dependent 2-D fiber motion and thermo-kinetic models. The interface of the models would also allow the influence of the fiber stresses directly on the 2-D fiber motion model, and also indirectly on the thermo-kinetic model through the fiber motion model. Such an interface would allow a more accurate representation of the actual fabrication process.

5. Incorporate interactive pre- and post-processing capability into WACSAFE. At the time of the conclusion of this dissertation, WACSAFE still has very rudimentary pre-processing capabilities which are limited to linear generation of nodes and elements, and mandrel element generation for a TASS finite element mesh. Furthermore, WACSAFE has virtually no post-processing capabilities. It is therefore recommended that a pre- and post-processor is interfaced with WACSAFE to facilitate mesh generation and stress and strain extractions. This pre- and post-processor can be made menu-driven to facilitate the use of WACSAFE.

References

1. Chen, M. C., and Clewlow, L. N. O., "Computer Analysis of Filament-Reinforced Metallic-Spherical Pressure Vessels," *Computers and Structures*, Vol. 7, pp. 93-102, 1977.

2. Gerstle, F. P., Jr., "Analysis of Filament Wound Spherical Pressure Vessels," *Composite Materials: Testing and Design, Third Conference* , ASTM STP 546, 1973.

3. Patel, H. P., and Kennedy, R. H., "Nonlinear Finite Element Analysis for Composite Structures of Axisymmetric Geometry and Loading," *Computer and Structures*, Vol. 15, No. 1, pp. 79-84, 1982.

4. Knight, C. E., "Analytical Failure Prediction of Spherical Composite Pressure Vessels," *ASME Journal of Pressure Vessel Technology*, Vol. 104, pp. 229-231, August 1982.

5. Leavesley, P. J., and Knight, C. E., "An Analytical Model of Strength Loss in Filament Wound Spherical Vessels," *ASME Journal of Pressure Vessel Technology*, Vol. 109, pp. 352-356, August 1987.

6. Johnson, J. C., and Knight, C. E., "Winding and Curing Stress Analysis of Filament Wound Composites by Finite Elements," Technical Report, Morton Thiokol, Inc., WASATCH Division, May 1986.

7. Tarnopol'skii, Y. M., and Beil', A. I., "Problems of the Mechanics of Composite Winding," *Handbood of Composites*, Vol. 4, pp. 45-108, 1983.

8. Clough, R. W., and Woodward, R. J., III, "Analysis of Embankment Stresses and Deformations," *Journal of the Soil Mechanical and Foundations Division*, ASCE, Vol. 93, pp. 529-549, July 1967.

9. Brown, C. P., and King, I. P., "Automatic Embankment Analysis: Equilibrium and Instability Conditions," *Geotechnique*, Vol. 16, No. 3, pp. 209-219, 1966.

10. Duncan, J. M., and Clough, G. W., "Finite Element Analysis of Port Allen Lock," *Journal of the Solid Mechanics and Foundations*, ASCE, Vol. 97, pp. 1053-1066, 1971.

11. Duncan, J. M., and Dunlop, P., "Slopes in Stiff-Fissured Clays and Shales," *Journal of the Soil Mechanics and Foundations*, ASCE, Vol. 95, No SM2, pp. 467-492, 1969.

12. Christian, J. T., and Wong, I. H., "Errors in Simulating Excavation in Elastic Media by Finite Elements," *Soils and Foundations*, Vol. 13, No. 1, pp. 1-10, March 1983.

13. Ishihara, K., "Relations between Process of Cutting and Uniqueness of Solutions," *Soils and Foundations*, Vol. 10, No. 3, pp. 50-65, 1970.

14. Ghaboussi, J., and Pecknold, D. A., "Incremental Finite Element Analysis of Geomtrically Altered Structures," *International Journal for Numerical Methods in Engineering*, Vol. 20, pp. 2051-2064, 1984.

15. Chandrasekaran, V. S., and King, G. J. W., "Simulation of Excavation Using Finite Elements," *Journal of the Geotechnical Engineering Division*, Vol. 100, No. GT9, pp. 1086-1089, 1974.

16. Loos, A. C., Knight, C. E., Somanath, N., and Tzeng, T. S., "Axisymmetric Cure/Stress Model for Filament Wound Composites, I. Layer Tension Loss and Cure Models," 1987 JANNAF Composite Motor Case Subcommittee Meeting, NASA Langley Research Center, February 23-27, 1987.

17. Zienkiewicz, O. C., *The Finite Element Method*, McGraw-Hill, England, 1977.

18. Cook, R. D., *Concepts and Applications of Finite Element Analysis*, John Wiley and Sons, New York, 1974.

19. Bathe, K. J., *Finite Element Procedures in Engineering Analysis* ,Prentice-Hall, New Jersey, 1982.

20. Reddy, J. N., *An Introduction to the Finite Element Method* , McGraw-Hill, England, 1985.

21. Frederick, D., and Chang, T. S., *Continuum Mechanics*, Scientific Publishers, Inc., Cambridge, 1972.

22. Tsai, S., "Mechanics of Composite Materials Part II - Theoretical Aspects," Technical Report AFML-TR-66-149 Part II, Air Force Materials Laboratory, Wright Patterson Air Force Base, Ohio, 1966.

23. Timoshenko, S., and Goodier. J. N., *Theory of Elasticity*, McGraw-Hill, New York, 1951.

24. Loos, A. C., and Springer, G. S., "Curing of Epoxy Matrix Composites," *Journal of Composite Materials*, Vol. 17, pp. 135-169, 1983.

25. Bathe, K. J., and Wilson, E. L., *Numerical Methods in Finite Element Analysis*, Prentice-Hall, New Jersey, 1976.

26. Nguyen, V. D., Johnson, J. C., and Knight, C. E., *WACSAFE/WACFORM Program User's Guide*, VPI&SU Department of Mechanical Engineering Report, January 1988.

Appendix A

Calculation of Element Thickness and Fiber Path Curvature

The fiber motion model described in this dissertation requires the element thickness and the fiber curvature in the normal direction. The computation of the fiber curvature is done at the center of the element, the radial position of which must also be computed. All three quantities can be computed from the finite element model geometry and winding data. This appendix will describe these computations for both the quadrilateral and the triangular elements.

A.1 Element Center

The radial coordinate of the element center is easily computed from simple geometrical considerations. The locations of the element centers for the quadrilateral and triangular elements are shown in Fig. 53. For the quadrilateral element, the radial coordinate of the element center is simply computed as the average of the radial coordinates of the nodes:

$$r_c = \frac{r_1 + r_2 + r_3 + r_4}{4} \qquad (a.1.1)$$

For the triangular element, the element center is the intersection of two bisectors, shown as lines $3 - m$ and $1 - n$ in Fig. 53. The equations for these two straight lines can be written in linear form as:

$$\begin{aligned} z &= ar + b \\ z &= cr + d \end{aligned} \qquad (a.1.2)$$

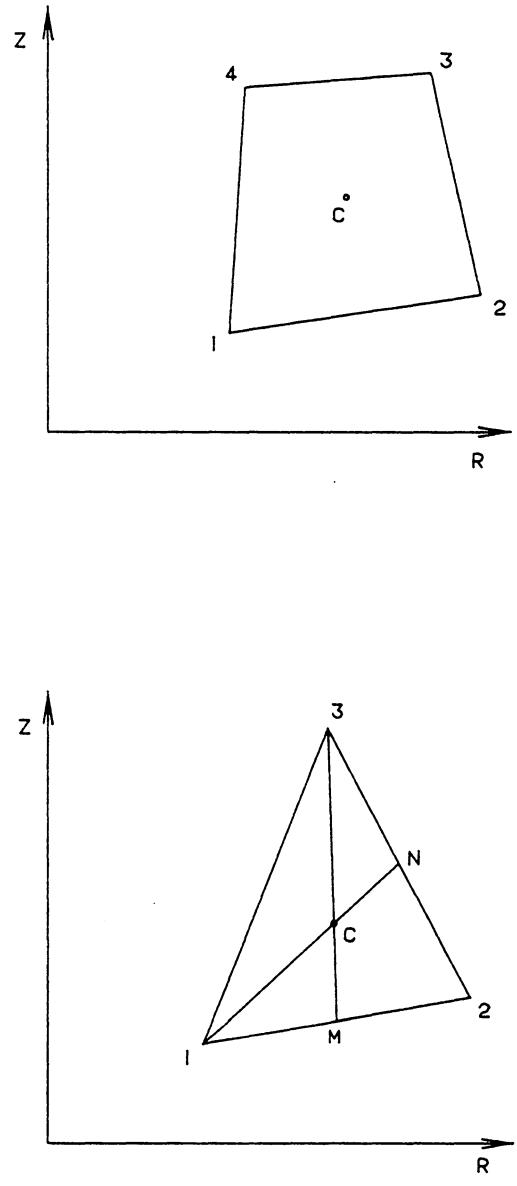

Figure 53. Location of Element Center

The intersection of these two straight lines is the element center, and its radial coordinate is computed by equating the z coordinates of the lines and solving for the r coordinate:

$$r_c = \frac{d-b}{a-c} \tag{a.1.3}$$

The coefficients in equation (a.1.3) are computed by substituting the coordinates of the end points into equations (a.1.2) and solving the equations simultaneously:

$$\begin{aligned} a &= \frac{z_n - z_1}{r_n - r_1} \\ b &= z_1 - ar_2 \\ c &= \frac{z_m - z_3}{r_m - r_3} \\ d &= y_3 - cr_3 \end{aligned} \tag{a.1.4}$$

where

$$\begin{aligned} r_m &= \frac{r_1 + r_2}{2}, \qquad z_m = \frac{z_1 + z_2}{2} \\ r_n &= \frac{r_2 + r_3}{2}, \qquad z_n = \frac{z_2 + z_3}{2} \end{aligned} \tag{a.1.5}$$

A.2 Element Thickness

The element thickness in the normal direction is computed from the nodal coordinates and the direction of the normal vector. The computation is done by projecting the sides of the element onto the normal vector as shown in Fig. 54. For the

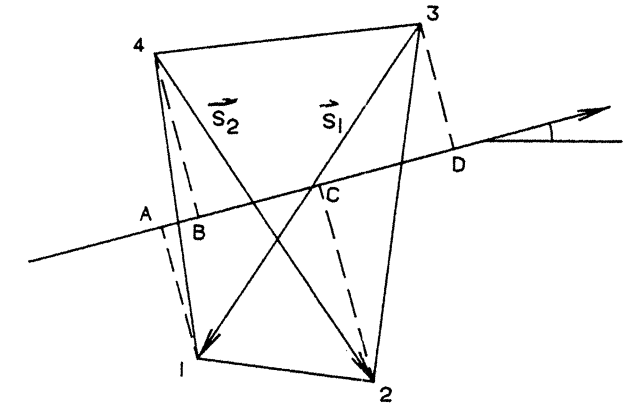

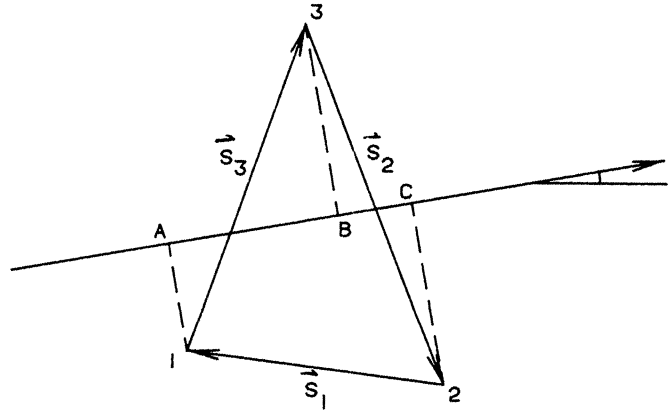

Figure 54. Computation of Element Thickness

quadrilateral element, the element thickness is simply the average of the thickness of the two ends:

$$t = \frac{BD + AC}{2} = \frac{(BC + CD) + (AD - CD)}{2} = \frac{BC + AD}{2} \qquad (a.2.1)$$

Thus, the element thickness in the normal direction is equal to the average of the projections of vectors $\vec{s}_1$ and $\vec{s}_2$ on the normal vector. The lengths AD and BC are computed as dot products of the vectors $\vec{s}_1$ and $\vec{s}_2$ with the normal vector $\vec{n}$:

$$\begin{aligned} AD &= |\vec{s}_1 \cdot \vec{n}| = |(r_1 - r_3)\cos\alpha_1 + (z_1 - z_3)\sin\alpha_1| \\ BC &= |\vec{s}_2 \cdot \vec{n}| = |(r_2 - r_4)\cos\alpha_2 + (z_2 - z_4)\sin\alpha_2| \end{aligned} \qquad (a.2.2)$$

where α_i is the angle between the normal vector $\vec{n}$ and the vector $\vec{s}_i$.

For the triangular element, the element thickness in the normal direction is approximated as half of the largest projection of the sides onto the normal vector. The projections of the sides onto the normal vector are written in dot product form as:

$$\begin{aligned} t_1 &= |\vec{s}_1 \cdot \vec{n}| = |(r_1 - r_2)\cos\alpha_1 + (z_1 - z_2)\sin\alpha_1| \\ t_2 &= |\vec{s}_2 \cdot \vec{n}| = |(r_2 - r_3)\cos\alpha_2 + (z_2 - z_3)\sin\alpha_2| \\ t_3 &= |\vec{s}_3 \cdot \vec{n}| = |(r_3 - r_1)\cos\alpha_3 + (z_3 - z_1)\sin\alpha_3| \end{aligned} \qquad (a.2.3)$$

Thus, the element thickness is:

$$t = \frac{\max\ (t_1, t_2, t_3)}{2} \qquad (a.2.4)$$

A.3 Fiber Path Curvature

The fiber path curvature is computed at the center of the element. Each axisymmetric element is considered as a portion of a circular cone with the cone angle being equal to the polar angle, as shown in Fig. 55. The angled solid lines in Fig. 55 are the center lines of the cross-section of the element. These lines, when extended will meet at point *T*, which is the apex of the cone. The fiber path is represented by a plane passing through the origin of the cylindrical coordinate system *rzt*, making an angle with the horizontal plane equal to the wrap angle. The intersection of the plane with the cone will give a conic section in the *xy* coordinate system on the plane. The shape of this intersection curve depends on the relative magnitudes of the wrap angle and the polar angle and can be written in parametric form as:

$$\begin{aligned} x &= x(\xi) \\ y &= y(\xi) \end{aligned} \qquad (a.3.1)$$

Thus, each point on the curve is defined by a position vector:

$$\vec{D} = x(\xi)\hat{i} + y(\xi)\hat{j} \qquad (a.3.2)$$

The curvature of any point on the curve is then given as:

$$\kappa = \frac{|\vec{V} \times \vec{A}|}{|\vec{V}|^3} \qquad (a.3.3)$$

where $\vec{V}$ and $\vec{A}$ are the first and second derivatives of the position vector $\vec{D}$ with respect to the parameter, respectively.

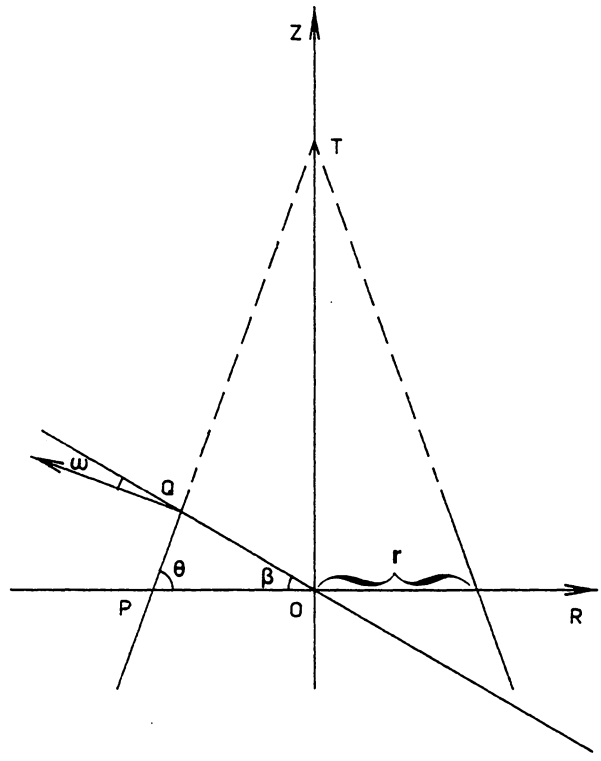

Figure 55. Modeling of the Fiber Path

In Fig. 55, the angle considered is not the polar angle but the angle the side of the cone makes with the horizontal plane. This angle θ is equal to 90° minus the polar angle. Two special cases results from extreme values of this angle θ . When θ is equal to 0°, the cone becomes a circular disk and the curvature of any fiber path on this disk is zero. When θ is equal to 90°, the cone becomes a circular cylinder and the intersection with any plane will result in an ellipse (a circle is a special ellipse). This special case is shown in Fig. 56. The intersection curve is shown in the coordinate system *xy* on the plane. The origin of the *xy* coordinate system coincides with the origin of the cylindrical coordinate system *rzt*. The major axis of the ellipse, *a*, is equal to length *OQ* and the minor axis, *b*, is equal to the radius of the cylinder:

$$a = OQ = \frac{r}{\cos \beta}$$
$$b = r \qquad (a.3.4)$$

The equation for the ellipse can be written in parameterized form as:

$$x = a \cos \alpha$$
$$y = b \sin \alpha \qquad (a.3.5)$$

where α is the angle the position vector makes with the *x* axis. Differentiation and substitution into equation (a.3.3) yields the following formula for curvature:

$$\kappa = \frac{ab}{\left[(-a\sin\alpha)^2 + (b\cos\alpha)^2\right]^{3/2}} \qquad (a.3.6)$$

The curvature at the center of the element is computed at point *M*, where $\alpha = 90°$. Substitution of this value into equation (a.3.6) yields the curvature of the fiber path at the center of the element:

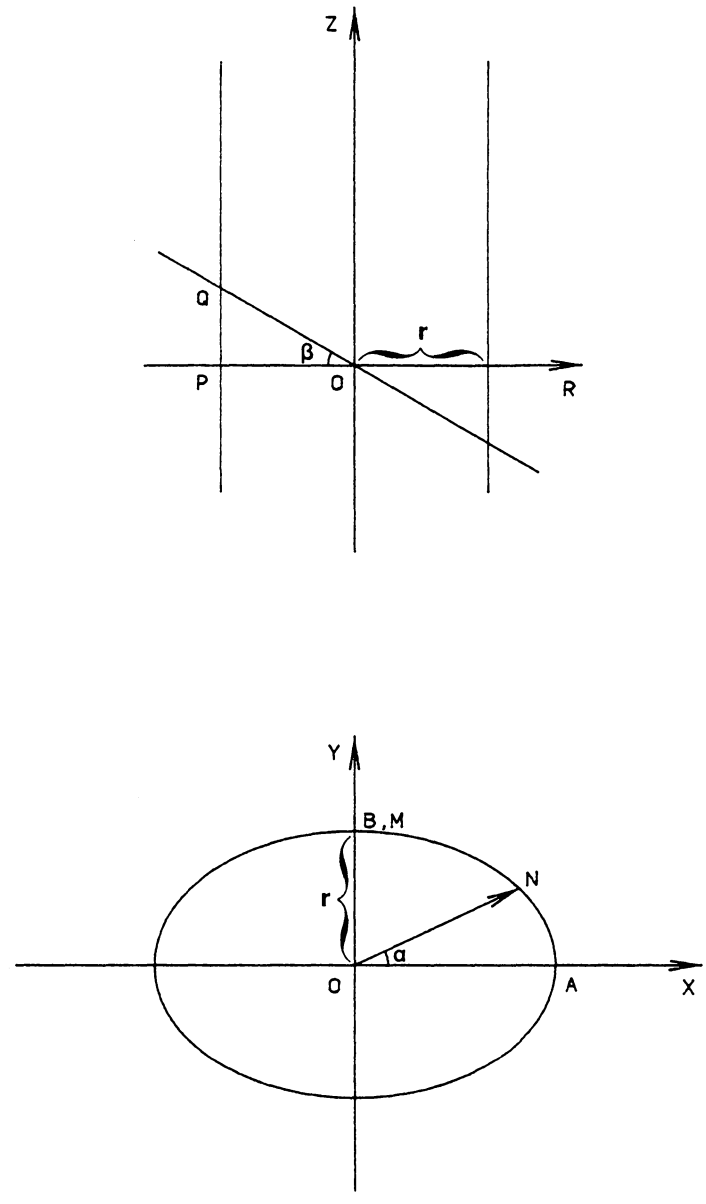

Figure 56. Special Case: θ = 90 deg

$$\kappa = \frac{b}{a^2} = \left\{ \cos^2\beta \right\} \frac{1}{r} \qquad (a.3.7)$$

Notice that the quantity $1/r$ in the above equation is just the curvature of the cylinder, or the smallest possible curvature of a fiber path on the cylinder. Thus, the curvature at any other direction can be obtained by multiplying the minimum curvature with the square of the cosine of the angle between that direction and the direction of minimum curvature. In other words, equation (a.3.7) is also the transformation of a curvature through an angle β from the direction of minimum curvature.

Other than these extreme cases, there are three types of curves: an ellipse when $\beta < \theta$, a parabola when $\beta = \theta$, and a hyperbola when $\beta > \theta$ The computations of the fiber path curvatures for these three cases are described below.

The case of $\beta < \theta$ is shown in Fig. 57. The intersection curve is an ellipse in the xy coordinate system with the origin located at point C. The major axis of the ellipse, a, is half the distance QS:

$$a = \frac{QS}{2} = \frac{OQ + OS}{2} = a'r \qquad (a.3.8)$$

where

$$a' = \frac{\sin\theta}{2}\left[\frac{1}{\sin\theta'} + \frac{1}{\sin\theta}\right] \qquad (a.3.9)$$

The offset distance from the origin O of the cylindrical coordinate system to the origin C of the Cartesian coordinate system is denoted by the quantity h:

$$h = a - OQ = h'r \qquad (a.3.10)$$

where

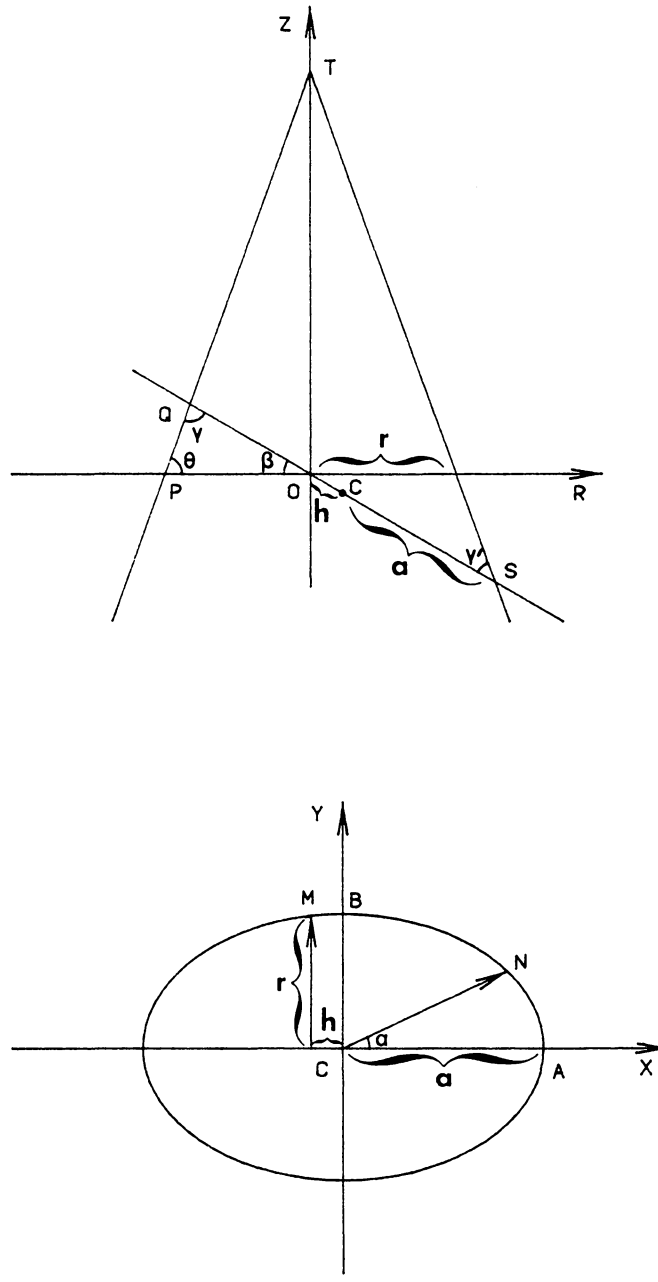

Figure 57. Case 1: Ellipse ($\beta < \theta$)

$$h' = \frac{\sin\theta}{2}\left[\frac{1}{\sin\gamma'} - \frac{1}{\sin\gamma}\right] \qquad (a.3.11)$$

The equation of the ellipse is written in the xy coordinate system as:

$$\frac{x^2}{a^2} + \frac{y^2}{b^2} = 1 \qquad (a.3.12)$$

where a is the major axis of the ellipse and b is the minor axis of the ellipse. The major axis was already computed above. The minor axis can be computed by evaluating the above equation at the point $(-h,r)$ and solving for b:

$$b = b'r \qquad (a.3.13)$$

where

$$b' = a'\sqrt{\frac{1}{a'^2 - h'^2}} \qquad (a.3.14)$$

The quantities a', b', and h' are independent of the radial position of the element center r.

The curvature of the ellipse is identical to the case of the cylinder, which was given in equation (a.3.6), except for the difference in the expressions for the coefficients. The fiber path curvature at the center of the element is evaluated at point M, where $x = -h$ and $y = -r$:

$$\kappa = \left\{\frac{a'b'}{\left[\left(\frac{a'}{b'}\right)^2 + \left(\frac{b'h'}{a'}\right)^2\right]^{3/2}}\right\}\frac{1}{r} \qquad (a.3.15)$$

The case of $\beta = \theta$ is shown in Fig. 58. The intersection curve is a parabola in the xy coordinate system. The offset center h between the cylindrical coordinate system and the Cartesian coordinate system is computed from the law of sines:

$$h = OQ = r\frac{\sin\beta}{\sin\gamma} = \frac{r}{2\cos\beta} \qquad (a.3.16)$$

Equation for the parabola in the xy coordinate system is:

$$y = -ax^2 \qquad (a.3.17)$$

The coefficient a is computed by evaluating the above equation at point $(r, -h)$:

$$a = \frac{1}{2r\cos\beta} \qquad (a.3.18)$$

Since the parabola is a single-valued function, the x coordinate can be used as the parameter. Consequently, the curvature of the parabola is given as:

$$\kappa = \frac{2a}{\left[1 + (2ar)^2\right]^{3/2}} \qquad (a.3.19)$$

The fiber path curvature at the element center is evaluated at $x = r$:

$$\kappa = \left\{\frac{\cos^2\beta}{(\cos^2\beta + 1)^{3/2}}\right\}\frac{1}{r} \qquad (a.3.20)$$

The case of $\beta > \theta$ is shown in Fig. 59. The intersection curve is a hyperbola in the xy coordinate system. The offset distance from the origin O of the cylindrical coordinate system to the origin C of the Cartesian coordinate system is given as the

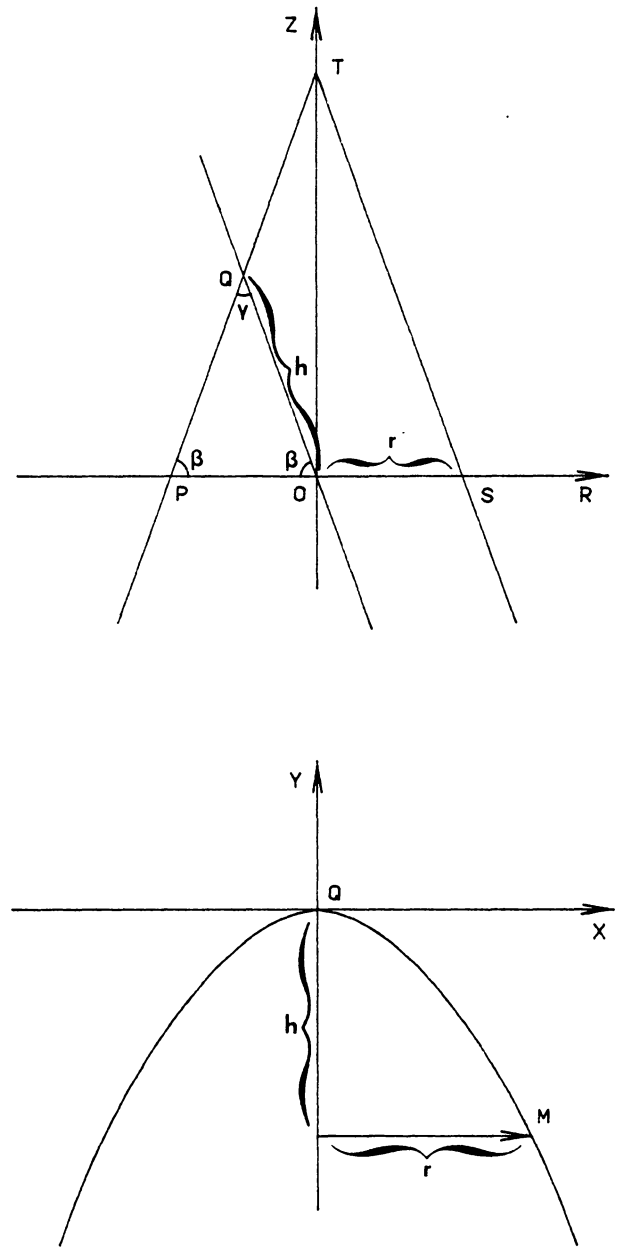

Figure 58. Case 2: Parabola ($\beta = \theta$)

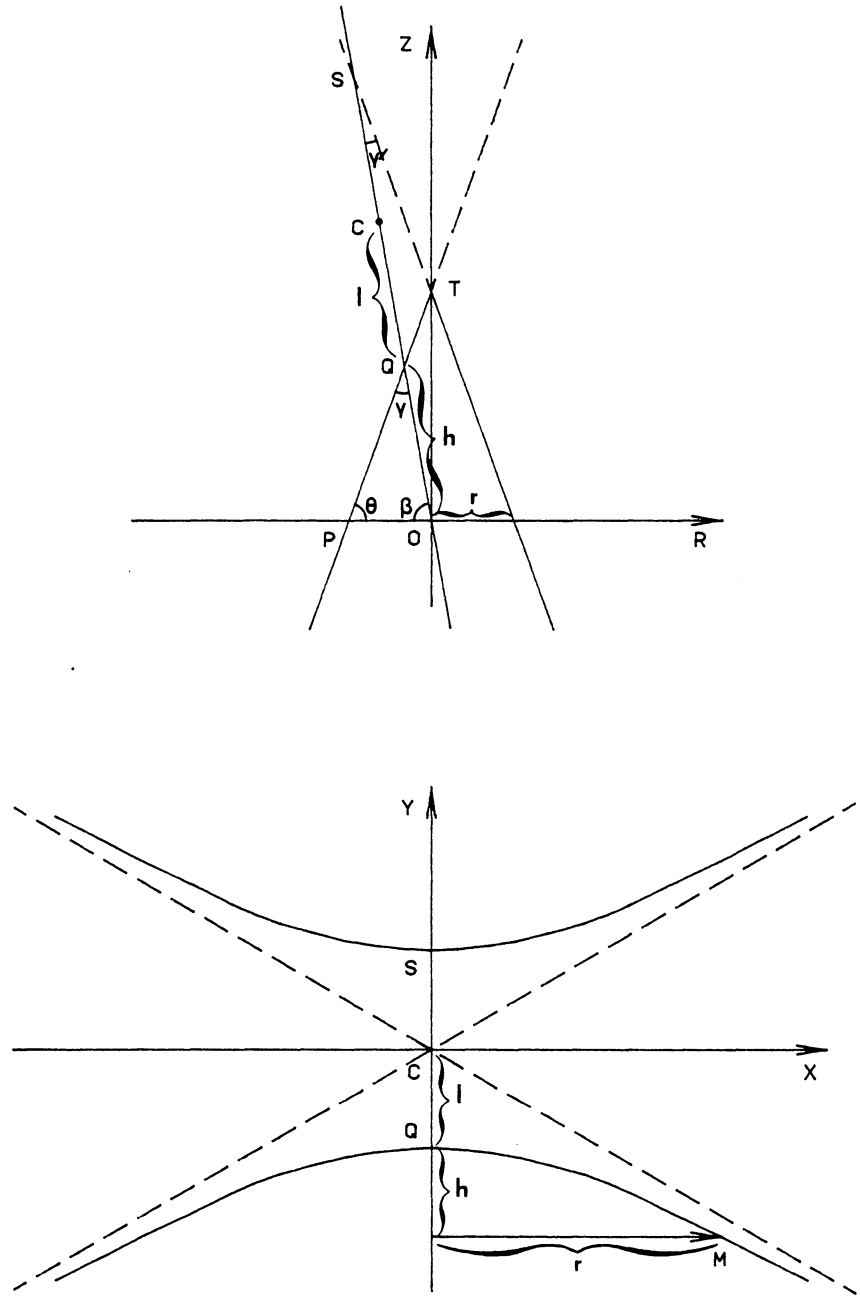

Figure 59. Case 3: Hyperbola ($\beta > \theta$)

quantity $l + h$, where l is the distance from C to the lower branch of the hyperbola and h is the distance from the lower branch of the hyperbola to O :

$$l = l'r \tag{a.3.21}$$

where

$$l' = \frac{r \sin\theta}{2}\left(\frac{1}{\sin\gamma'} - \frac{1}{\sin\gamma}\right) \tag{a.3.22}$$

and

$$h = h'r \tag{a.3.23}$$

where

$$h' = \frac{\sin\theta}{\sin\gamma} \tag{a.3.24}$$

Equation for the hyperbola in the xy coordinate system is:

$$\frac{y^2}{a^2} - \frac{x^2}{b^2} = 1 \tag{a.3.25}$$

The coefficients a and b are computed by evaluating the above equation at points $(0,l)$ and $(r,h + a)$:

$$a = a'r \tag{a.3.26}$$

where

$$a' = \frac{\sin\theta}{2}\left\{\frac{1}{\sin\gamma'} - \frac{1}{\sin\gamma}\right\} \tag{a.3.27}$$

and

$$b = b'r \tag{a.3.28}$$

where

$$b' = a' \sqrt{\frac{1}{(h' + a')^2 - a'^2}} \tag{a.3.29}$$

Again, the coefficients a', b', l', and h' are independent of the radial position of the element center.

By considering only the lower branch, one can let x be the parameter. The fiber path curvature at the element center is evaluated at $x = r$ and given as:

$$\kappa = \left\{ \frac{a'b'}{\left[1 + b'^2 - a'^2 + (h' + a')^2\right]^{3/2}} \right\} \frac{1}{r} \tag{a.3.30}$$

The curvatures calculated above are the minimum curvatures. Instead of these minimum curvatures, the fiber motion model requires the curvature of the fiber path in the normal direction. This in turn requires a transformation of the curvature from the direction of minimum value to the normal direction. This transformation was already described in the special case of the cylinder. Thus, if one can find the angle between the normal direction and the direction of minimum curvature then the transformation can be easily carried out. Figure 60 illustrates the calculation of this angle, shown as ω, for the case of $\beta < \theta$. This angle ω is the difference between angles μ and ν. Geometrical manipulations result in the following expression for ω:

$$\omega = \theta + \beta - 90° \tag{a.3.31}$$

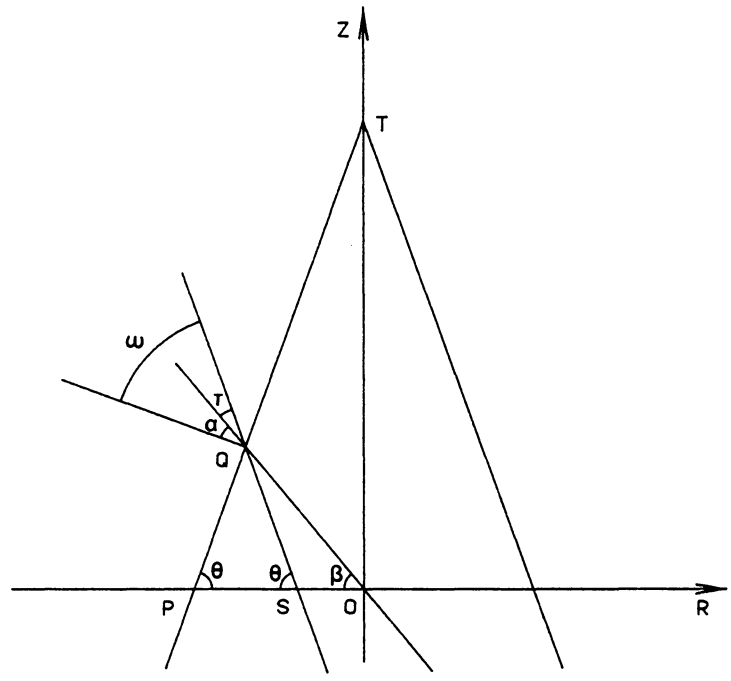

Figure 60. Calculation of Angle ω

The reader can verify that the above equation also holds true for other cases. Thus, the fiber path curvature in the normal direction, κ', is given in terms of the minimum curvature, κ, and angle ω:

$$\kappa' = \kappa \cos^2 \omega \qquad (a.3.32)$$

The vita has been removed from the scanned document